University of South Florida
Scholar Commons

Graduate Theses and Dissertations   Graduate School

1-1-2014

Development of Electroplated-Ni Structured Micromechanical Resonators for RF Application

Mian Wei
University of South Florida, mwei@mail.usf.edu

Development of Electroplated-Ni Structured Micromechanical

Resonators for RF Application

by

Mian Wei

A dissertation submitted in partial fulfillment
of the requirements for the degree of
Doctor of Philosophy in Electrical Engineering
Department of Electrical Engineering
College of Engineering
University of South Florida

Major Professor: Jing Wang, Ph.D.
Thomas Weller, Ph.D.
Sylvia Thomas, Ph.D.
Rasim Guldiken, Ph.D.
Andreas Muller, Ph.D.

Date of Approval:
September 3, 2014

Keywords: MEMS, Quality Factor, ALD,
Capacitive, Piezoelectric, Non-linearity

DEDICATION

To my mother Chunli Wang, my father Tiexiang Wei,

my husband Ivan Rivera and my son Alejandro Rivera

ACKNOWLEDGMENTS

First, I would like to thank the members of my dissertation committee: Prof. Jing Wang, Prof. Thomas Weller, Prof. Sylvia Thomas, Prof. Rasim Guldiken, and Prof. Andreas Muller, not only for their advice and suggestions, but also their time and patience to help me accomplish the doctoral program.

I would like to especially express my gratitude to my advisor Prof. Jing Wang, a passionate researcher and scientist who introduced me to the world of MEMS and guided my entire journey to achieve my Ph.D. Without his infinite ideas, encouragement, inspiration and support, I wouldn't have gone this far.

I would also like to thank all the staff from Nanotechnology Research and Education Center (NREC): Sclafani Louis-Jeune, Robert Tufts, Dr. Yusuf Emirov, Jay Bieber and Richard Everly, for running the laboratory smoothly and maintain the facility constantly to support students' projects. I especially appreciate the tremendous help and patience from Rich Everly, a cleanroom engineer who takes care of the equipment, trains the users and provides countless help on all the difficulties that the users have faced.

Other thanks go to the past and current group members (RF MEMS Transducers Group) for their friendship and encouragement. With all their efforts, our lab in IDRB is well organized and maintained so that I could fulfill my fabrication and measurement.

I am deeply indebted to my parents who raised me with all their best, always support me and help me pursue my dreams.

TABLE OF CONTENTS

LIST OF TABLES

LIST OF FIGURES

iv

ABSTRACT

On-chip vibrating MEMS resonators with high frequency-Q product on par with that of the off-chip quartz crystals have attracted lots of attention from both academia and industry for applications on sensing, signal processing, and wireless communication. Up to now, several approaches for monolithic integration of MEMS and transistors have been demonstrated. Vibrating micromechanical disk resonators which utilize electroplated nickel as the structural material along with either a solid-gap high-k dielectric capacitive transducer or a piezoelectric transducer have great potential to offer unprecedented performance and capability of seamless integration with integrated circuits.

Despite the frequency drift problems encountered in early attempts to use nickel as a structural material in MEMS gyroscopes, this low temperature nickel electroplating technology is amenable to post-transistor planar integration. The nickel microstructure is formed through the photoresist molding and electroplating process which enables the microstructure to have extremely high aspect ratio while retaining the overall process temperature under 60ºC. This temperature is low enough to allow the RF MEMS devices to be fabricated directly on top of foundry IC chips, thus enabling post-transistor monolithic integration with minimum parasitics. In addition, the electroplating setup for nickel deposition can be much cheaper as compared to the other deposition facilities (e.g., PVD, CVD, etc).

However, as the dimensions of the resonators are shrunk to μm range, several issues have come forth such as higher motional resistance and lower power handling ability. In order to reduce the motional resistance, high permittivity material is employed to form a solid capacitive

gap instead of an air gap. As compared to the air gap, ease of the process, better stability and elimination of the particles are the additional benefits of using the solid gap. Therefore, an ultra-thin high-k dielectric layer with atomically controlled thickness down to sub-nm range can be deposited under 100°C on the vertical sidewall of the device structure by using ALD processing technology. This enhances the efficiency of the capacitive transducer enormously, thus reducing the characteristic motional resistance of the device. This research project explored the idea of applying low temperature process of electroplated nickel and high-k solid-gap as well as partially-filled air-gap capacitive transducers. To further reduce the motional impedance, electromechanically-coupled resonator arrays have been implemented. Furthermore, the linearity of solid-gap versus partially-filled air-gap resonators has been studied through a modeling approach for RF applications.

In the meanwhile, this work also investigated electroplated nickel as a structural material for piezoelectrically-transduced resonators to demonstrate piezoelectric-on-nickel resonators with low temperature process. The thin film piezoelectric resonators can achieve high resonance frequency when increasing the piezoelectric film thickness and scaling down the device size. However, the sputtered piezoelectric films have very low deposition rate which limits the thickness to a couple of microns or less. Moreover, the yield of piezoelectric resonators is restricted after the releasing process since the stress of the thin films usually causes the structural layer to buckle or fracture. Thus, the development of piezoelectric-on-substrate resonators is an alternative solution to resolve the aforementioned issues. The previous work has been done by using single crystal silicon or nano-crystalline diamond (NCD) as resonator structural materials due to their high acoustic velocity and low loss. However, the deposition temperature for thin film silicon and diamond is too high to be allowable thermal budget of ICs. Therefore,

electroplated nickel is also a reasonable substitute for silicon and diamond substrates while realizing high frequency and moderate Q. Furthermore, it is observed that a localized annealing process through Joule heating can be adopted to significantly improve the effective mechanical quality factor for the ZnO-on-nickel resonators. This work successfully demonstrated the ZnO-on-nickel piezoelectrically-actuated MEMS resonators and resonator arrays with frequencies ranging from a few megahertz to 1.5 GHz by using IC compatible low temperature process.

CHAPTER 1 INTRODUCTION

Ever since David E. Hughes introduced the concept of wireless radio wave transmission in 1879 [1], wireless communication systems have become one of the most popular inventions in human history. This concept has completely changed the way people communicate and revolutionized every aspect of life. Presently, wireless electronic devices such as portable PC (personal computer), RFID (radio frequency identification tag), GPS (global positioning system), smartphones, and tablets with 3G, 4G or Wi-Fi have become part of our daily necessities. In addition, since the concept of "lab-on-a-chip" was introduced in 1959 [2], the newly developed micro-electro-mechanical system (MEMS) technology has pushed the studies of sensors and actuators forward on various novel applications such as micro harvesters for energy harvesting, accelerometers and gyroscopes in vehicles and game controllers, and BioMEMS in disease diagnostics, cell culture, drug delivery, vital sign sensors, medical implants, etc. Due to the fast growing evolution of these products which all demand for a wireless transceiver, wireless communication technology development in the past few decades has spurred the wireless gadgets with smaller size, lower cost and power consumption, simple interfaces, and better signal reception.

However, several challenges have to be addressed before this technology could move forward. On one hand, as we all know, antenna typically pick up the entire band of signals transmitted in the air. Hence, wireless receivers require components with superior frequency selectivity in order to receive the desired signals among other substantial frequency contents

while rejecting the adjacent strong interferences. On the other hand, in order to precisely generate and select those frequencies, off-chip components such as ceramic, surface acoustic wave (SAW) resonators and quartz crystals are widely utilized by RF filters and reference oscillators in present-day wireless transceivers. These off-chip components have abilities of achieving high quality factor (Q), however, in order to be functionalized, most of these high-Q components must interface with transistor circuits through board-level integration, which is not quite efficient from a cost perspective and it is also against the trends of miniaturization of wireless communication devices. Moreover, recent interests on integration of microelectronics and integrated circuits (ICs) have brought the focus on IC compatible technology development for the sake of reducing the cost and minimizing the size of integrated microsystem assemblies.

Among all the candidates, MEMS resonators hold great promises such as ability to operate at very high frequencies while achieving high quality factor (Q's > 10,000). Their micromechanical structures reduce the size by several orders of magnitude as compared to the traditional off-chip components. Moreover, it is demonstrated as an IC-compatible micro-fabrication technology [3] to eventually realize "system on a chip".

1.1 Background of Wireless Receiver Architecture

Wireless transceiver transmits and receives radio frequency signals by sharing the same electronic circuitry within a narrow channel bandwidth in a crowded communication environment. Thus, a transmitter is used to modulate the baseband data and then up-convert it to the carrier frequency for propagation as well as providing sufficient power amplification for the transmission in the medium. On the other hand, a receiver is to pick up and then demodulate the desired signals among the strong interferers and noise. Therefore, the receiver is much more challenging to implement as compared to the transmitter architecture. To better understand the

challenges on taking advantages of MEMS technology into wireless receivers, some traditional, novel, and MEMS-based wireless receiver architecture will be reviewed first.

1.1.1 Superheterodyne Receiver Architecture
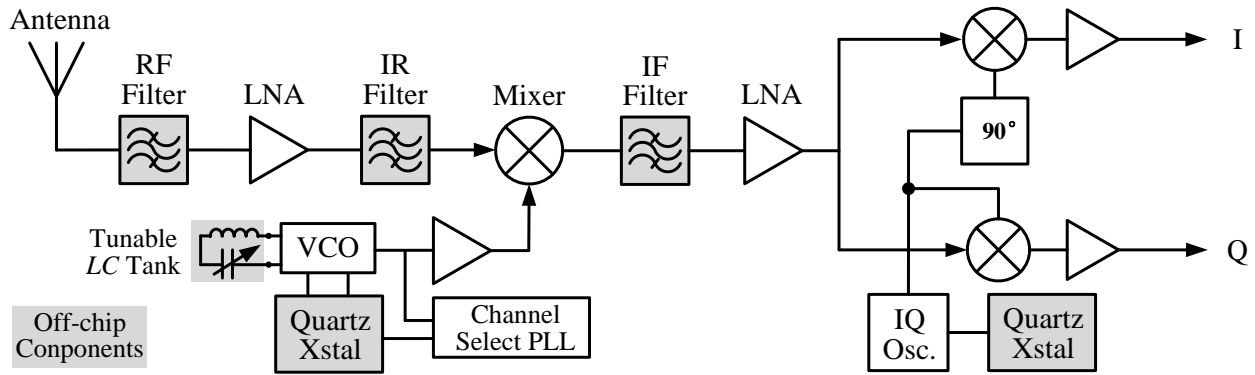
Figure 1.1 Schematic block diagram for a typical superheterodyne wireless receiver architecture [3].

The superheterodyne receiver, which was introduced by Edwin Armstrong in 1917 [4], is generally served as the receiver of choice in most transmitters and receivers due to its high selectivity and sensitivity. In order to achieve this selectivity, very high quality factor is required for a filter to reject out-of-band signals. On the other hand, the desired signals must be selected with minimum loss to meet the required sensitivity, resulting in difficulties for the filters in practical applications.

In a typical superheterodyne receiver, the signal band could be translated to a much lower frequency for the sake of relaxing the Q requirement of the channel select filters. As shown in Figure 1.1, after antenna receives a signal, it first passes through a band-select RF filter to remove out-of-band interferences. Followed by a low noise amplifier (LNA), the signal is amplified with minimum added noise. An image-reject (IR) filter is used to remove the image frequency, the selected signal is then down-converted to an intermediate frequency (IF) by multiplying the RF signal with a local oscillator (LO) signal using a mixer. The LO signal is

3

generated by a voltage controlled oscillator (VCO) together with a phase locked loop (PLL) configuration locked to a mechanical reference oscillator using off-chip components such as quartz crystals. Thereafter, the an IF filter picks up the selected channel in which the desired signal is then amplified and demodulated as baseband data. The role of the various filters in this superheterodyne receiver is illustrated to reduce the RF signal frequency and relax the Q requirement [5]. However, such architecture requires all kinds of high-Q off-chip components such as ceramic, quartz crystals and surface acoustic wave (SAW) resonators, which have to interface with transistor electronics at board level thus hindering both transceiver miniaturization and cost reduction.

1.1.2 Direct-Conversion Receiver Architecture
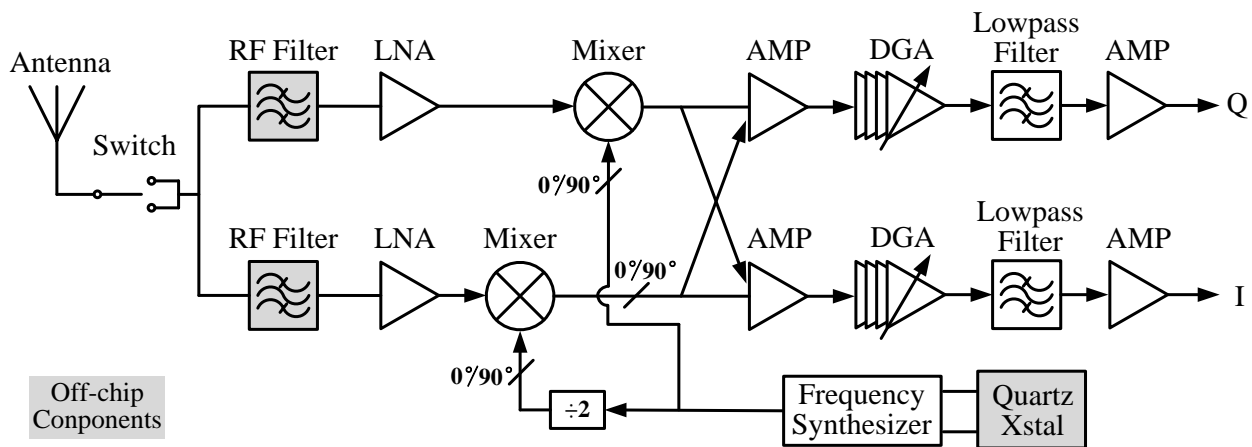
Figure 1.2 Schematic block diagram for a typical direct-conversion wireless receiver architecture [6].

Another popular architecture is direct-conversion receiver which has been widely used in mobile communication handsets due to its low cost, reduced size and low power consumption. Generally, the direct-conversion receiver is just like superheterodyne receiver converting the received RF signal directly down to the baseband, but with reduced numbers of off-chip components as shown in Figure 1.2. By setting the local oscillator frequency equal to the RF

signal frequency, there is no image frequency signal generated as compared to the superheterodyne. Therefore, the image reject filter is unnecessary in this direct-conversion receiver architecture, which is also known as "zero-IF" or "homodyne" receiver. Moreover, zero-IF also brings the advantage of further reducing the cost and size by replacing the channel select filter (IF filter) applied in the superheterodyne receiver by a low-pass filter (LPF) which can be implemented by transistor circuitry [6].

1.1.3 MEMS-Based Novel Receiver Architecture
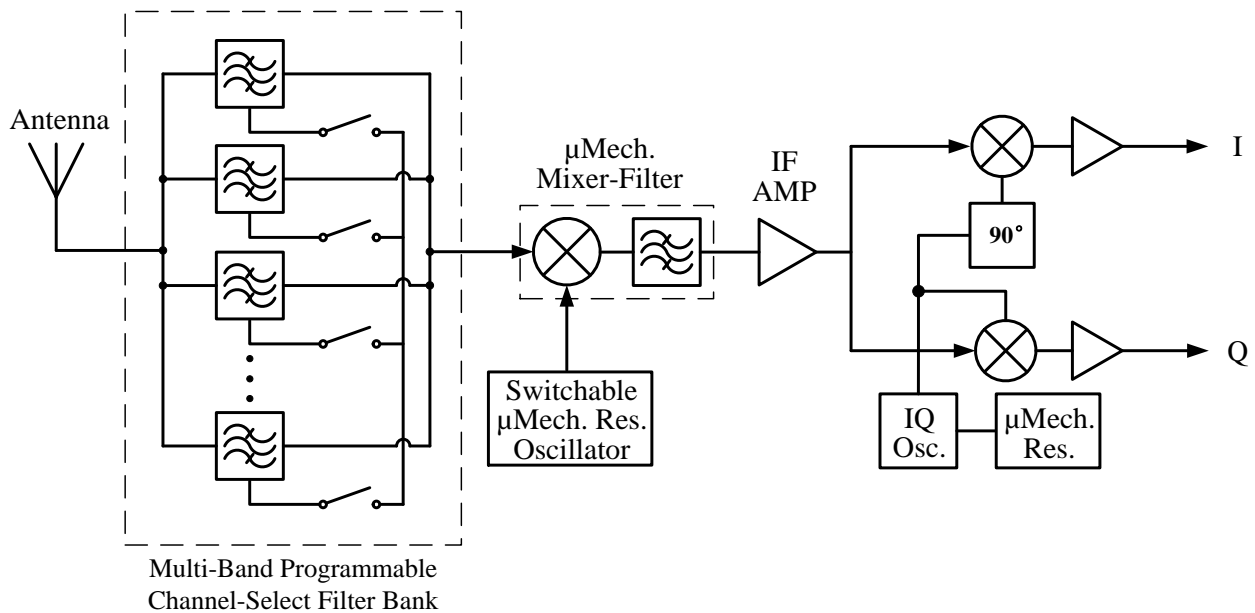
Figure 1.3 Schematic block diagram for a micromechanical resonator enabled channel-select receiver architecture [3].

Basically, both superheterodyne receiver and direct-conversion receiver architectures could be implemented into a single chip by substituting the off-chip high-Q passive devices (e.g. SAW filters and crystal reference oscillators, etc.) with MEMS-based elements. The advantages of applying on-chip MEMS components not only include the size shrinkage, cost reduction and power saving, but also the performance improvement such as high frequency, high-Q, high

dynamic range, and sharp cut-off. With the help of IC-compatible MEMS technology, the system-on-a-chip could be potentially realized with unprecedented levels of functionality, reliability, and sophistication.

By applying multi-band programmable channel-select filters, mixer-filter and switchable oscillator, Figure 1.3 presents a system-level block diagram which consists of several on-chip MEMS resonators. Compared to superheterodyne receiver as shown in Figure 1.1, MEMS-based novel receiver takes the advantage of MEMS technology to realize a front-end RF channelizer [3], an IF mixer-filter (also known as "mixler") [7] and less loss micromechanical circuits in order to lower the power consumption and prevent from using RF low noise amplifier (LNA) and transistor mixer.

1.2 Fundamentals of Quality Factor (*Q*)
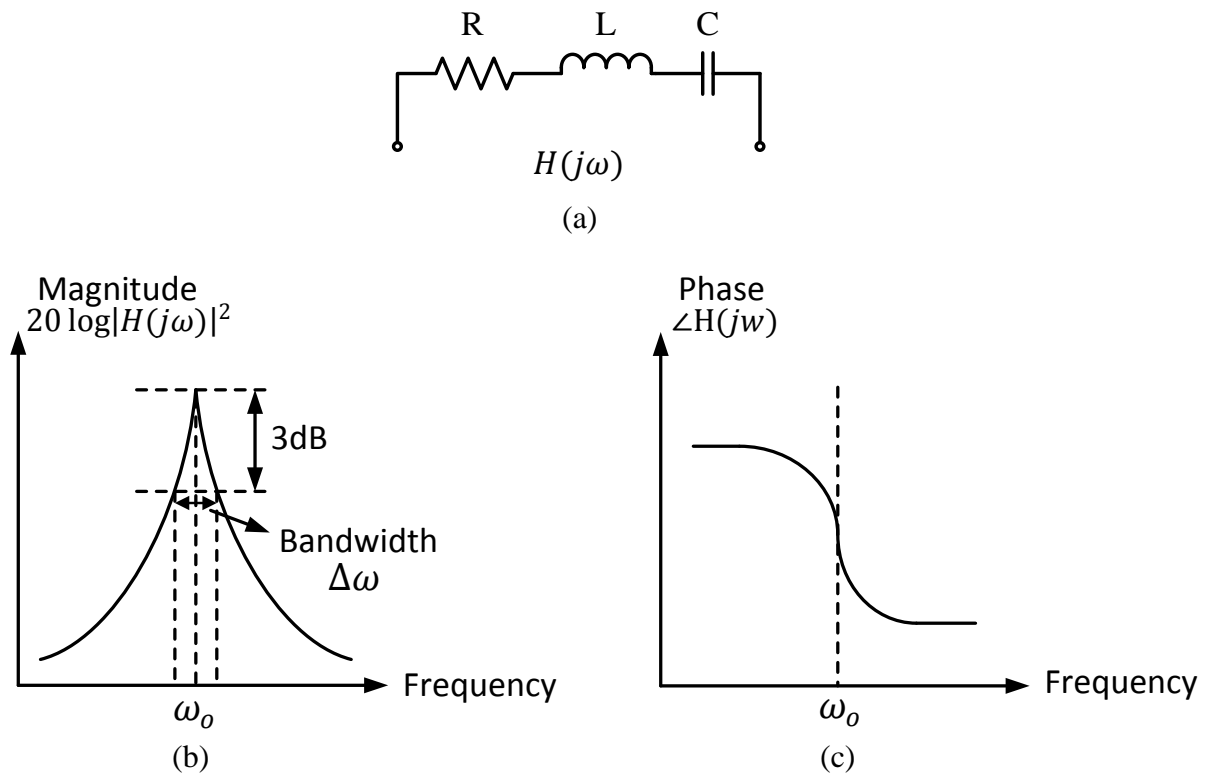
Figure 1.4 (a) A series RLC circuit representing the transfer function of a resonator; with (b) its magnitude and (c) phase spectra in frequency domain.

6

The key parameter that is used to evaluate the performance of a resonator, filter and reference oscillator is the quality factor which could affect the selectivity, noise figure, insertion loss, etc. Therefore, higher Q has always been pursued when designing these devices. There are three common approaches to define this important parameter.

1.2.1 Q by Energy

In a resonator, the quality factor is defined as the ratio between the energy stored in the resonator and the energy dissipated per cycle as

$$Q = 2\pi \times \frac{\text{Energy Stored}}{\text{Energy Dissipated per Cycle}} \tag{1.1}$$

In a *RLC* circuit illustrated in Figure 1.4 (a), the inductor, capacitor and resistor are connected in series, and the quality factor is defined as

$$Q = \frac{\omega_o L}{R} = \frac{1}{\omega_o RC} \tag{1.2}$$

where R is the resistance, L is the inductance, C is the capacitance and ω_o is the resonant frequency of the LC tank, which can also be defined as

$$\omega_o = \frac{1}{\sqrt{LC}} \tag{1.3}$$

Taking the MEMS resonator as an example, the quality factor indicates the ability to retain the mechanical energy in the system. In order to obtain higher Q, the energy loss should be minimized which is contributed by squeeze film damping, anchor loss, thermoelastic damping, and so on [8].

1.2.2 Q by Bandwidth

In the complex frequency domain, a mechanical resonator can be modeled as a RLC circuit, the transfer function of which indicates the relationship between the input and output of the resonator. Thus, the transfer function can be expressed with its magnitude and phase as

$$H(jw) = H(s)|_{s=jw} = |H(jw)| \cdot e^{j\angle H(jw)} \tag{1.4}$$

where $|H(jw)|$ and $\angle H(jw)$ are the magnitude and phase function of $H(jw)$, both are illustrated in Figure 1.4. For the magnitude function, Q of the RLC circuit can be defined as

$$Q = \frac{\omega_o}{\Delta\omega} \tag{1.5}$$

where ω_o is the center frequency and $\Delta\omega$ is the bandwidth between two cut-off angular frequencies at -3dB from ω_o as shown in Figure 1.4(b). To obtain a higher Q, a sharper frequency response is preferred to provide a narrow passband, which specifies the selectivity of the resonant tank.

1.2.3 Q by Phase

According to the transfer function (1.4) and phase response illustrated in Figure 1.4 (c), Q can also be defined as a function of its phase in complex frequency domain by

$$Q = \frac{\omega_o}{2} \cdot \left|\frac{d\phi}{d\omega}\right| \tag{1.6}$$

where ϕ is the phase response, which indicates a phase change at the resonance frequency.

1.3 MEMS-IC Integration Technology

As the development of MEMS technology becomes increasingly popular and significant, the integration of MEMS devices with integrated circuits (IC) has attracted a great deal of attention from both academia and industry, which holds great promise to potentially revolutionize the entire regime of the wireless technology for its compactness and performance. The traditional approach of MEMS-IC integration utilizes the hybrid integration technologies such as 3D through silicon via (TSV) stacking, chip-to-wafer bonding (C2W), wafer-to-wafer bonding (W2W) and so on [9]. By allowing the MEMS devices and the integrated circuits to be

8

designed and optimized independently, this modular hybrid approach has been widely employed on various products [10, 11]. However, the cost of assembly and packaging is far from optimum.

<div style="text-align:center">(a)   (b)</div>

Figure 1.5 MEMS-IC integration by (a) hybrid approach and (b) monolithic approach [12].

The monolithic approach, as a comparison, has advantages of lower cost, miniaturization ability, parasitic reduction and signal transduction enhancement due to its higher level of integration. Based on different fabrication sequences, MEMS-IC monolithic integration can be realized through four main approaches: (1) MEMS-first technology; (2) MEMS-last technology; (3) merged IC-MEMS technology; and (4) MEMS embedded within IC technology [9]. In order to address the key challenge on direct integration of RF MEMS passives with foundry-IC chips to strengthen the signal processing ability, MEMS-last technology provides several advantages such as reducing interconnect parasitic resistance and capacitance by fabricating MEMS devices directly over an integrated circuit chip.

Due to the concerns related to the limited thermal budget for IC electronics, low temperature post-IC fabrication process is highly preferred for MEMS-last strategy. As a sequence, MEMS structural materials and fabrication processes have been limited by the temperature restriction (below 425°C) and application requirement (e.g. conductivity, damping loss, strain, stress, thermoelastic damping, biocompatible and so on). As for micromechanical resonators, electroplated nickel is a good candidate among all the available structural materials since nickel has a relatively high acoustic velocity and low deposition temperature (40°C ~ 60°C)

which has been explored to demonstrate gyroscopes and resonators with high quality factors [13, 14].

1.4 Mixers and Filters
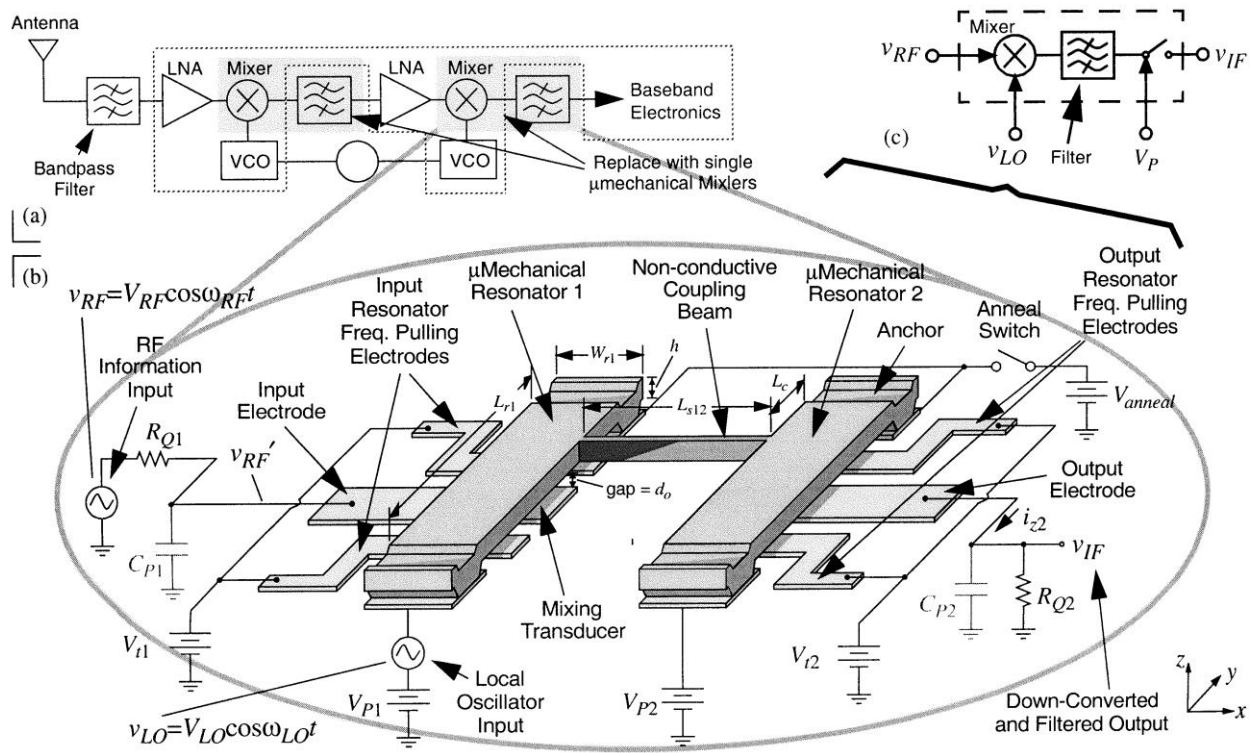
Figure 1.6 (a) Simplified block diagram of a wireless receiver indicating the replaceable components by mixler configuration; (b) Schematic diagram of micromechanical mixler for frequency down-conversion; (c) Equivalent block diagram of the mixler scheme [7].

As mentioned in section 1.1, the received signal from antenna must be processed at the lower baseband frequency in a superheterodyne receiver. As a result, filters and mixers are highly demanded for frequency filtering, selection and conversion in order to minimize the power consumption. Frequency conversion is a process that involves the multiplication of two signals using a nonlinear device of which the output is no longer a simple proportional to the input. Both up-conversion and down-conversion could be achieved by a mixer product depending on the transceiver architecture, while down-conversion is mostly used in wireless

receivers. A frequency selective filter usually follows after the mixer, removing all the by products from the mixer while selecting the desired frequency channel.

In order to maximize performance, frequency selection and conversion are normally achieved by using separate and distinct components that must be interfaced with each other at the board level. On one hand, these off-chip components increase the design complexity and power consumption by matching the output of the mixer to the subsequent filter; on the other hand, this architecture circumvents the size reduction in the portable communication devices and induces additional insertion loss because of the impedance mismatches between the mixer output and the filter input. Thus, by interlinking micromechanical resonators with nonlinear capacitive transducers, "mixler" device has been studied and demonstrated to fulfill frequency down-conversion and intermediate frequency filtering, thereby replacing mixer and filter devices in wireless transceivers [7].

1.5 Previous Work of Micromechanical Resonators

On-chip vibrating MEMS resonators with high frequency-Q products have attracted great attention from both academia and industry because of their versatile applications in the promising fields of sensing, signal processing, and wireless communication systems. Among the wide variety of MEMS transduction mechanisms, piezoelectrically-actuated resonators equipped with well documented piezoelectric materials such as zinc oxide, aluminum nitride, barium titanate and lead-zirconate-titanate (PZT) have been widely studied. Also, acoustic-wave-type piezoelectric transducers such as surface acoustic wave devices (SAW), bulk acoustic wave device (BAW), and film bulk acoustic resonator (FBAR), have been broadly accepted by the industry into products such as filters and duplexers. However, due to the relative low-Q, these

piezoelectrically-transduced resonators have limited abilities in signal processing such as narrow-band filtering.

Thus, the advent of capacitively-transduced resonators with measured resonance frequency easily exceeding 1GHz along with ultra-high Q (>10,000) have spurred new vigor in wireless communications. Aside from their high frequency-Q products, a widely adjustable range of linearity, low power consumption and high power handling are the other benefits of capacitive transduction.

1.5.1 Piezoelectrically-actuated Resonators
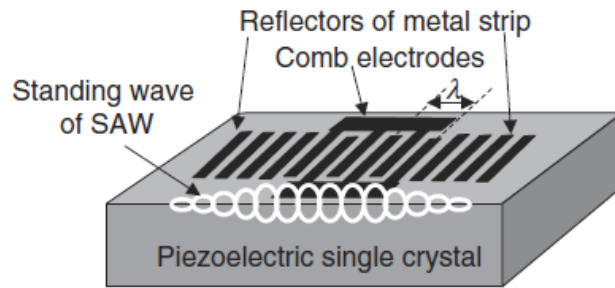
Figure 1.7 Schematic of a typical SAW resonator [15].

Piezoelectric materials, such as quartz, zinc oxide, aluminum nitride, barium titanate and lead-zirconate-titanate (PZT), have been widely employed in a variety of electromechanical devices ever since they were discovered in 1880. In response to an applied electric field, piezoelectric material deforms and induces a mechanical strain which generates charges within the material. Piezoelectric resonator normally consists of a piezoelectric material and a mechanical structure along with strategically placed electrodes, which are employed to facilitate the coupling between the mechanical strain and the induced electrical field. When the applied AC signal matches the resonance frequency of a piezoelectric resonator, the acoustic wave will be excited and converted back to the electrical signal through the output piezoelectric transducer.
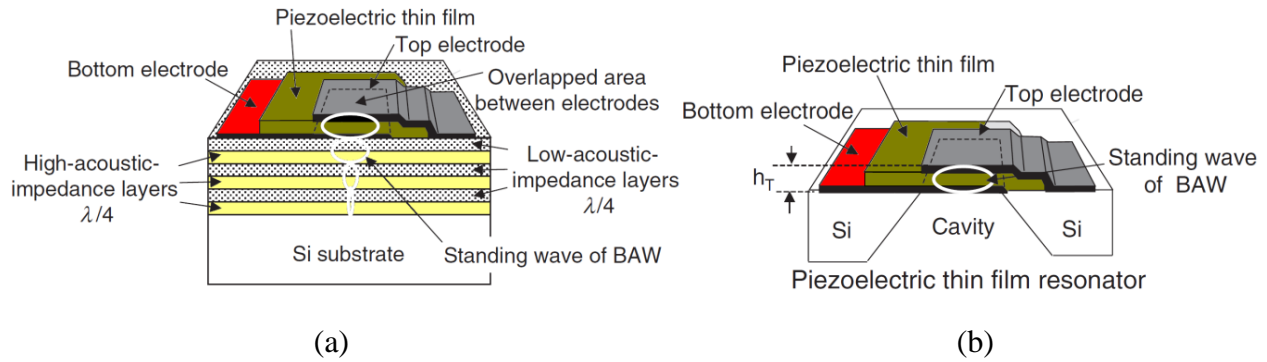
Figure 1.8 Schematic view of BAW resonators in (a) SMR and (b)FBAR configurations [15].

Surface acoustic wave (SAW) is a mechanical wave which has both vertical shear and longitudinal component and is capable of propagating along the surface of piezoelectric material as shown in Figure 1.7. SAW resonators usually use inter-digital transducers (IDTs) to convert energy between electrical and mechanical domains, which have been widely applied in filters and sensors [16].
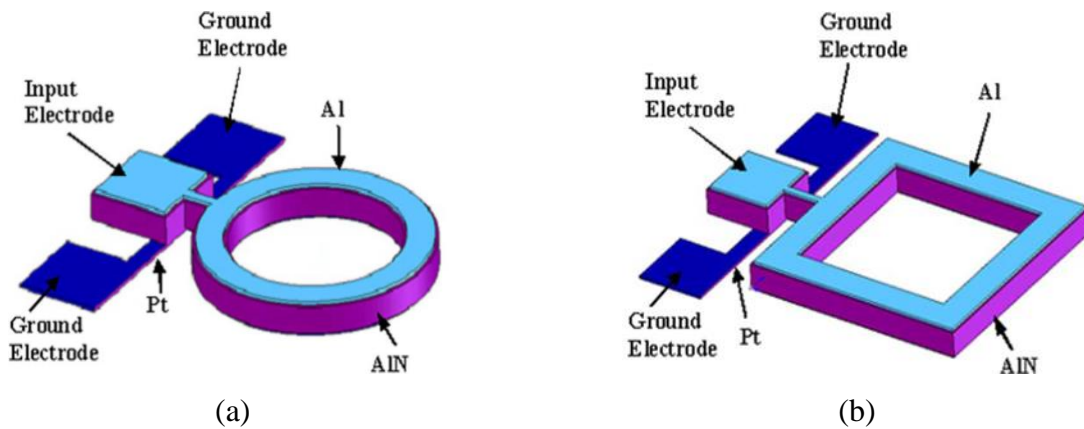
Figure 1.9 Contour-mode ring resonators: (a) One-port circular ring resonator; (b) One-port square-shape ring resonator [17].

Unlike the surface acoustic wave, bulk acoustic wave (BAW) travels from one surface through the piezoelectric material to the other surface, forming a sandwiched resonator structure which consists of top electrode, piezoelectric thin film and bottom electrode. There are two kinds

of implementation of BAW resonators as shown in Figure 1.8. One is the solid mounted resonator (SMR) which adopts Bragg reflectors to achieve mismatched acoustic impedance, and the other one is the film bulk acoustic resonator (FBAR) which simply applies air cavity to generate the high impedance mismatch for the sake of retaining acoustic energy in the resonator body [15].

Since the frequency of FBAR devices is determined by piezoelectric film thickness, only one frequency can be designed on a single chip without post-process thickness trimming. Therefore, a newly developed contour-mode resonators were designed to be able to achieve various selected frequencies on a single chip as their resonance frequencies are determined by the lateral dimensions. As shown in Figure 1.9, both circular and square shaped ring resonators can be designed with variety radius and width, and built as a sandwich structure including Pt bottom electrode, AlN elastic body and Al top electrode [17].

(a)   (b)
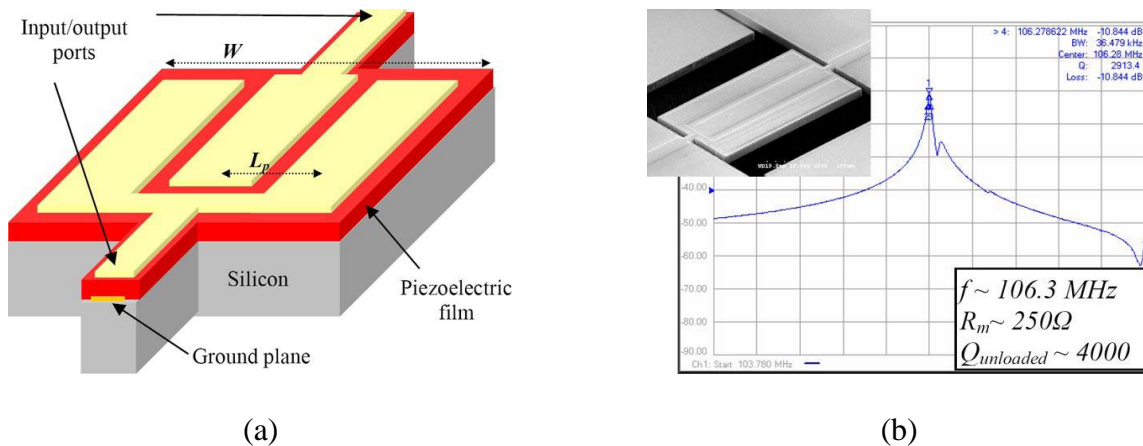
Figure 1.10 (a) Schematic view of a two-port third-order thin-film piezoelectric-on-substrate resonator; (b) frequency response and SEM of a third-order AlN-on-silicon resonator [18].

Another lateral extensional resonator, thin-film piezoelectric-on-substrate resonator (TPoS), has recently been developed [18]. TPoS resonators employ the sandwich structure of bottom electrode, thin-film piezoelectric layer and top electrode on top of a thick, low-acoustic-

loss and resonant structure made of single crystal silicon or nano-crystalline diamond as shown in Figure 1.10 (a). By taking the advantage of piezoelectric transduction and a low loss mechanical structure, this kind of devices provides very low motional impedance at relatively high frequencies with moderate to fairly high quality factor.

1.5.2 Capacitively-transduced MEMS Resonators

(a)   (b)   (c)
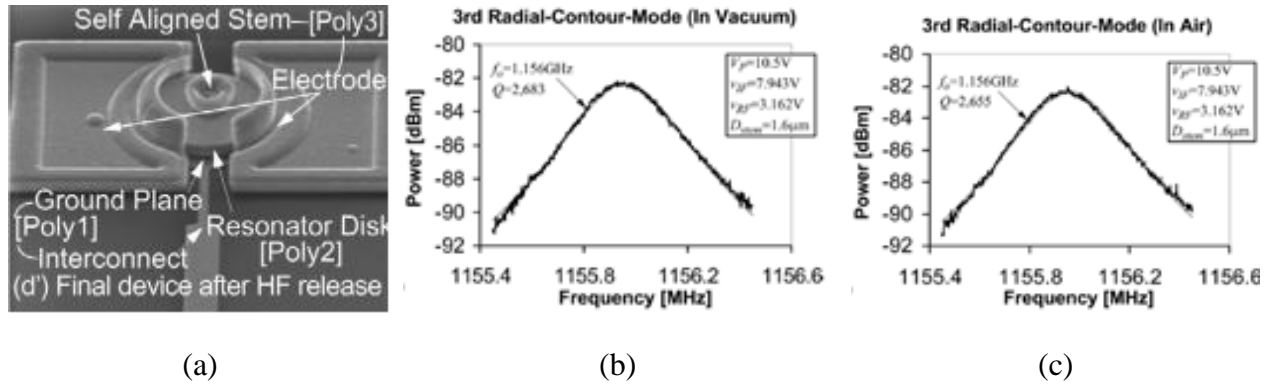
Figure 1.11 (a) SEM photo and measured frequency response in (b) vacuum and (c) air for a polysilicon capacitively-transduced radial-contour mode disk resonator [19].

In contrast to the piezoelectric resonators, capacitive resonators are capable of achieving higher frequency-Q performance. As a result of employing high quality structural materials (e.g. high acoustic velocity, low loss) such as polycrystalline silicon, silicon carbide, polycrystalline diamond and ultrananocrystalline diamond (UNCD), capacitively-transduced resonators with ultra-high quality factor (~100,000) have been demonstrated at ultra-high frequency along with good thermal stability [20], high frequency stability [21], voltage-controlled tunability [22], IC-compatibility and self-switching capability [23].

For the sake of obtaining high-Q in ultra-high frequency surpassing 1 GHz, a mass-production viable fabrication methodology has been studied and demonstrated in a series of polysilicon radial-contour mode disk resonators: Q's of 7,330 in vacuum and 6,100 in air at frequency of 733 MHz [24]; Q's over 1,500 in both vacuum and air at frequency of 1.14 GHz

[24]; and Q's over 2,650 in both vacuum and air at frequency of 1.156 GHz [19]. In contrast to the traditional anchor-alignment-refill technology which imposes a limitation of lithography alignment tolerance, this new self-alignment technique allows the supporting stem to be placed at the exact center of the disk resonator body which is also known as the motionless nodal point, as shown in Figure 1.11 (a). In consequence, this type of device symmetrically balances the resonator during radial vibration and dramatically reduces the energy loss from the anchor, resulting in high Q in both air and vacuum at gigahertz frequency.

| (a) | (b) | (c) |
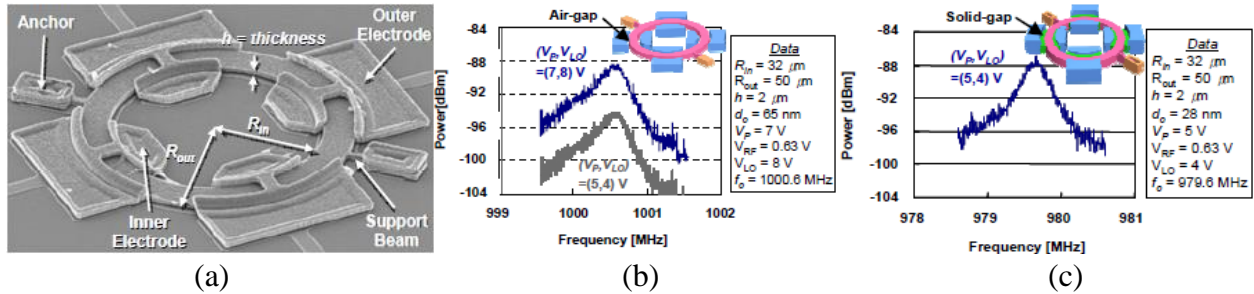
Figure 1.12 (a) SEM photo and measured frequency response with (b) air-gap and (c) solid-gap of a fabricated extensional wine-glass ring resonator [25].

Although offering a high Q in GHz-range frequency, capacitively-driven micromechanical resonators still suffer from their relatively high impedance which prevents this type of devices from directly matching the 50 Ω systems for RF applications. In order to lower the impedance, solid-filled dielectric transducer gaps have been demonstrated in polysilicon micromechanical compound-(2,4) mode ring resonators, achieving 979.6 MHz with Q's of 3,100 while reducing motional resistances 4.7 times as compared to that of air-gap devices [25]. Since the motional resistance is proportional to the fourth power of resonator-to-electrode gap, reducing the gap spacing is a highly effective approach to lower the impedance aside from its limitation by the fabrication technology and reduction of the pull-in voltage. Applying a dielectric material of 28nm-thick nitride layer, whose permittivity is much higher than that of air,

a much smaller gap can be defined compared to the 65nm air-gap, which also reduces the motional resistance.
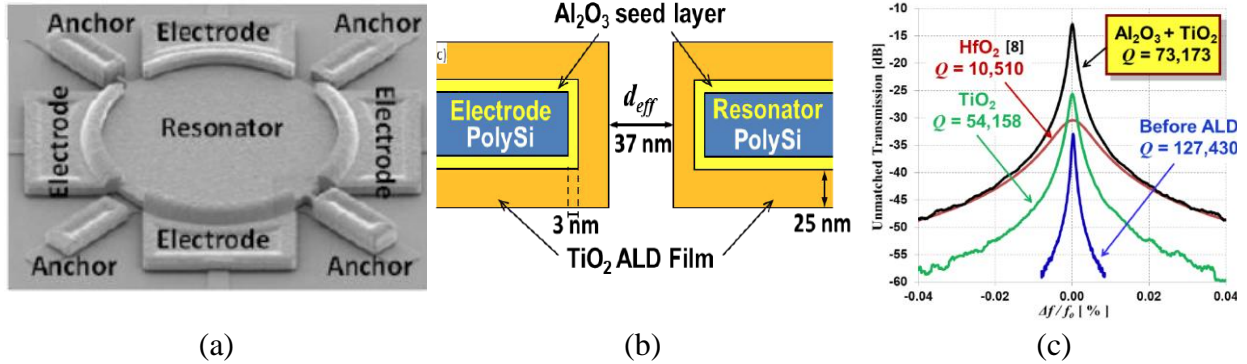
Figure 1.13 (a) SEM picture of polysilicon wine-glass mode disk resonator; (b) Schematic view of resonator-to-electrode gap reduction from 87nm to 37nm via ALD partial-gap refill; (c) Comparison of measured frequency characteristics under vacuum with dc-bias voltage of 9V for 61-MHz wine-glass disk resonators treated with various ALD partial gap filling recipes [26].

To further reduce the motional resistance for capacitively-transduced micromechanical resonators, partially filling the electrode-to-resonator gap by atomic layer deposition has been studied [26, 27]. The traditional approach, which adopts a wet etchant to release the resonator structure so that the device could move, anticipates difficulties of shrinking the gap spacing under 60nm. Thereby, an alternative approach, which generate a roughly 100nm air gap followed by atomic layer deposition to partially fill the capacitive gap with non-conductive high-k dielectric material, successfully reduces the electrode-to-resonator gap to 37nm, as shown in Figure 1.13 (b). As a result of the relatively high permittivity of ALD dielectric materials, the effective capacitance of this partially-filled capacitive transducer is still dominated by the air gap. With the new technique, capacitively-transduced micromechanical disk resonator has achieved low motional resistance ($< 130\Omega$) and high Q ($> 70,000$) simultaneously at 61MHz.

As the new generation of IC process can only survive temperature below 425°C, post-transistor MEMS integration with foundry IC has been demonstrated with a new structural

material of nickel which can be deposited at very low temperature while remaining high Q [13]. With a highest process temperature of 380°C, electroplated-nickel micromechanical disk resonator has achieved Q's over 54,000 at frequency of 60 MHz as seen in Figure 1.14, which proves its ability of post-fabrication over finished foundry transistors. Moreover, in order to improve the quality factor of metal structural devices, anchorless design and in situ localized annealing have been effectively studied to reduce the anchor loss and improve drift stability, respectively.

(a)   (b)
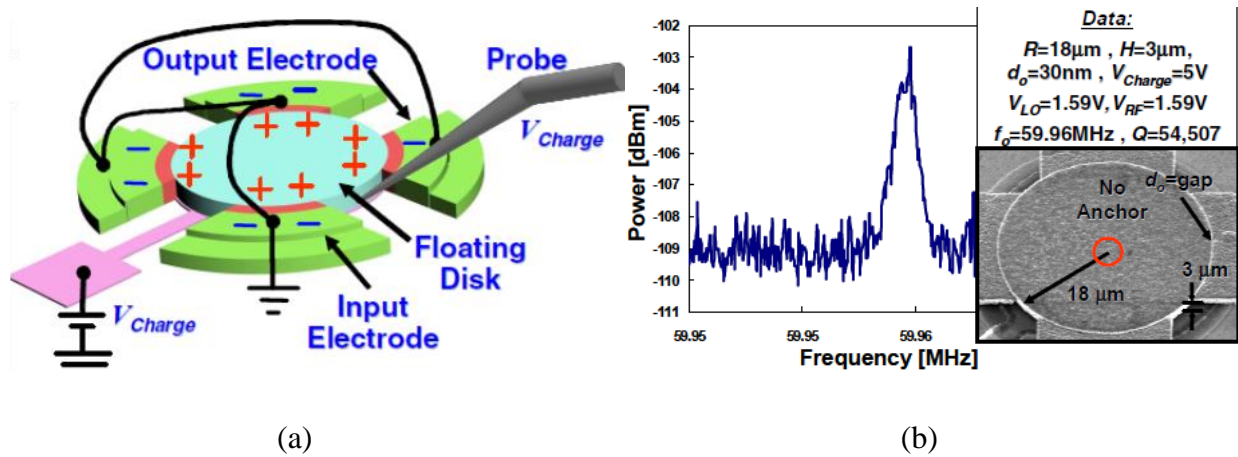
Figure 1.14 (a) Schematic view of charge-biasing the disk via a charged probe tip; (b) Mixing measurement and SEM photo of a stemless charge-biased 60-MHz wine-glass mode nickel disk resonator [13].

In this work, capacitively-transduced electroplated-nickel micromechanical resonators and resonator arrays have been designed and fabricated with air gap, solid gap and partially-filled air gap in low-temperature IC compatible process. Moreover, the linearity of solid-gap versus partially-filled air-gap resonators has been studied through a modeling approach for RF applications. In the meanwhile, this work also investigated electroplated nickel as a structural material for piezoelectrically-transduced resonators and successfully demonstrated the ZnO-on-

nickel piezoelectrically-actuated MEMS resonators and resonator arrays with frequencies ranging from a few megahertz to 1.5 GHz by using IC compatible low temperature process.

CHAPTER 2 CAPACITIVELY-TRANSDUCED RESONATORS

At present, capacitively-transduced micromechanical resonators have achieved resonant frequency in the GHz range [19, 28] with Q values exceeding 10,000 [29, 30] which holds a great potential for the applications on on-chip filters and low noise oscillators in wireless communications. However, the trade-off for extending operation frequencies by scaling the dimensions of micromechanical resonators is the highly increased impedance reported from 1~2500 kΩ [19, 29], which is far too large to be matched with the 50-377 Ω range impedance that is widely expected for off-chip components in the RF front ends. Although capacitively-transduced resonators have offered the highest frequency-Q product among micromechanical resonators, their inherent high impedance still prevents this kind of devices from taking over the piezoelectrically-actuated resonators, which can achieve quite low impedance without the need of bias voltages. Thus, ongoing efforts have been put into studying on how to reduce the motional impedance of capacitively-transduced resonators for directly matching the output circuits [25, 26].

2.1 Capacitive Transducer

As shown in Figure 2.1 (b) and (c), a wine-glass mode disk resonator is comprised of four supporting beams located at its quasi-nodal points (also known as motionless points), one input (driving) electrode and one output (sensing) electrode. In order to excite the device, an alternating AC signal v_i is applied to the input electrode generating an electrostatic force to drive the resonator to its vibration frequency mode. At the same time, a DC-bias voltage V_p is applied

20

directly on the resonant structure forming a capacitance between the resonator disk and the output electrode which induces an output current i_o. This time-varying electrostatic excitation force can be expressed (in phasor form) as following if $V_p \gg v_i$,

$$F_{ele} \cong V_p \cdot V_i \cdot \frac{\partial C}{\partial x} \tag{2.1}$$

where $\partial C/\partial x$ is the integrated change in electrode-to-resonator overlap capacitance per unit displacement; V_i is the phasor form input voltage (i.e. the voltage amplitude here).

(a)

(b)

(c)
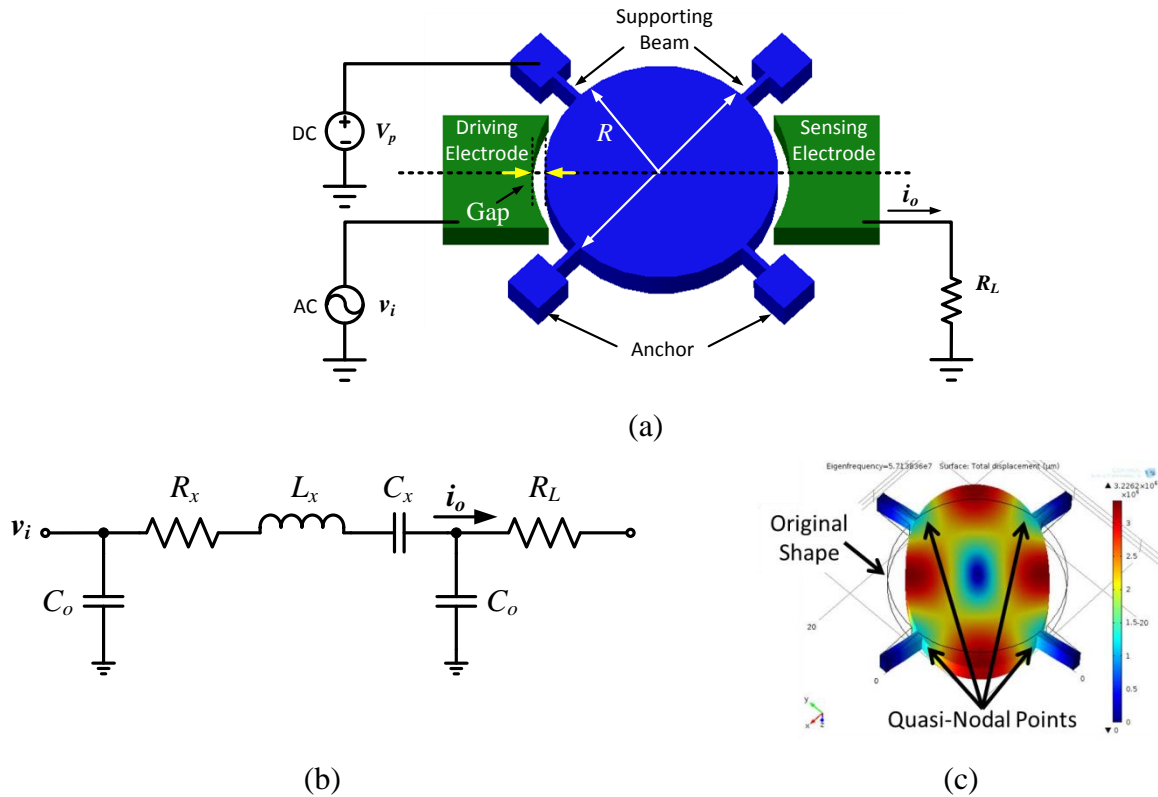
Figure 2.1 (a) Perspective schematic view of an air-gap wine-glass mode disk resonator in a two-port measurement set-up; (b) Equivalent circuit of a wine-glass mode disk resonator; (c) COMSOL simulation of wine-glass mode shape.

When the frequency of AC signal matches the resonance frequency of the disk resonator, the amplitude of the resonance vibration can be expressed by

$$X = \frac{Q F_{ele}}{j k_{re}} = \frac{Q}{j k_{re}} \cdot V_p \frac{\partial C}{\partial x} V_i \tag{2.2}$$

21

where Q is the quality factor of the resonator; k_{re} is the resonator equivalent stiffness. Along with the vibration, the time-varying capacitance between the disk and output electrode also produces an output current expressed by

$$i_o = V_p \cdot \frac{\partial C}{\partial t} = V_p \cdot \frac{\partial C}{\partial x} \cdot \frac{\partial x}{\partial t} = V_p \cdot \frac{\partial C}{\partial x} \cdot \omega_o X \cong \frac{\omega_o Q V_i}{k_{re}} V_p{}^2 (\frac{\partial C}{\partial x})^2 \qquad (2.3)$$

where $\omega_o = 2\pi f_o$ is the radian resonance frequency. In this resonant mode shape, the disk expands along one axis and contracts along the orthogonal axis, thus the resonant frequency can be expressed by the solution of [31]

$$\left[\Psi_n\left(\frac{\zeta}{\xi}\right) - n - q\right] \cdot [\Psi_n(\zeta) - n - q] = (nq - n)^2 \qquad (2.4)$$

where

$$\Psi_n(x) = \frac{x J_{n-1}(x)}{J_n(x)}$$

$$q = \frac{\zeta^2}{2n^2 - 2}$$

$$\zeta = 2\pi f_o R \sqrt{\frac{\rho(2 + 2\sigma)}{E}} \qquad (2.5)$$

$$\xi = \sqrt{\frac{2}{1 - \sigma}}$$

where $J_n(x)$ is a Bessel function of first kind of order n; $\Psi_n(x)$ is modified quotients of $J_n(x)$; R is the radius of resonator disk; ρ, σ and E are the density, Poisson's ratio and Young's modulus of the resonator structural material, respectively. The mode shape of wine-glass appears when n=2. Also, the equation indicates that the resonant frequency f_o of wine-glass mode disk resonator is to the first order inversely proportional to the resonator disk radius R.

2.1.1 Air-Gap Micromechanical Resonators

In the two-port measurement set-up, the wine-glass disk resonator can be expressed in the *RLC* electrical equivalent circuit as shown in Figure 2.1 (b), where C_o is the static capacitance between the disk and input/output electrode; R_x, L_x and C_x are the motional resistance, inductance and capacitance, respectively. When the resonator is excited at its vibration frequency, the impedance of the inductor L_x and capacitor C_x are cancelled out, thus, the motional resistance is determined by the input voltage V_i and output current i_o as following:

$$R_x = \frac{V_i}{i_o} \cong \frac{k_{re}}{\omega_o Q} \cdot V_p^{-2} \cdot \left(\frac{\partial C}{\partial x}\right)^{-2} = \frac{k_{re}}{\omega_o Q V_p^2} \cdot \frac{d_o^4}{\varepsilon_r^2 \varepsilon_o^2 A_o^2} \tag{2.6}$$

where d_o is the electrode-to-resonator gap spacing; ε_r is the relative permittivity of the material used to fill the capacitive transducer gap; ε_o is the permittivity in vacuum; A_o is the electrode-to-resonator overlap area.

(a)   (b)

Figure 2.2 Perspective schematic and cross-section view of capacitively-transduced micromechanical resonators with a pair of air-gap capacitive transducers.

2.1.2 Solid-Gap Micromechanical Resonators

As shown, in order to lower the motional impedance R_x, several approaches could be taken. The first approach is to apply higher dc-bias voltage. However, the applied dc-bias voltage is limited by the pull-in voltage value which is also determined by the gap spacing. Obviously, reducing the gap spacing is the most effective approach among all since the motional resistance is proportional to the fourth power of the gap distance; however, the fabrication limitation has restricted the minimum air gap to about 60nm. Moreover, smaller gap results in smaller pull-in voltage and also the device becomes more nonlinear [32]. Another approach is to increase the electrode-to-resonator overlapping area by enlarging the thickness and radius of the resonator correspondingly. The trade-offs of this approach are the cost and frequency because the frequency is inversely proportional to the resonator critical dimension such as disk radius. Last but not the least is to fill the air gap with a high-k material. Compared to air gap ($\varepsilon_r=1$), the employment of high-k dielectric filled electrode-to-resonator gap is expected to provide a better transducer efficiency as a result of higher permittivity. Although Si_3N_4 has been selected to form the solid transducer gap of wine-glass disk resonators and demonstrated a 8X reduction in series motional resistance [33], it has limitations in its thickness controllability, dielectric constant ($\varepsilon_r=$ 7.8), and high deposition temperature. Therefore, other thin film high-k materials should be explored.

Atomic layer deposition is a thin film deposition technology that self-limits surface reaction down to atomic scale or monolayer level. Taking the advantages of several unique attributes from ALD process including precise thickness control at angstrom to nanometer, conformal coating even on high aspect ratio structures, pinhole and particle free, low deposition temperature (80ºC ~ 300ºC) and very wide variety of high-k materials, ALD has been widely

utilized in the semiconductor industry and MEMS applications [34]. In particular, a wide variety of high-k dielectric thin films including Al_2O_3 (ε_r=8), ZrO_2 (ε_r=12.5), HfO_2 (ε_r=25), TiO_2 (ε_r=80) and BST (ε_r=300) [35] can be seamlessly integrated to serve as the solid gap for the capacitively-transduced MEMS resonators.

$$R_x = \frac{V_i}{i_o} \cong \frac{k_r}{\omega_o Q} \cdot V_p^{-2} \cdot \left(\frac{\partial C}{\partial x}\right)^{-2} = \frac{k_r}{\omega_o Q V_p^2} \cdot \frac{d_o^4}{\varepsilon_r^2 \varepsilon_o^2 A_o^2} \tag{2.7}$$

(a)   (b)
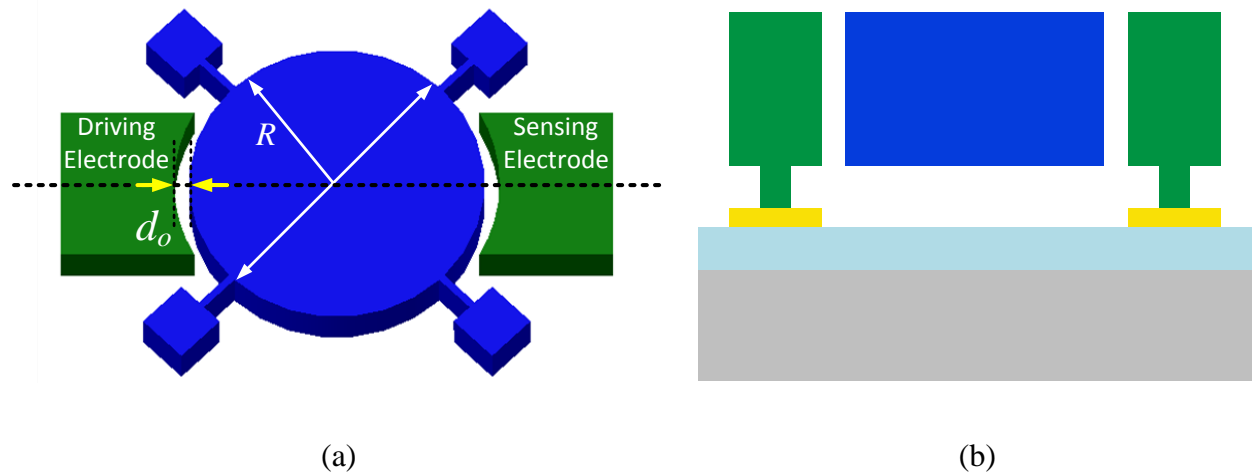
Figure 2.3 Perspective schematic and cross-section view of capacitively-transduced micromechanical resonators with solid-gap capacitive transducers at its input and output ports.

2.1.3 Partially-Refilled Air-Gap Micromechanical Resonators

As discussed previously, reducing the gap spacing is the most effective method to reduce the motional resistance. Unfortunately, due to the limitation of micro fabrication (e.g. thin film deposition and wet releasing), it is very difficult to achieve sub-100 nm air gap in a high-aspect-ratio structure. However, there are several approaches that have been developed to successfully shrink the air gap below 100 nm. One approach is to fabricate the nano-scale gap directly by thermal oxidizing the polysilicon as hard mask and then transfer the trench pattern to silicon nitride and eventually to silicon through DRIE [36]. Due to the side-wall scalloping and

passivation layer formed during the DRIE process, a precise instrument and an optimized recipe are required.

The advent of ALD technology brings thin film deposition down to sub-100 nm and it is capable of controlling the thickness precisely. Therefore, the electrode-to-resonator gap can be defined by ALD and then released by hydrofluoric acid (HF) wet etching. Although the thickness of ALD process can go down to angstrom scale, the wet etchant has difficulties entering into the small gap below about 60 nm due to the surface tension. Thus, HF vapor etching has been applied [37] to achieve a 10 nm air-gap resonator device. It is believed that gas phase etchant is more capable to diffuse into the small gap and also allows the etching by-products to escape from the gap as compared to the liquid phase etchant [38]. However, yield and circuit shortage problems are the major concerns for this method.
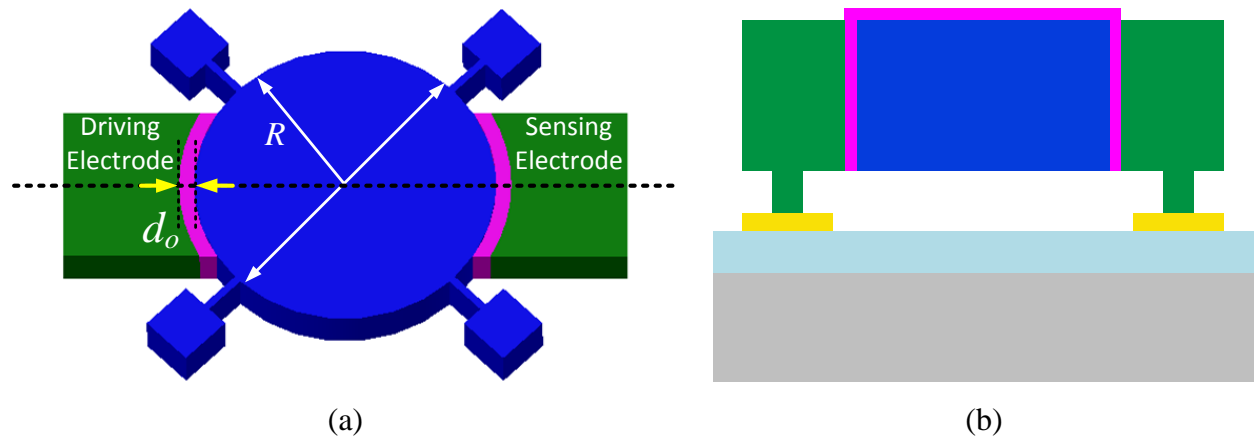

(a)

(b)
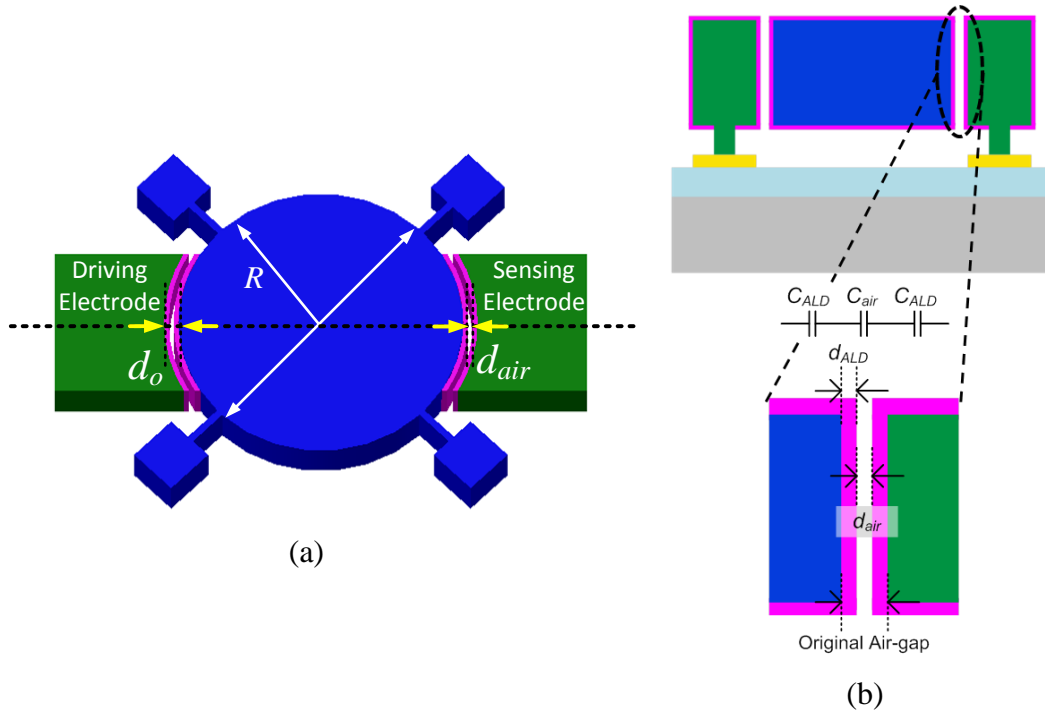
Figure 2.4 Perspective schematic and cross-section view of capacitively-transduced micromechanical resonators with partially-filled air gap.

26

A recently developed partially-refilled air-gap resonator equipped with an electro-to-resonator air gap down to 32 nm which results in significantly lowering down the motional resistance to hundreds of ohms [26, 27]. Instead of defining the sub-100 nm transducer gap from the beginning, an approximate 100 nm-thick oxide material can be deposited by ALD and released by HF wet etching to form an air gap. Again, by taking advantage of ALD's precisely controlled thickness, the air gap is then uniformly filled with about 33 nm-thick dielectric materials on both sides to finally narrow the air gap down to 32 nm as shown in Figure 2.4. The partially-filled air gap not only helps to reduce the motional resistance, but also prevents the resonator from electrostatic discharge because the applied filling high-k material has high permittivity. In order to reduce the motional resistance, the effective transducer gap has to be the air gap other than the entire dielectric-air-dielectric gap. Normally, the equivalent capacitance between the resonator and electrode can be expressed by

$$\frac{1}{C_{eq}} = \frac{1}{C_{ALD}} + \frac{1}{C_{air}} + \frac{1}{C_{ALD}}$$

$$C_{eq} = \frac{C_{air}C_{ALD}}{2C_{air} + C_{ALD}}$$

(2.8)

where C_{air} is air-gap capacitance; C_{ALD} is sold-gap capacitance and two C_{ALD} are identical since ALD provides conformal coating on all surfaces as illustrated in Figure 2.4 (b). If the dimensions of capacitor gap d_{ALD} and d_{air} are set to be closely identical, the equivalent capacitance is then expressed by

$$C_{eq} \cong C_{air}(\frac{2}{\varepsilon_{ALD}} + \frac{1}{\varepsilon_{air}})$$

(2.9)

Also, in order to guarantee that the equivalent capacitance is dominated by air (which is $C_{eq} \cong C_{air}$), the relative permittivity of the filling material need to meet the following condition

$$\varepsilon_{ALD} \gg 20 \tag{2.10}$$

In practical, ε_{ALD} at least needs to be larger than 20, hence, HfO$_2$ (ε_r=25) and TiO$_2$ (ε_r=80) are the reasonable materials among the available selections.

2.2 Atomic Layer Deposition

Figure 2.5 Savannah 100 ALD system by Cambridge Nanotech Inc. used in this work.
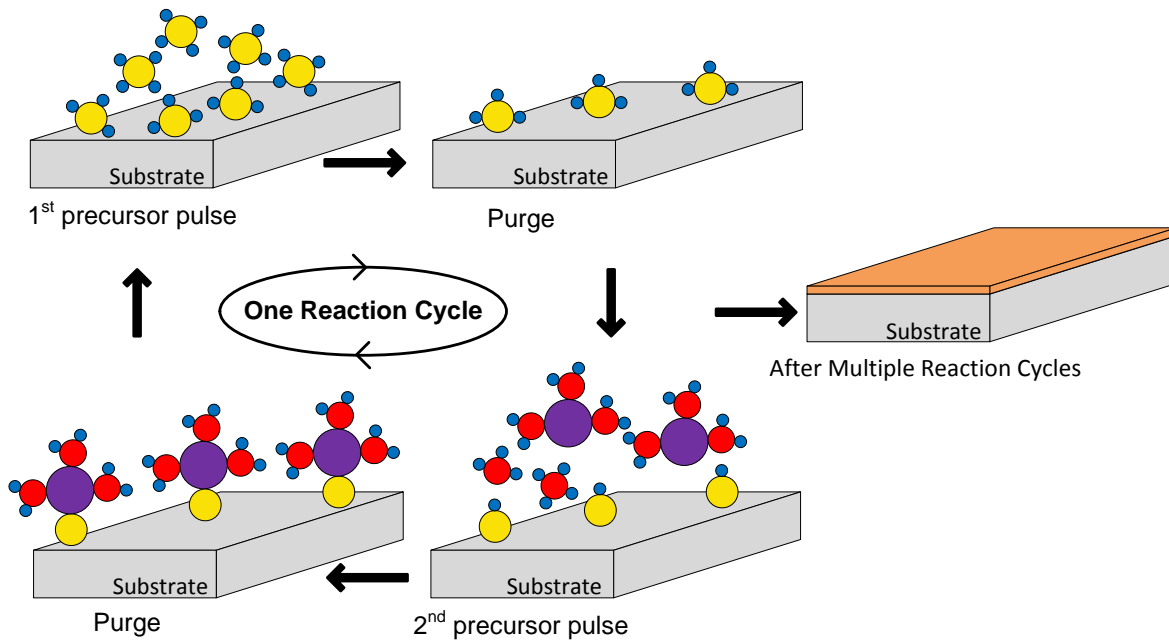
Figure 2.6 Schematic illustration of atomic layer deposition reaction sequence.

Figure 2.6 presents Al_2O_3 thin film deposition process by ALD using water and trimethylaluminum (TMA) precursors at 250°C. The process starts from exposure of the 1st precursor which is water vapor. H_2O vapor is adsorbed on most of the surfaces, forming a hydroxyl group. After purging the reaction chamber, the non-reacted precursors and the gaseous reaction by-products will be removed. Then, the 2nd precursor of TMA is precisely pulsed into the reaction chamber to react with the adsorbed hydroxyl group until the surface is passivated. Neither TMA nor H_2O vapor reacts with itself, which terminates the reaction to one layer and causes the perfect passivation to one atomic layer. After purging the reaction chamber again, the non-reacted precursors and the gaseous reaction by-products will be pumped away. This is the last step of a single cycle for atomic layer deposition, resulting in Al_2O_3 deposition rate of 1.07Å per cycle approximately. After multiple reaction cycles, a uniform, conformal, pinhole and particle free thin film will be deposited through ALD [39].
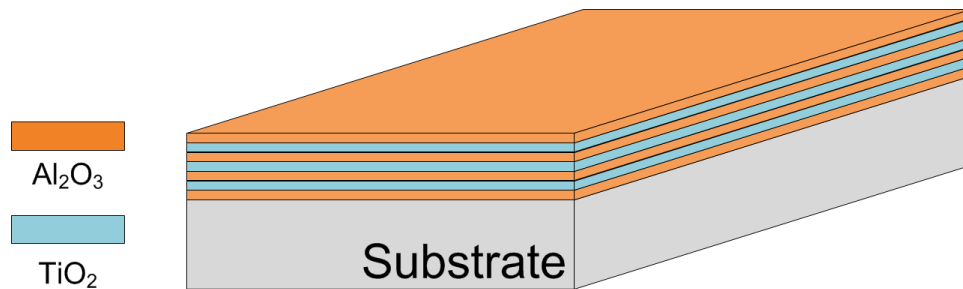
Figure 2.7 Schematic illustration of Nanolaminates with Al_2O_3 and TiO_2 as sub-layers.

Furthermore, a new ALD deposition technique of nanolaminates has been discovered to improve the properties of the dielectric materials and achieve even higher dielectric constant than that of the single dielectric material. To synthesize nanolaminates, two different dielectric materials are deposited alternatingly with nanometer thickness of each as shown in Figure 2.7. The composition of the nanolaminates and the thickness of each material can be modified to

accomplish better dielectric characteristics. Nanolaminates of Al_2O_3 ($\varepsilon_r = 8$) and TiO_2 ($\varepsilon_r = 80$) synthesized by ALD have been systematically investigated to achieve very high dielectric constant ($\varepsilon_r = \sim1,000$) [40] due to the interfacial polarization effects such as the Maxwell-Wagner effect or charge disproportionation in superlattice structures [41].

2.3 Nickel Electroplating

(a)   (b)
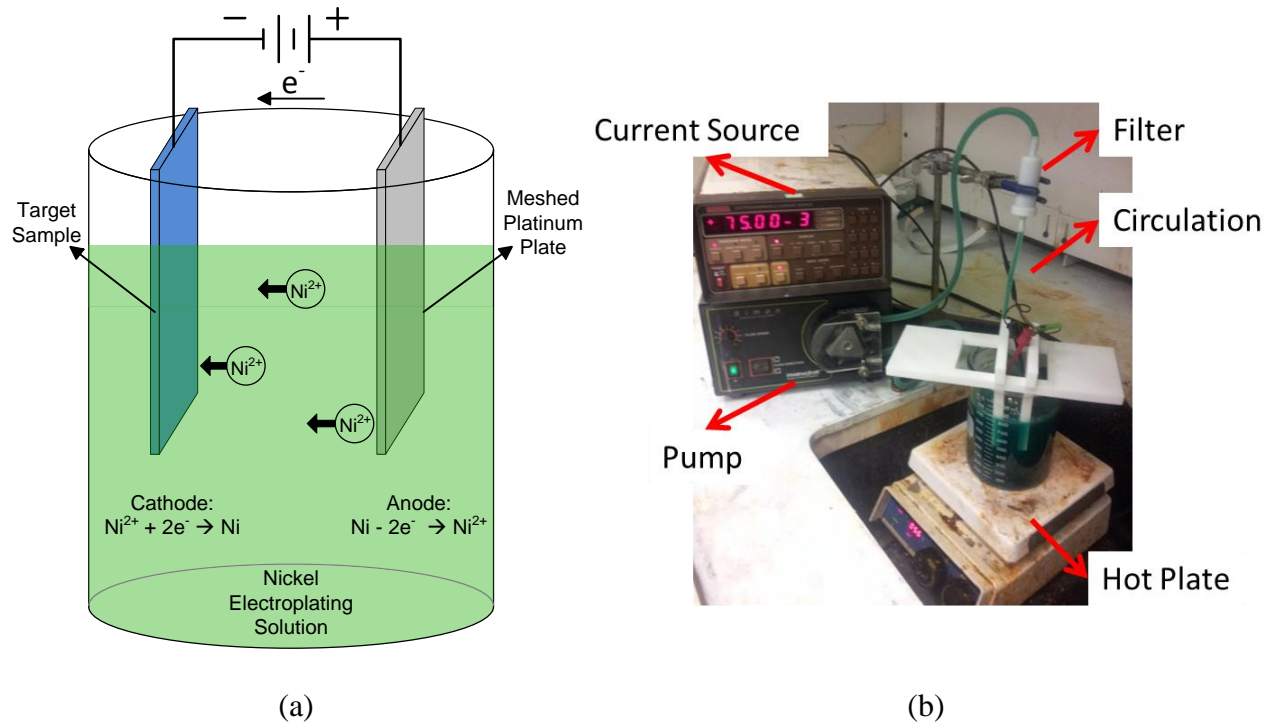
Figure 2.8 (a) Schematic view and (b) experiment set-up of nickel electroplating.

Among the currently available low-temperature materials such as amorphous silicon, germanium, ultrananocrystalline diamond, and other metals, electroplated-nickel was employed here as structural material because of its low deposition temperature, as well as its low cost and the potential for realizing high-aspect-ratio microstructures. Particularly, the electroplating process was conducted in the nickel electroplating solution heated to 40°C ~ 60°C which was low enough to enable the post-transistor fabrication of MEMS devices over the foundry-fabricated electronics.

There are two popular types of electrolyte for nickel electroplating: one is the nickel sulfate ($NiSO_4 \cdot 6H_2O$) which is designed for high speed plating and through-hole metallization; the other one is the nickel sulfamate ($Ni(SO_3NH_2)_2$) which provides low stress and high ductility. The electroplating solution applied here with a pH value of 4.0 was composed of nickel sulfamate, boric acid, nickel chloride and sodium lauryl sulfate. During the electroplating, the target sample was connected to the cathode where Ni^{2+} ions were attracted after giving a current source, while a platinum-meshed plate was connected to the anode where ions were produced for the electrolyte.

Table 2.1 Comparison of Key Material Properties between Nickel and Other MEMS Structural Materials [13]

Material	Young's Modulus E(GPa)	Density ρ (kg/m³)	Acoustic Velocity (m/s)	Deposition Temperature (°C)	Electrical Conductivity (10^7 /Ωm)
PolySilicon	150	2,330	8,024	588	0.001
PolyDiamond	1,144	3,500	18,076	800-1000	0.001
Silicon Carbide	415	3,120	11,500	800	0.00083
Nickel	195	8,900	4,680	40-60	1.43

During the chemical reaction, hydrogen gas was released at the cathode and resulted in pitting at the surface of the plated nickel, raising the pH value of the plating solution and lowering the plating efficiency. Thus, in addition to constantly stirring the electroplating solution by a magnetic stirrer, boric acid was added to maintain the pH value and also help to reduce the pitting and roughness. Nickel chloride is adopted to improve the conductivity. Sodium lauryl

sulfate not only served as auxiliary brightener, but also acted as anti-pitting agent to reduce the surface tension and remove the bubble from the nickel surface [42].

Table 2.2 Composition and Operating Conditions for Nickel Sulfamate Solution

$Ni(SO_3NH_2)_2$, (Nickel Sulfamate)	180 g/L
$NiCl_2 \cdot 6H_2O$, (Nickel Chloride)	4.5 g/L
$B(OH)_3$, (Boric Acid)	22.5 g/L
$CH_3(CH_2)_{11}OSO_3Na$ (Sodium Lauryl Sulfate)	2.7 g/L
Temperature	40-60 °C
Agitation Rate	200 rpm
Current density	1-20 mA/cm²
pH	3.5-4.5

2.4 Distortion in Micromechanical Resonators

To date, capacitively-transduced micromechanical resonators with high frequency-Q performance have been realized an enabler for mixer-filters ("mixlers") [7], on-chip filters and low noise oscillators [43] in wireless communications. Besides the frequency, Q factor, motional impedance, there are several other important parameters (e.g. dynamic range, intercept points, 1dB compression point, etc.) that could determine if the resonator technology is able to be utilized in certain RF communication circuits for the target applications with special specifications. So far, only limited work has been done to study the system linearity of capacitively-transduced MEMS resonators: measured *IIP₃* of -3 dBm for a 10-MHz clamped-clamped beam resonator [32]; measured *IIP₃* of 35.6 dBm at *V*=16 volts for a 8-MHz single-

beam resonator [44]; and measured IIP3 of 19.49 dBm for a 156-MHz contour-mode disk resonator with Q's of 20,500 [45]. Therefore, in order to better tailor the capacitively-transduced MEMS resonators for RF communication circuits, systemic study of system nonlinearity is highly demanded.

2.4.1 Nonlinearity

A system is considered nonlinear if its output is not directly proportional to the input. For a linear system, the characteristic function of the input and output is given by

$$y(t) = \alpha x(t) \tag{2.11}$$

where α is the small-signal gain of the system. For a nonlinear system, the characteristic function of the input and output is given by

$$y(t) = \alpha_o + \alpha_1 x(t) + \alpha_2 x^2(t) + \alpha_3 x^3(t) + \cdots \tag{2.12}$$

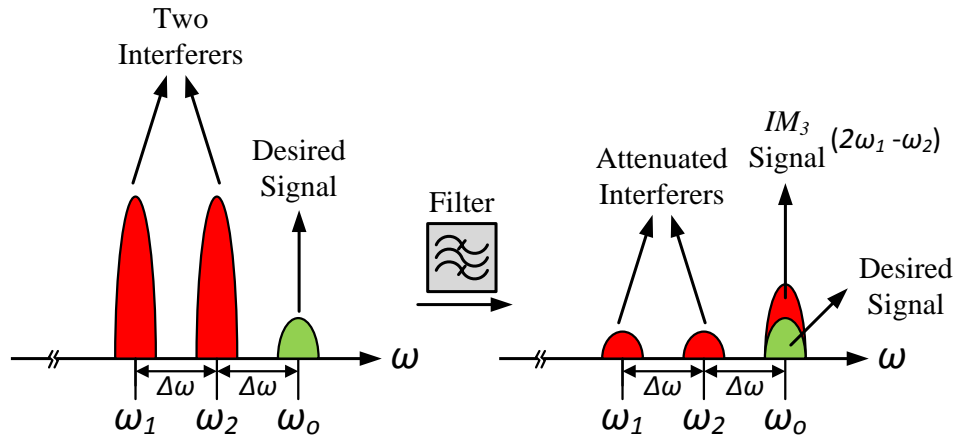### 2.4.2 Fundamentals of Intermodulation Distortion

Figure 2.9 Schematic illustration of signal corruption due to the third-order intermodulation caused by system nonlinearity [32].

Assume $x(t)$ is a sinusoid signal which contains only one frequency, therefore, the generalized sinusoidal wave form can be expressed by

$$x(t) = A cos \omega t \tag{2.13}$$

In a nonlinear system, the input signals consist of a fundamental signal at frequency of ω_o, accompanied with two strong out-of-band interferers which occur at ω_1 and ω_2 and are separated from the fundamental frequency ω_o by $2\Delta\omega$ and $\Delta\omega$, respectively, as shown in Figure 2.9. Thus, the relationship between the fundamental signal and interferers can be expressed by

$$\omega_o = 2\omega_1 - \omega_2 \tag{2.14}$$

These two non-harmonic interfered signals generate additional non-harmonic output frequencies through the nonlinear mixing process which is called intermodulation (IM) [46].

$$S_{in} = A_o \cdot cos\, \omega_o t + A_1 \cdot cos\, \omega_1 t + A_2 \cdot cos\, \omega_2 t \tag{2.15}$$

where A_o is the amplitude of fundamental signal, A_1 and A_2 are the amplitudes of the interfered signals. Then, the output signal of this system is given by

$$S_{out} \approx \alpha_o + \alpha_1 S_{in} + \alpha_2.S_{in}^2 + \alpha_3.S_{in}^3 \tag{2.16}$$

where α_o , α_1, α_2 ..., α_n are the constants, after substituting S_{in} in equation (2.16) with equation (2.15), the output signal can be expanded as:

$$
\begin{aligned}
S_{out} = \alpha_o &+ \alpha_1(A_o \cdot cos\, \omega_o t + A_1 \cdot cos\, \omega_1 t + A_2 \cdot cos\, \omega_2 t) \\
&+ \alpha_2(A_o \cdot cos\, \omega_o t + A_1 \cdot cos\, \omega_1 t + A_2 \cdot cos\, \omega_2 t)^2 \\
&+ \alpha_3(A_o \cdot cos\, \omega_o t + A_1 \cdot cos\, \omega_1 t + A_2 \cdot cos\, \omega_2 t)^3 \\
= \cdots &+ \alpha_1 A_o cos\, \omega_o t + \frac{3\alpha_3 A_1^2 A_2}{4} cos(2\omega_1 - \omega_2)\, t + \cdots
\end{aligned}
\tag{2.17}
$$

where the fundamental component (ω_o) and the third-order intermodulation component ($2\omega_1 - \omega_2$) happened to occur at the same frequency as a sequence of nonlinearity. Therefore, α_3 represents the third-order intermodulation (*IM₃*) distortion generated by the third-order nonlinearity which may disguise the desired signal if α_3 or the magnitudes of interference signals are large enough as illustrated in Figure 2.9.

In order to measure the degree of nonlinearity in a system, a common method of "two-tone" test is applied here which sets the two sinusoid input interference signals to have an equal amplitude A. The input signal is then given by

$$S_{in} = A \cdot \cos \omega_o t + A \cdot \cos \omega_1 t + A \cdot \cos \omega_2 t \tag{2.18}$$

If the amplitude of each tone increases, the output of IM_3 components raises more sharply ($\propto A^3$). As the amplitude continues to increase, the output of IM_3 components will eventually reach the same level as that of the fundamental signal as shown in Figure 2.10. Therefore, the third-order input intermodulation intercept point (IIP_3) is defined as the input amplitude at which the extrapolated IM_3 and the fundamental output components are equal in magnitude. Similarly, the corresponding output is represented by O_{IP_3}.
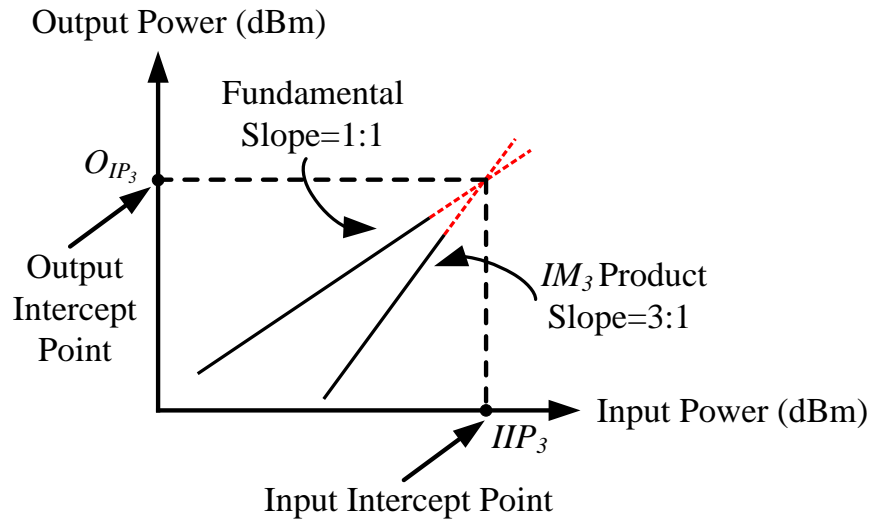

Figure 2.10 Schematic definitions of IM_3 and IIP_3.

To determine the IIP_3, just simply denote the output of the fundamental to be equal to that of the third-order nonlinear product which is given by

$$IIP_3 = A = \sqrt{\frac{4\alpha_1}{3\alpha_3}} \tag{2.19}$$

35

where α_1 and α_3 are not related to any input signals but determined by the linearity of the device. With a higher *IIP$_3$* (higher α_1), the fundamental signal dominates more in the output which indicates the circuit is more linear or can handle lager interferers, and vice versa. Thus, *IIP$_3$* is served as an important metric for the ability of a system to suppress the *IM$_3$* distortion.
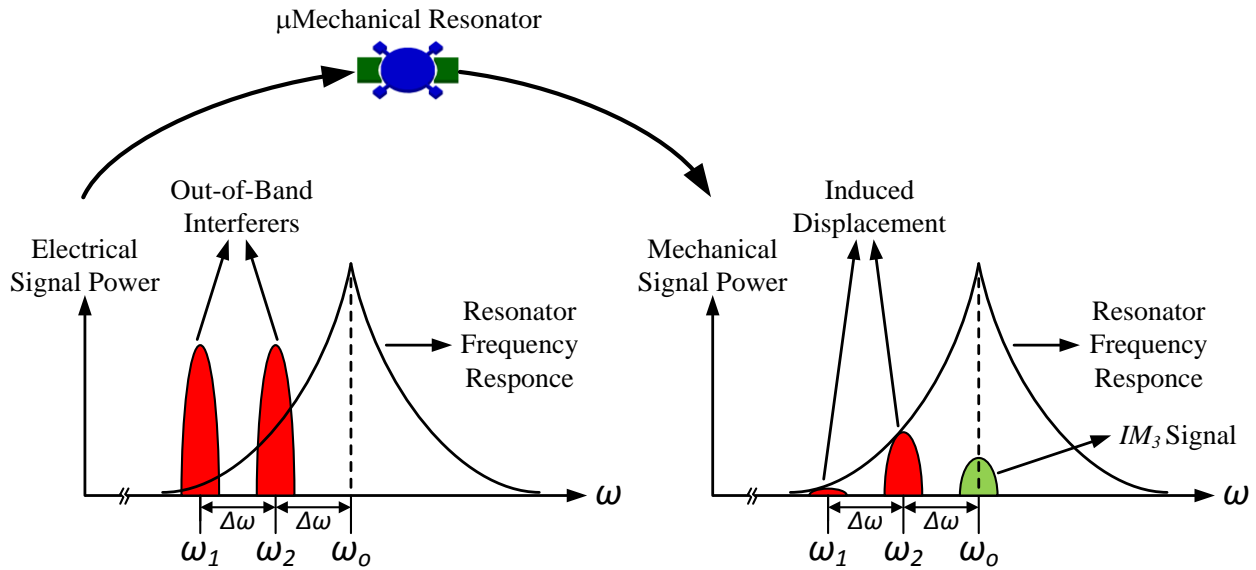

Figure 2.11 Schematic description of the mechanism for *IM$_3$* generation in a capacitively-transduced resonator [32].

2.5 Intermodulation Distortion in MEMS Resonators

In a RF receiver architecture, although these two out-of-band interferers have gone through a band-pass filter, an undesired signal still appears in the target signal channel (as shown in Figure 2.9 and 2.11) which is not acceptable for filtering devices that are designed to eliminate the out-of-band products. Accordingly, in order to circumvent this scenario, the third-order nonlinear term in (2.17) must be constrained below a minimum acceptable value in the practical communication systems.
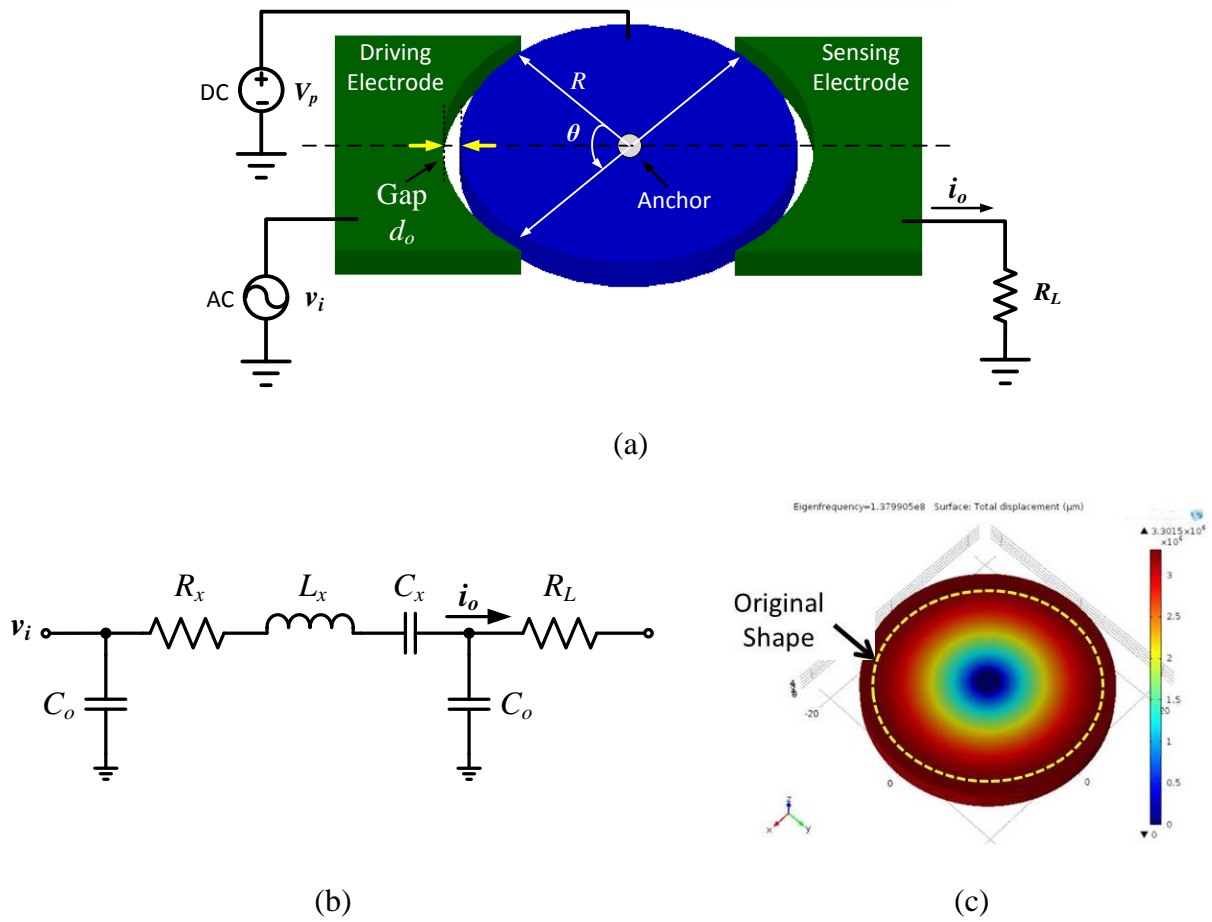
(a)

(b)

(c)

Figure 2.12 (a) Perspective schematic view of an air-gap wine-glass mode disk resonator in the two-port measurement set-up; (b) Equivalent circuit of a contour mode disk resonator; (c) COMSOL simulation of contour mode shape.

In order to excite the device, an alternating AC signal v_i is applied to the input electrodes generating an electrostatic force to drive the resonator to its vibration frequency mode in which it expands and contracts uniformly around its perimeter [19] as illustrated in Figure 2.12. At the same time, a dc-bias voltage V_p is applied directly on the resonant structure forming a capacitance between the resonator disk and the output electrode which introduces an output current i_o. In the two-port measurement set-up, the contour mode disk resonator can be expressed in the *RLC* electrical equivalent circuit in Figure 2.12 (a), where C_o is the static capacitance

between the disk and input/output electrode; R_x, L_x and C_x are the motional resistance, inductance and capacitance, respectively.

So far, two approaches have been adopted when measuring the IIP_3 of micromechanical resonators. One of the prior work [32] presented a traditional "two-tone" test that utilized a power combiner to combine two off-resonance interference signals and then injected it into the electrode of a beam resonator as an input signal. The other work [45] applied two interfering tones to two separated electrodes of the disk resonator without the need of a power combiner, for the purpose of withdrawing nonlinear components generated by the measurement instrument and allowing cleaner third-order nonlinear products to be measured.

As shown in Figure 2.12 (a), a DC-bias voltage is applied to the resonator disk while an AC excitation voltage is applied to the driving electrode, thus, both DC and AC voltages here contribute to the force that drives the resonator into its desired resonance mode. Hence, the driving force can be expressed:

$$F_d = \frac{1}{2}(V_p - v_i)^2 \frac{\partial C}{\partial x} \tag{2.20}$$

where $\partial C / \partial x$ is the integrated change in the electrode-to-resonator overlap capacitance per unit displacement. For the resonator, the value of the disk-to-sense-electrode capacitance as a function of displacement is roughly given by

$$C(x) = \frac{\varepsilon_o A_o}{d_o - x} = C_o (1 - \frac{x}{d_o})^{-1} \tag{2.21}$$

where C_o, A_o and d_o are the static disk-to-electrode capacitance, overlap area and gap spacing, respectively. After differentiating (2.21), $\partial C / \partial x$ can be expressed as

$$\frac{\partial C}{\partial x} = \frac{C_o}{d_o}(1 - \frac{x}{d_o})^{-2} \tag{2.22}$$

If the displacements are small, a Taylor series expansion may be performed in (2.22), yielding

$$\frac{\partial C}{\partial x} = \frac{C_o}{d_o}(1 + \frac{2}{d_o}x + \frac{3}{d_o{}^2}x^2 + \frac{4}{d_o{}^3}x^3 + \cdots) \tag{2.23}$$

After applying (2.23) to (2.20), the driving force can be expanded as following [47]:

$$F_d = \frac{1}{2}(V_p - v_i)^2 \cdot (\frac{C_o}{d_o}) \cdot (1 + \frac{2}{d_o}x + \frac{3}{d_o{}^2}x^2 + \frac{4}{d_o{}^3}x^3 + \cdots) \tag{2.24}$$

Here, in a nonlinear system, the two off-resonance interferers that occur at ω_1 and ω_2 and are separated from the fundamental frequency ω_o by $2\Delta\omega$ and $\Delta\omega$, respectively, are applied to the input electrodes. Therefore, the effective excitation voltage is the sum of two tone signals as following:

$$v_i = V_1 \cdot cos(\omega_1 t) + V_2 \cdot cos(\omega_2 t) \tag{2.25}$$

where $2\omega_1 - \omega_2 = \omega_o$. Then the mechanical displacement can be expanded as

$$x = X_1 \cdot cos(\omega_1 t + \phi_1) + X_2 \cdot cos(\omega_2 t + \phi_2) \tag{2.26}$$

where the amplitude X_1 and X_2 can be obtained from the voltage-to-displacement transfer function of the mechanical resonator as following:

$$X_{1,2}(j\omega) = \frac{F}{k_{re}} \cdot \Theta(\omega) \cong \frac{V_p V_i}{k_{re}} \cdot \frac{C_o}{d_o} \cdot \Theta_{1,2}(\omega) \tag{2.27}$$

where k_{re} is the effective stiffness at any location on the disk perimeter; and the transfer functions of two interfering tones are given by

$$\Theta_{1,2}(\omega) = \frac{1}{1 - \left(\frac{\omega_{1,2}}{\omega_o}\right)^2 + j\left(\frac{\omega_{1,2}}{Q\omega_o}\right)} \tag{2.28}$$

By setting the input voltage amplitudes as V_i and inserting (2.25) and (2.26) into (2.24), the total driving force can be solved including the force of a third-order intermodulation component, which can be expressed as [45]

$$F_{IM_3} = V_i^3 \cdot \left\{ \frac{1}{2} \frac{\varepsilon_o^2 A_o^2}{d_o^5} \frac{V_p}{k_{re}} \Theta_1 + \frac{1}{4} \frac{\varepsilon_o^2 A_o^2}{d_o^5} \frac{V_p}{k_{re}} \Theta_2^* + \frac{3}{4} \frac{\varepsilon_o^3 A_o^3}{d_o^8} \frac{V_p^3}{k_{re}^2} \Theta_1^2 \right.$$

$$\left. + \frac{3}{2} \frac{\varepsilon_o^3 A_o^3}{d_o^8} \frac{V_p^3}{k_{re}^2} \Theta_1 \Theta_2^* + \frac{3}{2} \frac{\varepsilon_o^4 A_o^4}{d_o^{11}} \frac{V_p^5}{k_{re}^3} \Theta_1^2 \Theta_2^* \right\}$$

(2.29)

It is known that the fundamental force component can be expressed by

$$F = V_p \cdot V_i \cdot \frac{\partial C}{\partial x} = V_p \cdot V_i \cdot \frac{\varepsilon_o A_o}{d_o^2}$$

(2.30)

At the extrapolated input power, the third-order intermodulation components in a two-tone test have the same value as the linear force component. By equating the IM_3 force (2.29) to the fundamental force (2.30) and solving for $V_{IIP_3} = V_i$, then the input voltage magnitude at the IIP_3 is explained as following:

$$V_{IIP_3} = \left\{ \frac{\varepsilon_o A_o}{2 k_{re} d_o^3} \Theta_1 + \frac{\varepsilon_o A_o}{4 k_{re} d_o^3} \Theta_2^* + \frac{3 \varepsilon_o^2 A_o^2 V_p^2}{4 k_{re}^2 d_o^6} \Theta_1^2 + \frac{3 \varepsilon_o^2 A_o^2 V_p^2}{2 k_{re}^2 d_o^6} \Theta_1 \Theta_2^* \right.$$

$$\left. + \frac{3 \varepsilon_o^3 A_o^3 V_p^4}{2 k_{re}^3 d_o^9} \Theta_1^2 \Theta_2^* \right\}^{-\frac{1}{2}}$$

(2.31)

Therefore the power of IIP_3 can be expressed as

$$P_{IIP_3} = \frac{V_{IIP_3}^2}{2(R_x + 50\Omega)}$$

(2.32)

where 50Ω is the load resistance representing the measurement instrument.

The completed equations for calculating the equivalent mass and stiffness of contour-mode disk resonators can be found in [19]:

$$m_{re} = \frac{KE_{tot}}{\frac{1}{2}v'(R_{disk},\theta)^2} = \frac{2\pi\rho\, t \int_0^{R_{disk}} r\, J_1{}^2\left(\frac{\omega_o}{C_{QL}}r\right)dr}{J_1{}^2\left(\frac{\omega_o}{C_{QL}}R_{disk}\right)}$$ (2.33)

where the equivalent mass, m_{re}, at a location (R_{disk} ,θ) can be obtained by dividing the total

kinetic energy by one-half the square of the velocity at that location; KE_{tot} is the total kinetic

energy in a vibrating disk obtained by integrating the kinetic energies of all infinitesimal mass

elements; $v'(R_{disk},\theta)$ is the velocity magnitude at location (R_{disk} ,θ); C_{QL} is quasi-longitudinal

wave speed; J_n is Bessel function of first kind of order n. Thereafter, the equivalent stiffness can

be expressed as:

$$k_{re} = \omega_o{}^2 \cdot m_{re}$$ (2.34)

2.5.1 *IIP₃* of Air-gap Resonators

(a)   (b)
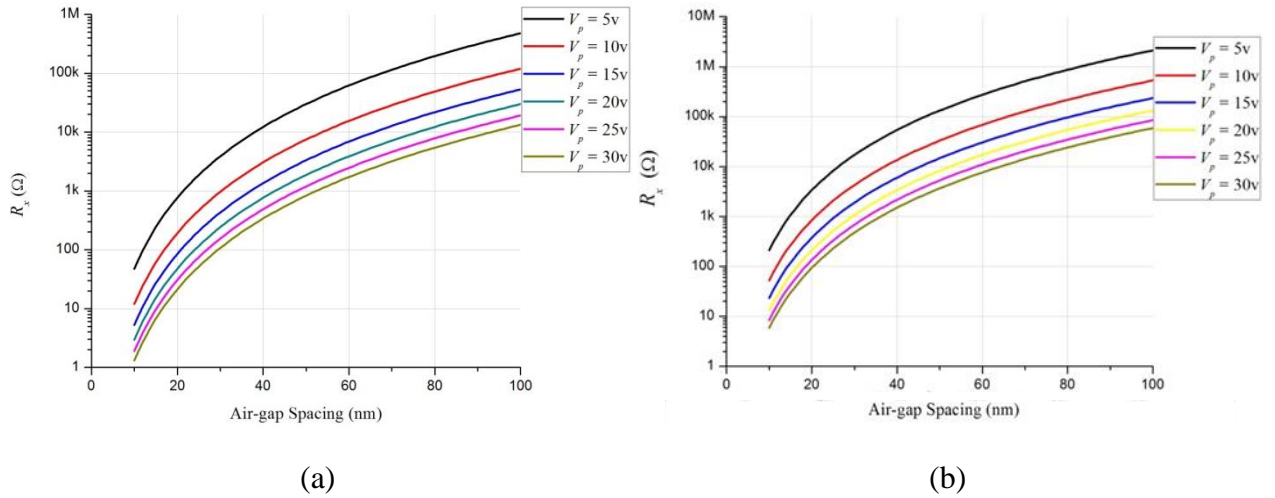
Figure 2.13 Simulated motional impedance of (a) polysilicon resonators; and (b) electroplated
nickel resonators depending upon capacitive disk-to-electrode gap spacing and applied DC-bias
voltages.

By taking polysilicon as structural material, the simulated motional impedance is based

on the device with specifications including disk radius of 30 μm, thickness of 4 μm, and quality

factor of 10,000. By considering electroplated nickel as structural material, the simulation results

are based on the device with specifications including disk radius of 30 µm, thickness of 4 µm, and quality factor of 5,000. As shown, the motional impedance is highly dependent on the air-gap spacing and applied DC-bias voltage. Since the material loss of nickel is higher than silicon, the quality factor for the nickel devices under similar conditions will be lower than that of silicon devices, which results in the difference of the motional resistance.
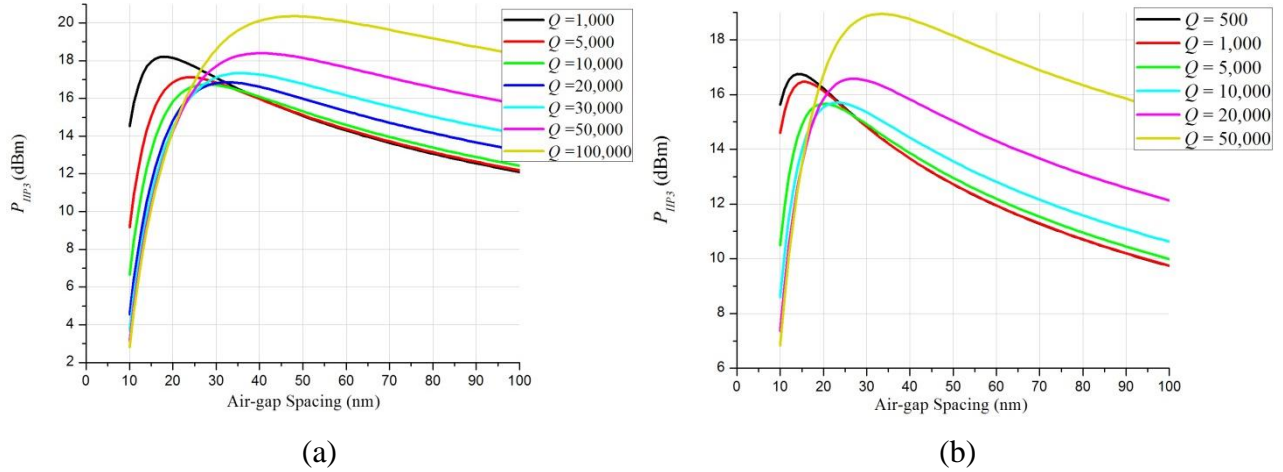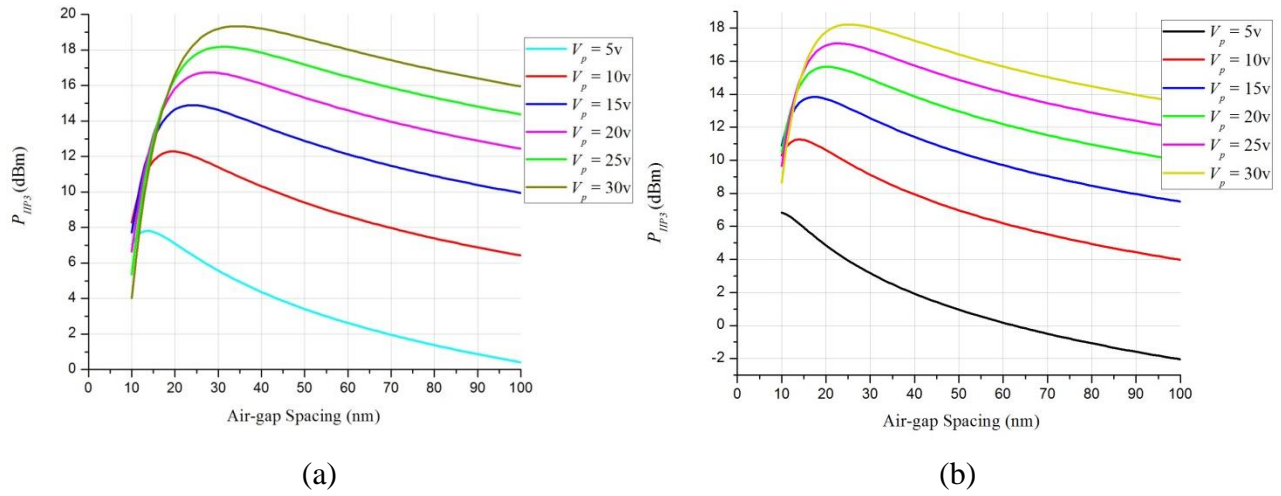

(a)   (b)

Figure 2.14 Simulated *IIP₃* of (a) polysilicon resonators; and (b) electroplated nickel resonators depending upon capacitive disk-to-electrode gap spacing and different Q factor.

By taking polysilicon as structural material, the *IIP₃* simulation results are based on the device with specifications including disk radius of 30 µm, thickness of 4 µm, and applied bias voltage of 20 volts. By considering electroplated nickel as structural material, the *IIP₃* simulation results are based on the device with specifications including disk radius of 30 µm, thickness of 4 µm, and applied bias voltage of 20 volts. As shown in equation (2.6), the motional resistance is inversely proportional to the Q factor and P_{IIP3} is inversely proportional to the motional resistance. Meanwhile, the voltage of *IIP₃* is also inversely proportional to the Q factor. However, the motional resistance decreases faster than the voltage of *IIP₃* when Q factor increases up to 10,000. Therefore, the *IIP₃* decreases as Q increases in this region. After the Q factor is greater than 10,000, the *IIP₃* becomes proportional to the Q factor.

Figure 2.15 (a) presents the simulated results of *IIP₃* based on the device with polysilicon as structural layer, disk radius of 30 μm, thickness of 4 μm, and quality factor of 10,000. By taking electroplated nickel as structural material, the simulation results in Figure 2.15 (b) are based on the device with a disk radius of 30 μm, thickness of 4 μm, and quality factor of 5,000. Since the motional resistance is highly proportional to the bias voltage V_p, while *IIP₃* is not dependent on it, the *IIP₃* increases when higher bias voltage applied.

Figure 2.15 Simulated *IIP₃* of (a) polysilicon resonators; and (b) electroplated nickel resonators depending upon capacitive disk-to-electrode gap spacing and applied DC-bias voltages.

Figure 2.16 (a) presents the simulated results of *IIP₃* based on the device with polysilicon as structural layer, thickness of 4 μm, applied bias-voltage of 20 volts, and quality factor of 10,000 with varies disk radius from 5 μm to 50 μm. By taking electroplated nickel as structural material, the simulation results in Figure 2.16 (b) are based on the device with thickness of 4 μm, applied bias-voltage of 20 volts, and quality factor of 5,000 with varies disk radius from 5 μm to 50 μm. The comparison shows that the smaller size device gains higher power of *IIP₃*, but no significant improvement on it. It is because the smaller device provides less overlapping area as a trade-off of higher frequencies which actually increases the motional resistance.
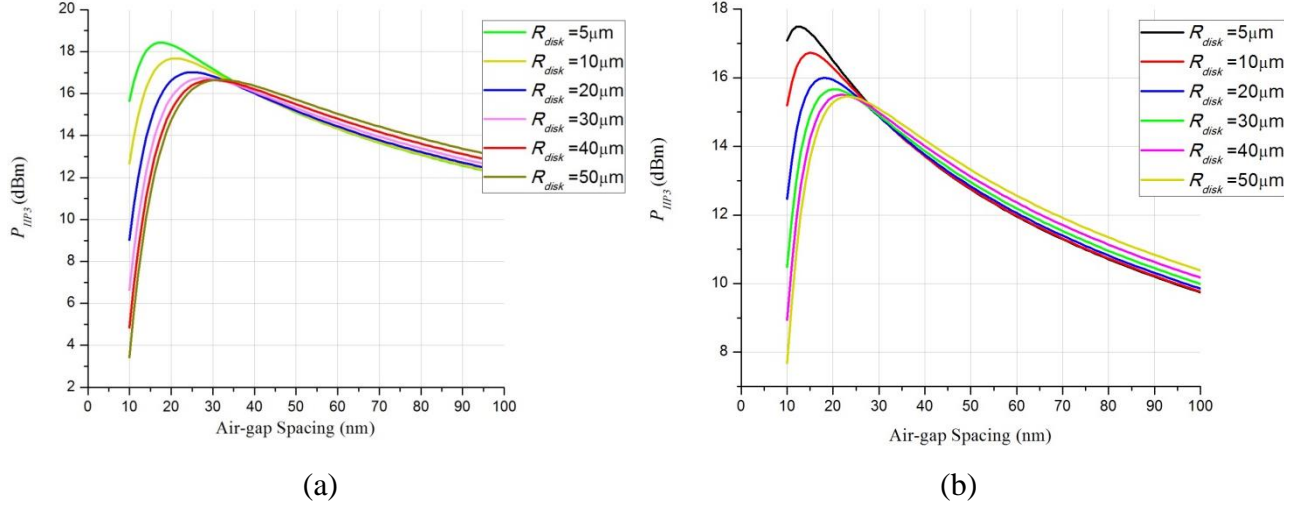
(a)   (b)

Figure 2.16 Simulated *IIP₃* of (a) polysilicon resonators; and (b) electroplated nickel resonators depending upon capacitive disk-to-electrode gap spacing and radius of resonator disk.

2.5.2 *IIP₃* of Solid-gap Resonators

Compare to air-gap resonators, solid-gap resonators can provide much lower motional resistance by applying both high-k gap material and much smaller resonator-to-electrode gap. However, the motional resistance only slightly decreased according to the device measurement results [35] due to the increased stiffness as compared to that of air gap. Thus, the motional resistance of a solid-gap resonator can be approximately expressed by [35]

$$R_x = \frac{V_i}{i_o} \cong \frac{k_r}{\omega_o Q} \cdot V_p^{-2} \cdot \left(\frac{\partial C}{\partial x}\right)^{-2} = \frac{k_r}{\omega_o Q V_p^2} \cdot \frac{d_o^4}{\varepsilon_r^2 \varepsilon_o^2 A_o^2} \cdot \frac{1}{\gamma} \tag{2.34}$$

where γ is a modified quotient of stiffness between the solid gap and surrounding electrode plates that at present is empirically extracted from the measurement results.

2.5.3 *IIP₃* of Partially-filled Air-gap Resonators

By taking into account the effect of the dielectric material which forms a partially-filled capacitive gap, the equivalent capacitance can be expressed as

$$C_{eq} = \frac{C_{air}C_{ALD}}{2C_{air} + C_{ALD}} = \frac{\dfrac{\varepsilon_o A_o}{d_1 - x} \cdot \dfrac{\varepsilon_o \varepsilon_r A_o}{(d_1 - d_o)/2}}{\dfrac{2\varepsilon_o A_o}{d_1 - x} + \dfrac{\varepsilon_o \varepsilon_r A_o}{(d_1 - d_o)/2}} \tag{2.35}$$

where d_o is the spacing of the original released air gap; d_1 is the spacing of final air gap after partially filled with ALD material; ε_r is permittivity of filled ALD high-k material. Then the differential of equivalent capacitance can be expressed as

$$\frac{\partial C_{eq}}{\partial x} = \frac{\varepsilon_o A_o}{\left(\dfrac{d_o - d_1}{\varepsilon_r} + d_1\right)^2} \cdot \left(1 - \frac{x}{\dfrac{d_o - d_1}{\varepsilon_r} + d_1}\right)^{-2} \tag{2.36}$$

If the displacements are small, a Taylor series expansion may be performed in (2.36), yielding

$$\frac{\partial C_{eq}}{\partial x} = \frac{\varepsilon_o A_o}{D^2}\left(1 + \frac{2}{D}x + \frac{3}{D^2}x^2 + \frac{4}{D^3}x^3 + \cdots\right) \tag{2.37}$$

where

$$D = \frac{d_o - d_1}{\varepsilon_r} + d_1 \tag{2.38}$$

Along with the vibration, the time-varying capacitance between the disk and output electrode also produces an output current expressed by

$$i_o = V_p \cdot \frac{\partial C_{eq}}{\partial t} = V_p \cdot \frac{\partial C_{eq}}{\partial x} \cdot \frac{\partial x}{\partial t} = V_p \cdot \frac{\partial C_{eq}}{\partial x} \cdot \omega_o X \cong \frac{\omega_o Q V_i}{k_r} V_p^2 \left(\frac{\partial C_{eq}}{\partial x}\right)^2 \tag{2.39}$$

The motional resistance is determined by the input voltage V_i and output current i_o as following

$$R_x = \frac{V_i}{i_o} \cong \frac{k_{re}}{\omega_o Q} \cdot V_p^{-2} \cdot \left(\frac{\partial C}{\partial x}\right)^{-2} = \frac{k_{re}}{\omega_o Q V_p^2} \cdot \frac{D^4}{\varepsilon_o^2 A_o^2} \tag{2.40}$$

By taking the same procedure as that of air gap scenario, the driving force of third-order intermodulation component can be expressed as

$$F_{IM_3} = V_i^3 \cdot \left\{ \frac{1}{2} \frac{\varepsilon_o^2 A_o^2}{D^5} \frac{V_p}{k_{re}} \Theta_1 + \frac{1}{4} \frac{\varepsilon_o^2 A_o^2}{D^5} \frac{V_p}{k_{re}} \Theta_2^* + \frac{3}{4} \frac{\varepsilon_o^3 A_o^3}{D^8} \frac{V_p^3}{k_{re}^2} \Theta_1^2 \right.$$

$$\left. + \frac{3}{2} \frac{\varepsilon_o^3 A_o^3}{D^8} \frac{V_p^3}{k_{re}^2} \Theta_1 \Theta_2^* + \frac{3}{2} \frac{\varepsilon_o^4 A_o^4}{D^{11}} \frac{V_p^5}{k_{re}^3} \Theta_1^2 \Theta_2^* \right\} \tag{2.41}$$

As a sequence, the input voltage magnitude at the *IIP₃* is given by

$$V_{IIP_3} = \left\{ \frac{\varepsilon_o A_o}{2\, k_{re}\, D^3} \Theta_1 + \frac{\varepsilon_o A_o}{2\, k_{re}\, D^3} \Theta_2^* + \frac{3\, \varepsilon_o^2 A_o^2\, V_p^2}{4\, k_{re}^2\, D^6} \Theta_1^2 + \frac{3\, \varepsilon_o^2 A_o^2\, V_p^2}{2\, k_{re}^2\, D^6} \Theta_1 \Theta_2^* \right.$$

$$\left. + \frac{3\, \varepsilon_o^3 A_o^3\, V_p^4}{2\, k_{re}^3\, D^9} \Theta_1^2 \Theta_2^* \right\}^{-\frac{1}{2}} \tag{2.42}$$

Thereafter, the power of *IIP₃* in a partially-filled air-gap resonator can be expressed as

$$P_{IIP_3} = \frac{V_{IIP_3}^2}{2(R_x + 50\Omega)} \tag{2.43}$$
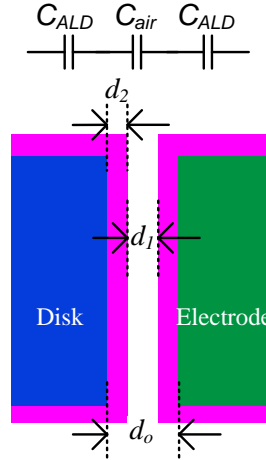
Figure 2.17 Schematic cross-section view of a partially-filled air-gap resonator.

Figure 2.18 presents the simulated motional impedance based on a polysilicon resonator device with disk radius of 30 µm, thickness of 4 µm, the initial released air gap of 100 µm, and applied ALD filling material of HfO_2, TiO_2 and BST.
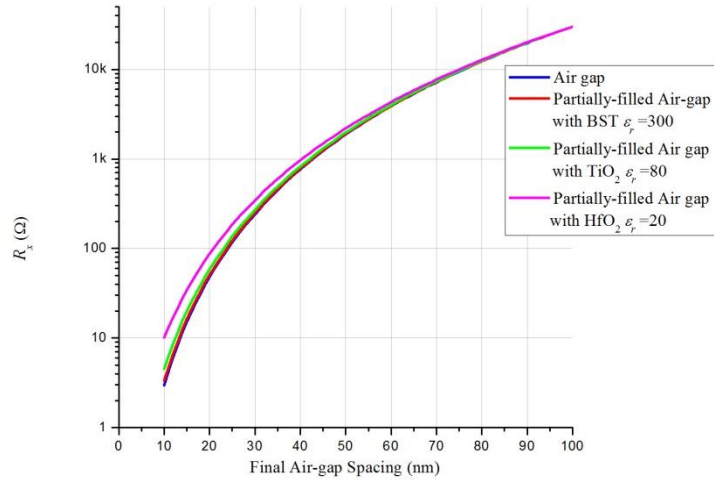
Figure 2.18 Simulated motional impedances as a function of the gap spacing and partially-filled air gap materials.
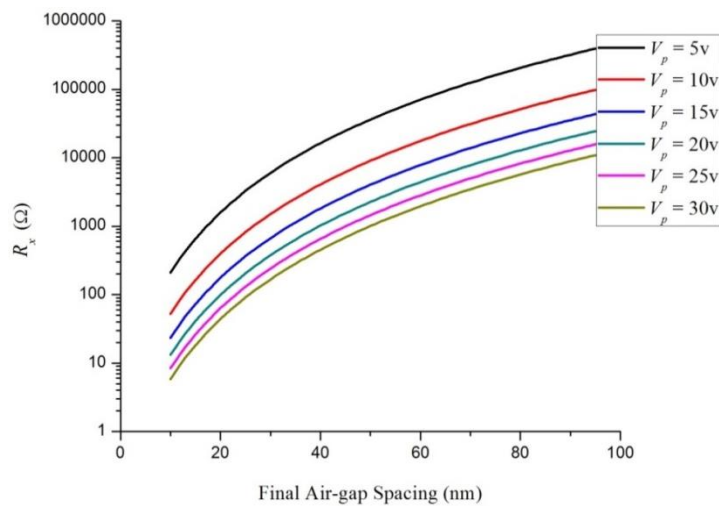
Figure 2.19 Simulated motional impedances as a function of air-gap spacing and applied bias voltages.

Under a common DC-bias voltage of 25 volts, Figure 2.18 shows the comparison of simulated motional resistance between air-gap resonator and partially-filled air-gap resonator. As for the partially-filled air-gap device, the motional resistance is not much higher than the air-gap device when the final air-gap spacing is below 20nm because the air-gap capacitance is not dominated in the overall capacitance. However, the air-gap device may only be released with air-

gap spacing above 60 nm. Therefore, the partially-filled air-gap device has further advantages of reducing the motional resistance while having a decent fabrication yield.

Figure 2.19 presents the simulated motional impedances for a resonator with partially-filled air gap. As shown, when the applied DC-bias voltage increased, the motional resistance was reduced significantly.

CHAPTER 3 ELECTROPLATED-NICKEL MEMS RESONATORS

3.1 Measurement Set-up

The RF measurement was conducted through either wire-bonding or on-chip probing in both air and vacuum with equipment including a network analyzer, a signal generator, a spectrum analyzer, a signal generator, a power supply, a vacuum chamber and a probe station.
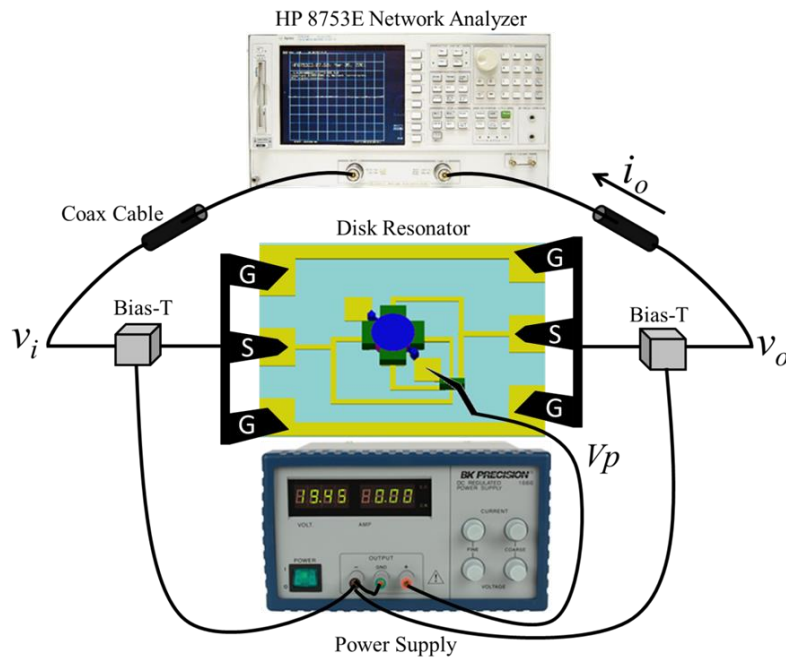
Figure 3.1 Schematic measurement set-up for nickel disk resonators.

In order to measure the resonance frequency and quality factor, Figure 3.1 presents a two-port measurement set-up, which consists of a disk resonator with key features such as driving and sensing ports, and testing instruments. In order to excite the device, an alternating AC signal V_i is applied to the input electrodes generating an electrostatic force to drive the resonator to its vibration resonance mode. At the same time, a DC-bias voltage V_p is applied directly on the

resonant structure forming a DC-biased time varying capacitance between the resonator disk and the output electrodes which induces an output current i_o.

3.2 Solid-Gap Resonator Fabrication Process

Figure 3.2 presents a step-by-step fabrication process flow for a solid-gap capacitively-transduced resonator using electroplated nickel as its structural material. Starting with a standard silicon wafer, a 1µm-thick silicon dioxide was coated through thermal oxidation to serve as an isolation layer. By applying the first photomask, the Cr/Au bottom electrodes were defined by means of UV photolithography, e-beam evaporation and lift-off process. Then a 1µm-thick amorphous silicon (α-Si) layer was deposited by plasma enhanced chemical vapor deposition (PECVD) to serve as a sacrificial layer. After utilizing the second photomask and UV photolithography, the photoresist patterns were then transferred to α-Si by silicon dry etching, thus forming via holes as the anchors of the resonator disk and electrodes. Followed by blanket deposition of Cr/Au seeding layers, AZ P4620 photoresist mold was then patterned using the third photomask. A 5µm-thick nickel microstructure was electroplated inside the mold to form the body of the disk resonator. After soaking in the solvent and metal etchant to remove the mold and seeding layers, respectively, a 30nm-thick HfO_2 film was deposited by ALD to uniformly cover the sidewall of the resonators to define the electrode-to-resonator capacitive gap as shown in Figure 3.2(c). Followed by photolithography of the fourth photomask, the sidewall dielectric film was protected by the photoresist whereas the field HfO_2 film was removed by dry etching to make contact to the bottom electrodes. Next, with the last photomask, molding process along with electroplating was employed again to form the surrounding electrodes for the MEMS resonators. Finally, a unique isotropic silicon dry etching process through DRIE was adopted to selectively etch away the amorphous silicon sacrificial layer resulting in suspended resonator

structures made of electroplated nickel. The final device cross-sectional structure is illustrated in Figure 3.2 (j).
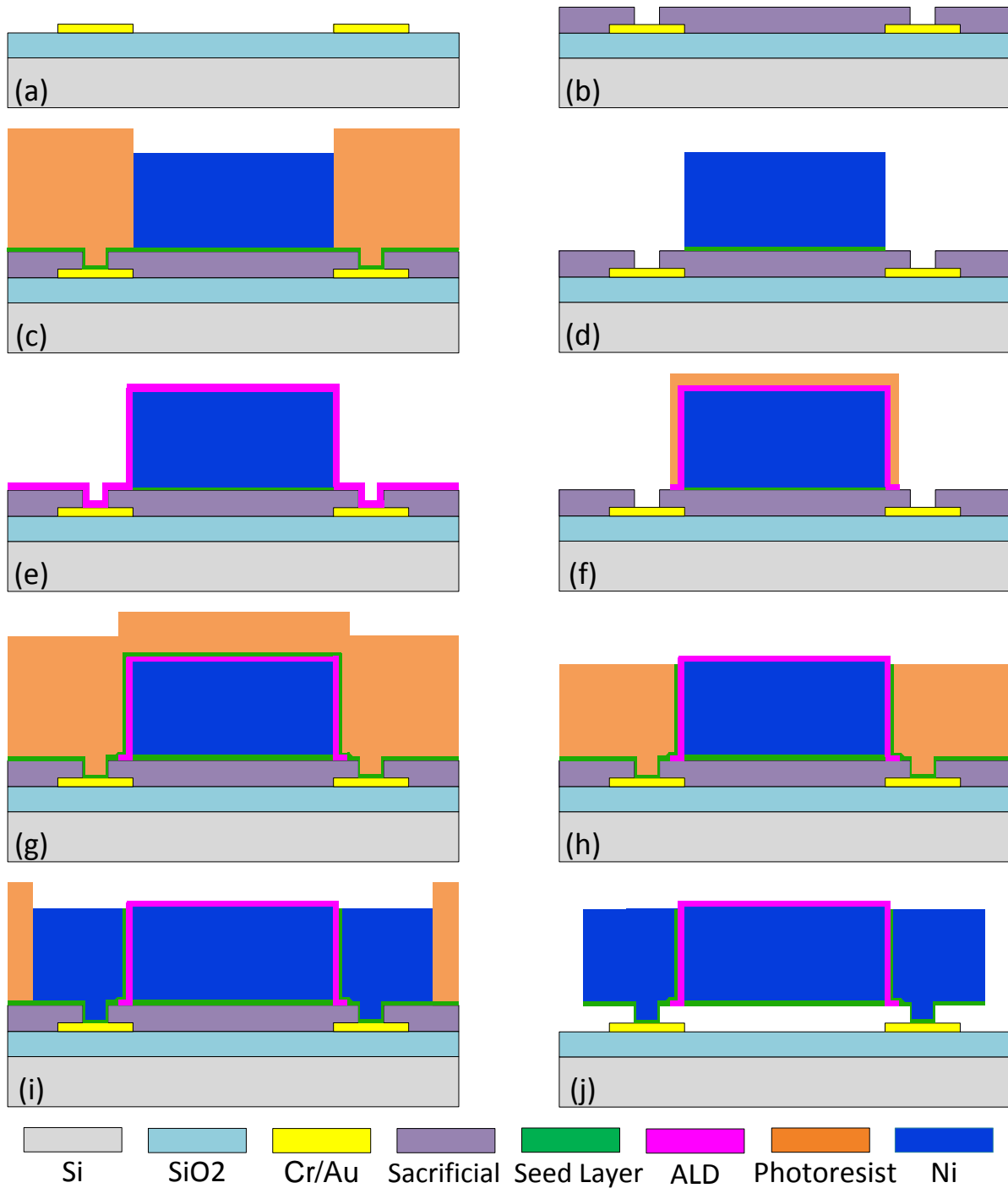
Figure 3.2 Fabrication process flow of a solid-gap capacitively-transduced nickel resonator.
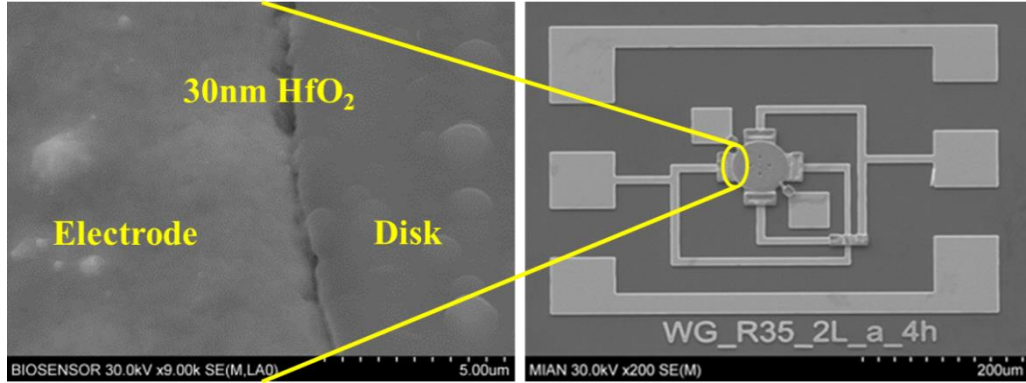
Figure 3.3 SEM image of electroplated-Ni wine-glass mode disk resonator with a solid gap of 30nm.

After 20 minutes isotropic silicon etching in an inductively-coupled plasma etcher, the nickel resonator was released along with the pre-defined 30 nm HfO_2 electrode-to-disk solid capacitive gap as shown in Figure 3.3. Also, the Cr/Au bottom electrodes were exposed for on-chip probing in air or wire-bonding in vacuum measurement. Since the gap spacing of this solid-gap device is smaller than the typical air gap, the pull-in voltage was only about 5 volts.
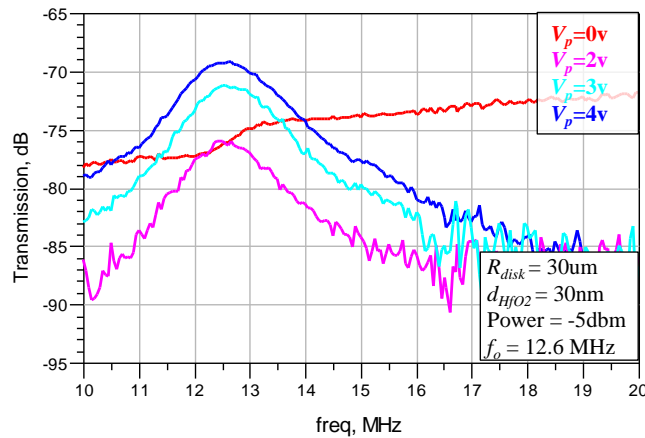
Figure 3.4 Measurement results of electroplated-Ni wine-glass mode disk resonator with solid gap of 30nm.

The measurement results in Figure 3.4 were based on a wine-glass mode disk resonator with radius of 30 μm, thickness of 5um, and a solid gap of 30 nm. The applied DC-bias voltage was from 2 volts to 4 volts and the device was pulled-in after 5 volts.

Figure 3.5 presents the measured frequency response of a wine-glass mode disk resonator with radius of 20 µm, thickness of 5 µm and a solid-gap of 30 nm. The applied DC-bias voltage was 4 volts and the device was pulled-in after 5 volts. The extrapolated Young's Modulus of electroplated nickel in this device is roughly 190 GPa that is on par with the prior reports.
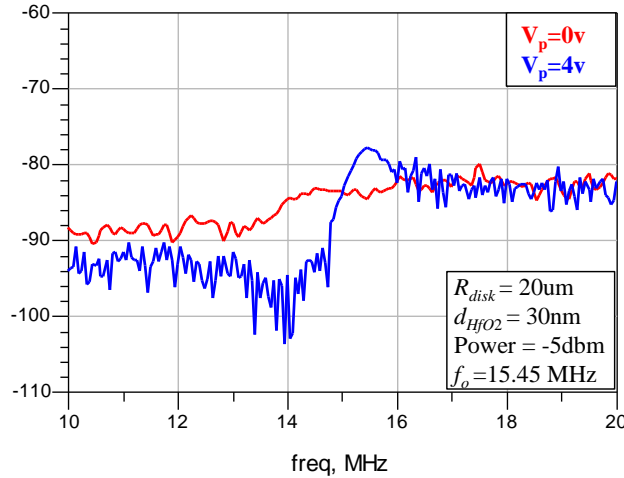
Figure 3.5 Measurement results of electroplated-Ni wine-glass mode disk resonator with solid gap of 30nm.

3.3 Air-Gap Resonator Fabrication Process

Figure 3.6 presents a step-by-step fabrication process flow for air-gap capacitively-transduced resonator using electroplated nickel as its structural material. Apart from the solid-gap devices, a high resistivity (6kΩ·cm) silicon wafer was employed here so that the isolation layer is not necessary for keeping low feed-through level from the substrate. By utilizing the same photomask set for the solid-gap resonators, the fabrication process of air-gap resonators was performed similar to the solid-gap process. By applying the first photomask, the Cr/Au bottom electrodes were defined by means of UV photolithography, e-beam evaporation and a lift-off process. Instead of amorphous silicon, 1µm-thick silicon dioxide was coated here by PECVD at 250°C to serve as sacrificial layer. After utilizing the second photomask and UV

53

photolithography, the photoresist patterns were then transferred to silicon dioxide by dry etching, thus forming via holes as the anchors of resonator disk and electrodes.
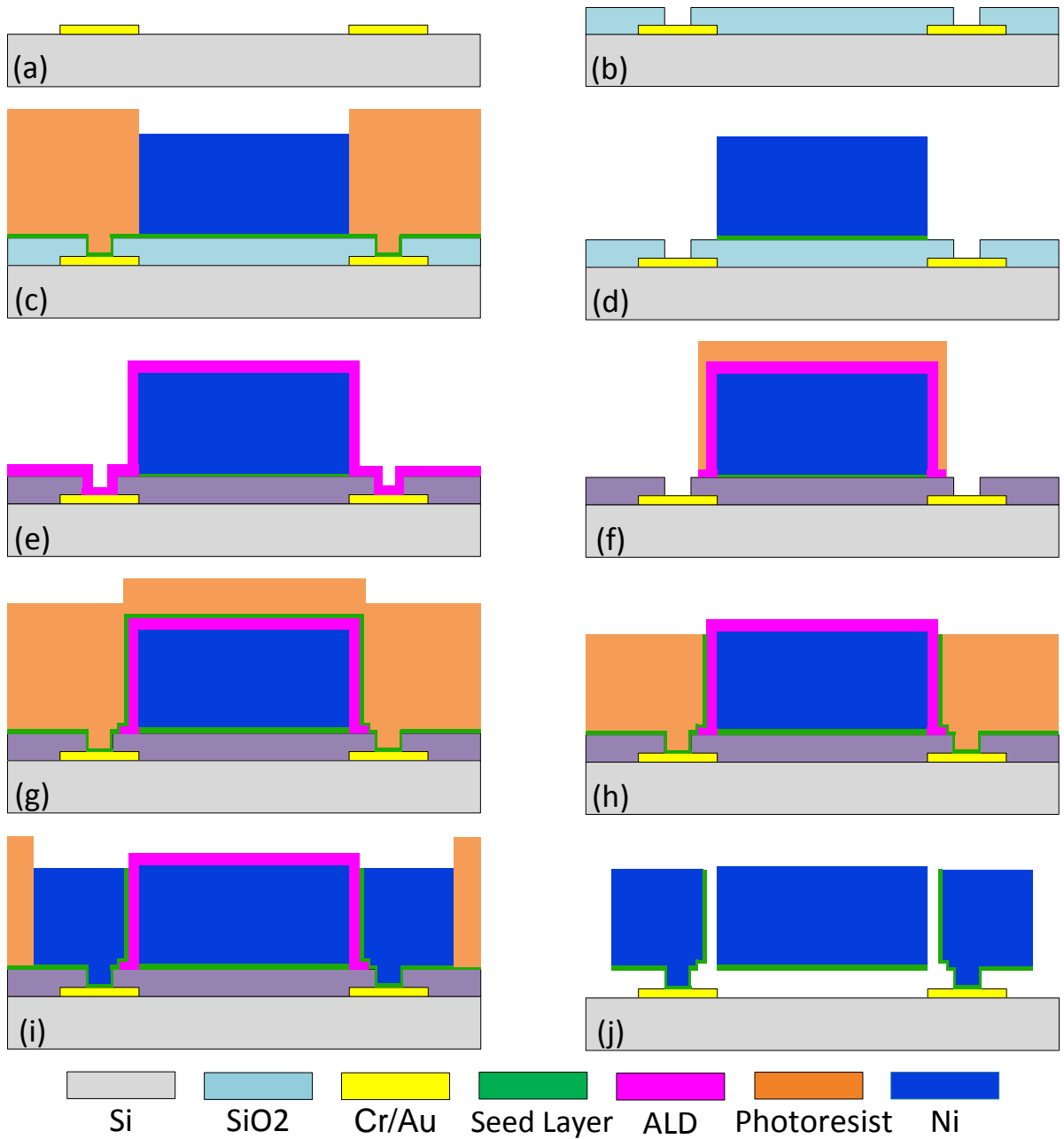
Figure 3.6 Fabrication process flow of an air-gap capacitively-transduced nickel resonator.

Followed by a blanket deposition of Cr/Au (20nm/20nm) seeding layers, AZ P4620 photoresist mold was then patterned using the third photomask. A 5µm-thick nickel

microstructure was electroplated inside the mold to form the body of the disk resonator. After soaking in the solvent and metal etchant to remove the mold and seeding layers, respectively, a 100nm-thick Al_2O_3 film was deposited by ALD to uniformly cover the sidewall of the resonators while defining the electrode-to-resonator capacitive gap as shown in Figure 3.6 (e). Followed by UV photolithography of the fourth photomask, the sidewall dielectric film was protected by photoresist from dry etching for the purpose of removing the field Al_2O_3 film and making contact to the bottom electrodes. Next, molding process along with electroplating was employed again to form the surrounding electrodes for the MEMS resonators. Finally, a wet etching process using 6:1 BOE (buffered oxide etchant) was adopted to selectively etch away the silicon dioxide sacrificial layer and Al_2O_3 transducer gap resulting in suspended resonator structures in electroplated nickel and released air gap. The final device cross-sectional structure is illustrated in Figure 3.6 (j).
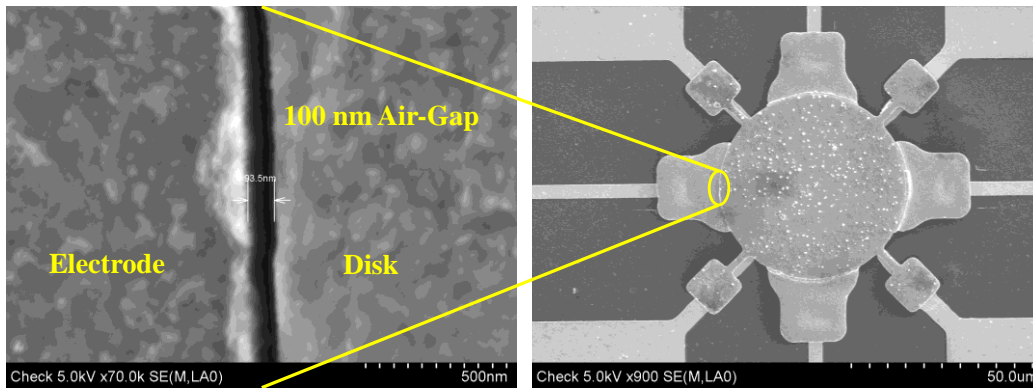
Figure 3.7 SEM image of electroplated-Ni wine-glass mode disk resonator with an air gap of 100nm.

After soaking the nickel resonator in the buffered oxide etchant for about 1 hour, the device was released to be suspended and the Al_2O_3 was etched away to form the 100 nm electrode-to-disk air gap as shown in Figure 3.7. Also, the Cr/Au bottom electrodes were exposed for on-chip probing for in air measurement or wire-bonding for in vacuum measurement.

3.4 Partially-Filled Air-Gap Resonator Fabrication Process
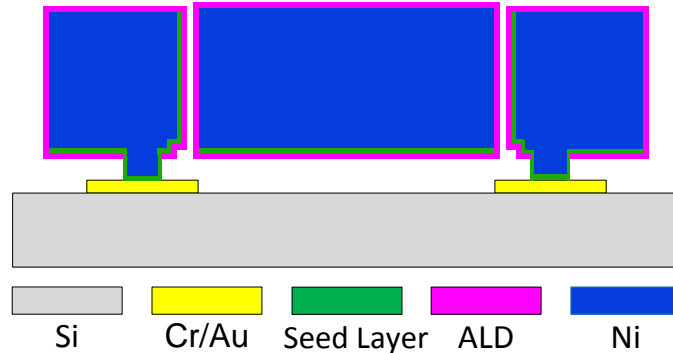
Figure 3.8 Cross-sectional illustration of a partially-filled air-gap capacitively-transduced nickel resonator.

First, following the fabrication process for an air-gap nickel resonator, a 100nm-thick capacitive transducer gap was defined by ALD and an air-gap device was realized after a BOE wet etching. Then, a 15nm-thick HfO_2 was deposited by ALD so that both sides of the released capacitive air gap were coated with a conformal ALD film. Therefore, the 100nm-thick air gap was refilled to effectively reducing the air gap down to 70 nm for an already released structure.
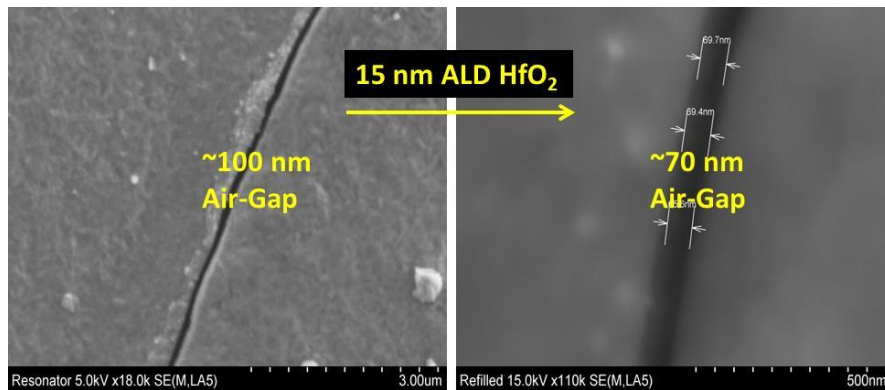
Figure 3.9 SEM images of electroplated-Ni disk resonator with air gap of 100nm and partially-filled air gap of 70nm after 15nm ALD deposition.

CHAPTER 4 PIEZOELECTRIC-ON-NICKEL MEMS RESONATORS

To date, piezoelectrically-actuated resonators have been successfully developed and commercially utilized for frequency control and sensing applications including MEMS oscillators from SiTime, IDT and Discera, Quartz-MEMS inertial measurement unit from Epson, BAW and SAW filters from Avago, Triquint and so on. Better performance devices are still being pursued by applying new material, fabrication technology and integration methods.

4.1 Piezoelectric Effect and Piezoelectric Materials

The piezoelectric effect was first discovered by Pierre Curie and Jacques Curie in 1880 and later applied in transducers by Paul Langevin in 1916. As shown in Figure 4.1, for the direct piezoelectric effect, an electrical charge is generated by applying mechanical stress on piezoelectric materials. On the other hand, the converse piezoelectric effect appears when the mechanical deformation is generated by an electric field. Overall, the piezoelectric effect is a linear interaction between the mechanical and electrical domains in a reversible process [48]. The piezoelectric governing equations which show the relation between the electrical and mechanical domains can be expressed by [49]

$$T = c^E \cdot S - e \cdot E \tag{4.1}$$

$$D = e \cdot S + \varepsilon^S \cdot E \tag{4.2}$$

where T, S, D and E represent stress, strain, electric displacement and electric field, respectively; c^E is the elastic stiffness at a constant electric field; e is the piezoelectric constant; ε^S is the permittivity at a constant strain.
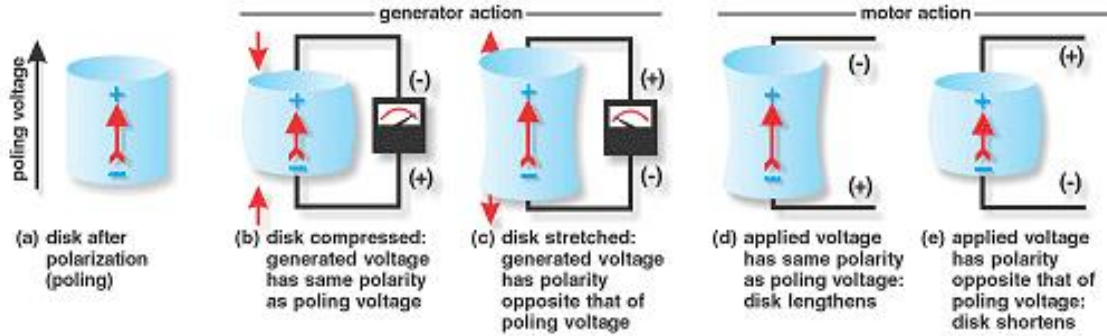
Figure 4.1 Illustration of the direct and reverse piezoelectric effects [48].

Among all the materials that have piezoelectric effect, quartz and rochelle salt are naturally occurring crystals; barium titanate ($BaTiO_3$), lead zirconate titanate (PZT), zinc oxide (ZnO) and aluminum nitride (AlN) are synthetic ceramics. So far, PZT, ZnO and AlN are the commonly used piezoelectric materials for MEMS applications due to their relatively low deposition temperature (below 300°C) which supports IC-compatible process for MEMS-IC integration.

4.2 Piezoelectrically-actuated MEMS Resonator

(a)   (b)
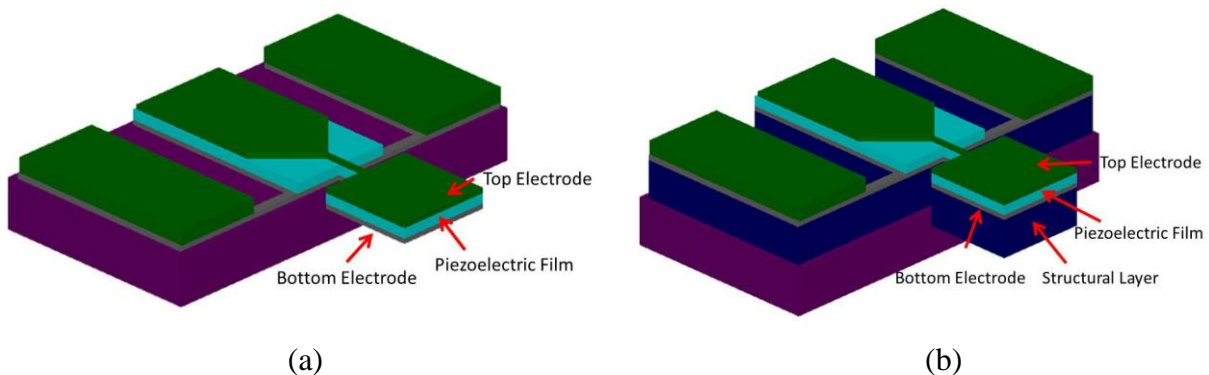
Figure 4.2 Schematic view of (a) a thin-film piezoelectric rectangular plate resonator; (b) a piezoelectric-on-substrate rectangular plate resonator.

The conventional piezoelectric resonators usually has the suspended sandwich structure as shown in Figure 4.2 (a) including a top electrode, a thin piezoelectric film and a bottom electrode. This kind of devices can achieve high operation frequency by decreasing the

piezoelectric film thickness in the thickness modes and scaling down the device lateral dimensions in the extensional modes. However, the sputtered piezoelectric films have limited thickness of a few microns or less due to the low deposition rate. Moreover, the yield of piezoelectric resonators is restricted by the releasing process since the stress of the thin films usually causes the structural layer to curve or fracture. Thus, the development of piezoelectric-on-substrate resonators as shown in Figure 4.2 (b) is an alternative solution to solve the aforementioned drawbacks. The prior work has been done by using single crystal silicon or nano-crystalline diamond (NCD) as resonant structural material due to their high acoustic velocity and low material-related loss [18]. However, the deposition temperature for silicon and diamond structural layer hinders the monolithic integration with IC chips as discussed in Chapter 2. Therefore, electroplated nickel is also a reasonable structural material candidate for piezoelectric-on-substrate resonators to retain high resonance frequencies and moderate Q's. In the meanwhile, zinc oxide (ZnO) has been selected here as the piezoelectric film due to its low deposition temperature around 300°C and its compatibility with a dry etching.

Table 4.1 Key Properties of Materials for Piezoelectric-on-Substrate Resonators

Material	Young's Modulus E(GPa)	Density ρ (kg/m³)	Acoustic Velocity (m/s)	Deposition Temperature (°C)	Electrical Conductivity (10^7 Ωm)
ZnO (This work)	123	5676	4655	300	$3 \cdot 10^{-7}$
PolySilicon [13]	150	2330	8023	600	0.001
PolyDiamond [13]	1,144	3500	18,076	800-1000	0.001
Nickel (This work)	257±11	8900	5048±43	40-60	1.43

$$f_o = \frac{k}{2\pi R}\sqrt{\frac{E}{\rho(1-\nu^2)}}$$

E: Young's Modulus
ρ: Material Density
ν: Poisson's Ratio
R: Disk Radius
k: Frequency Parameter

| (a) | (a') | (a'') |

$$f_o = \frac{\alpha}{R}\sqrt{\frac{E}{\rho(1-\nu^2)}}$$

E: Young's Modulus
ρ: Material Density
ν: Poisson's Ratio
R: Disk Radius
α: Mode-dependent Scaling Factor

| (b) | (b') | (b'') |

$$f_n = \frac{n}{2W}\sqrt{\frac{E}{\rho}}$$

E: Young's Modulus
ρ: Material Density
ν: Poisson's Ratio
W: Width
n: Mode-dependent Scaling Factor

| (c) | (c') | (c'') |
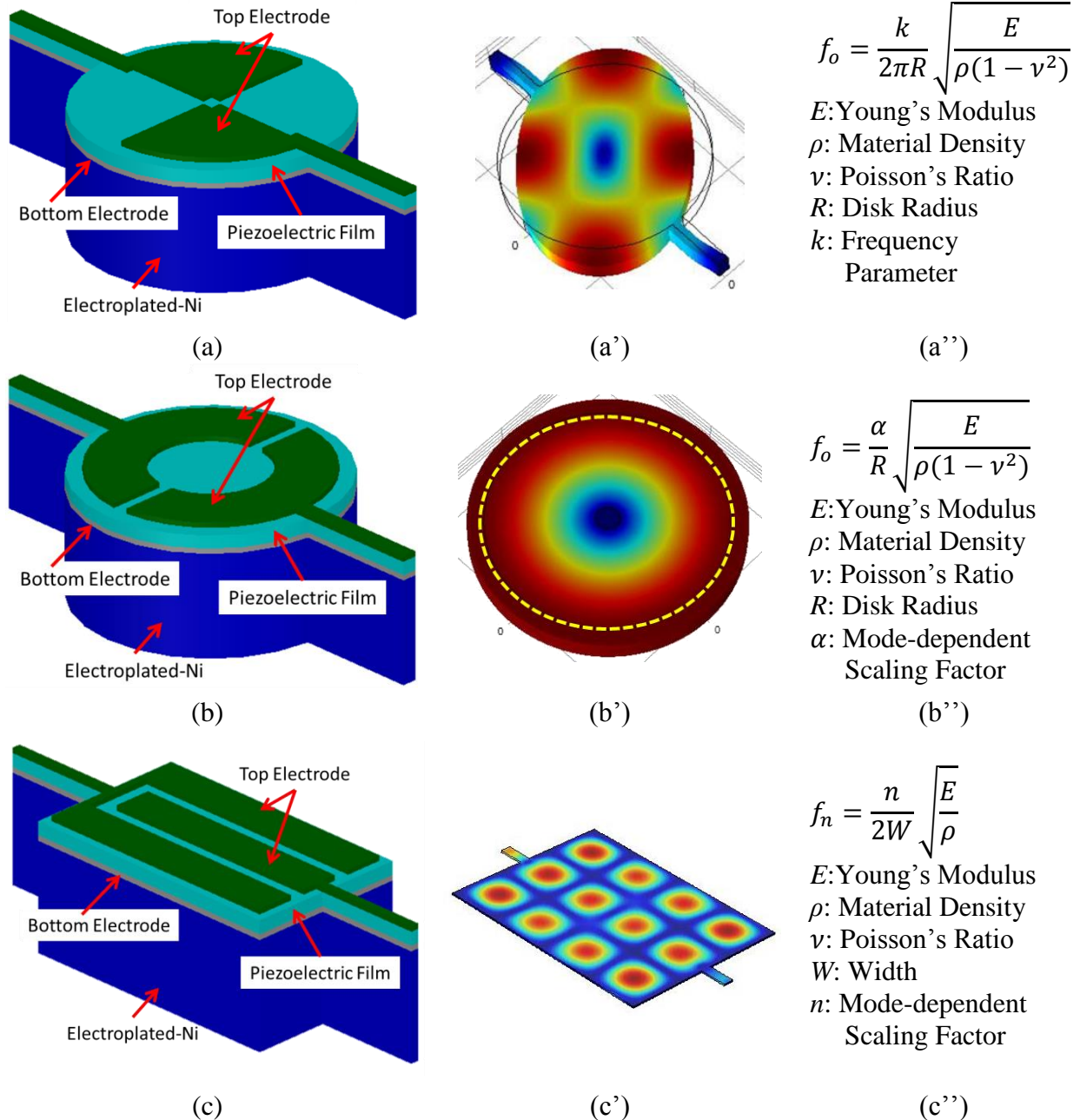
Figure 4.3 Schematics and simulated mode shapes for (a) wine-glass mode piezoelectric-on-nickel resonator; (b) contour-mode piezoelectric-on-nickel resonator; (c) lateral-extensional mode piezoelectric-on-nickel resonator.

Among a great deal of vibration resonant modes, the radial-contour mode, wine-glass mode and lateral-extensional mode have been jointly investigated in this work. The schematic view, simulated mode shape and frequency equation can be found in Figure 4.3. Different shapes of top electrodes are strategically designed to excite the desired resonant mode while suppressing

the other spurious modes at the same time. More details will be discussed along with the measurement results.
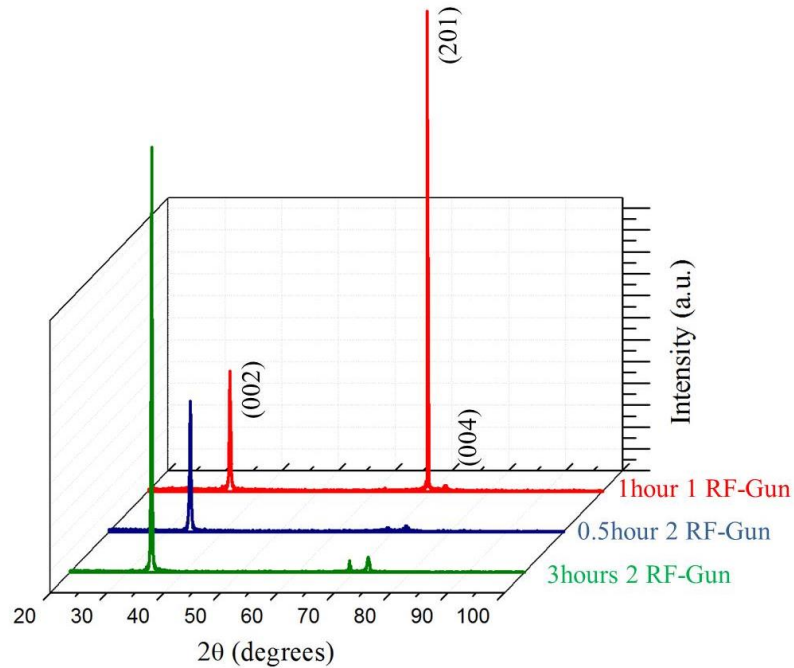
Figure 4.4 XRD measurement of as-deposited ZnO thin films under different conditions.

The ZnO deposition rate is about 120 nm per hour under normal conditions of 300°C substrate temperature, 6ccm Ar and 6ccm O_2, 100W RF power. However, instead of using a single target for one source RF sputtering, deposition by using two ZnO targets powered by two different RF sources was conducted in order to double the deposition rate to about 240 nm per hour and improve the quality of c-axis aligned piezoelectric film. The comparison of as-deposited ZnO thin films under different conditions was evaluated by x-ray diffraction (XRD). Figure 4.4 shows consistent results of two RF-gun deposited ZnO thin films which have a strong alignment to (002) plane while the one RF-gun deposited ZnO film has a crystal defect along (201) plane, which will result in extra mass loading and energy loss on the resonator.
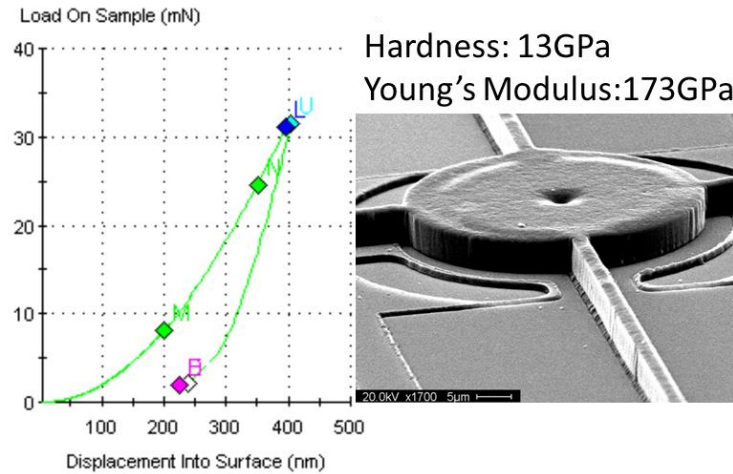
Figure 4.5 Nanoindentation of electroplated nickel revealing its Young's modulus and hardness.

Nickel resonator microstructure was electroplated at 50°C in the nickel sulfamate solution. The mean current density here plays a significant role for determining the Young's modulus [50]. The nanoindentation measurement was then carried out to determine the Young's modulus of about 173 GPa and the hardness of 13 GPa for electroplated nickel under the current density of 20 mA/cm^2.

Table 4.2 Comparison of Electroplated Nickel Young's Modulus with Different Mean Current Density

Measured Young's Modulus (GPa)	Mean Current Density (mA/cm^2)				
	2	2.5	5	10	20
Microindentation [50]	223±19	–	208±11	180±7	178±21
Cantilever [50]	–	205	–	–	163
Nanoindentation (This Work)	–	–	–	–	173
ZnO-on-Nickel Resonator (This Work)	–	257±11	–	–	–

For the sake of calculating the resonant frequency of ZnO-on-nickel resonators, the equivalent acoustic velocity has to be determined for the stacked device layers. Based on the Hooke's Law, the equivalent acoustic velocity can be expressed by [51]

$$V_{eq} = \sqrt{\frac{E_1 T_1 + E_2 T_2 + \cdots + E_n T_n}{(\rho_1 T_1 + \rho_2 T_2 + \cdots + \rho_n T_n)(1 - \nu^2)}} \qquad (4.3)$$

where n is the number of the stacked layers; T is the thickness of each material; E, ρ, and ν denote the Young's Modulus, density and Poisson's ratio of the stacked resonator structural material. The equivalent Poisson's ratio of the stacked layer structure is assumed to be 0.3.

Table 4.3 Measurement Results of ZnO-on-Nickel Resonators with 700nm-thick ZnO Piezoelectric Layers

Diameter (µm)	Thickness of Ni (µm)	Frequency (MHz)	Quality Factor
275	2	29.1	546.5
	4	30.3	236.6
225	2	35.5	379.4
	4	36.9	199.4
175	2	45.3	395.5
	4	46.8	159.3
125	2	63.2	361.4
	4	65.3	193.5
75	2	72.0	202.3
	4	73.9	147.0
50	2	109.1	122.9
	4	111.4	109.5

Based on this method, the extracted acoustic velocity of electroplated nickel is determined to be slightly higher than that of ZnO. Thus, the equivalent acoustic velocity of ZnO-on-nickel resonators is also slightly higher than ZnO resonators, which varies with different combinations of this ZnO-on-nickel layer stack. Table 4.3 presents ZnO-on-nickel resonators with the same 700nm-thick of ZnO piezoelectric layer but different thickness of electroplated nickel. The frequency of these devices increased when having a thicker nickel layer due to its higher equivalent acoustic velocity. However, the material loss of as-deposited nickel limited the Q of the devices with a thicker nickel structural layer as well.

4.3 Fabrication Process

Figure 4.6 presents a step-by-step fabrication process flow for a piezoelectrically-actuated resonator using ZnO-on-nickel as its stacked structural material. Starting with a high resistivity (6kΩ·cm) silicon wafer coated by a 5 μm PECVD SiO_2 isolation layer, 1μm-thick amorphous silicon was then deposited by PECVD as a sacrificial layer. After a blanket deposition of Cr/Ni seeding layer, AZ P4620 photoresist mold was then patterned using the first photomask, where 4μm-thick nickel microstructure was electroplated inside the mold. Right after it, 200nm-thick platinum was then ebeam evaporated on top of the electroplated nickel and the photoresist mold. After a lift-off process, the platinum on nickel structure was then formed to act as the bottom electrode of the resonator. Thereafter, ZnO film was deposited by RF sputter at 300°C with a deposition rate of 240nm/hr. By utilizing the second photomask and UV photolithography, the photoresist patterns were then transferred to ZnO by HCl: H_2O (1: 100) wet etching, forming the contact openings to the bottom electrodes. The platinum top electrode was created by utilizing the third photomask and lift-off process. Finally, after patterning the photoresist by the fourth photomask to generate an opening for the release process and protect

the rest of the sample, the resonator structure was suspended by dry etching of ZnO and isotropic

dry etching of amorphous silicon sacrificial layer via DRIE.
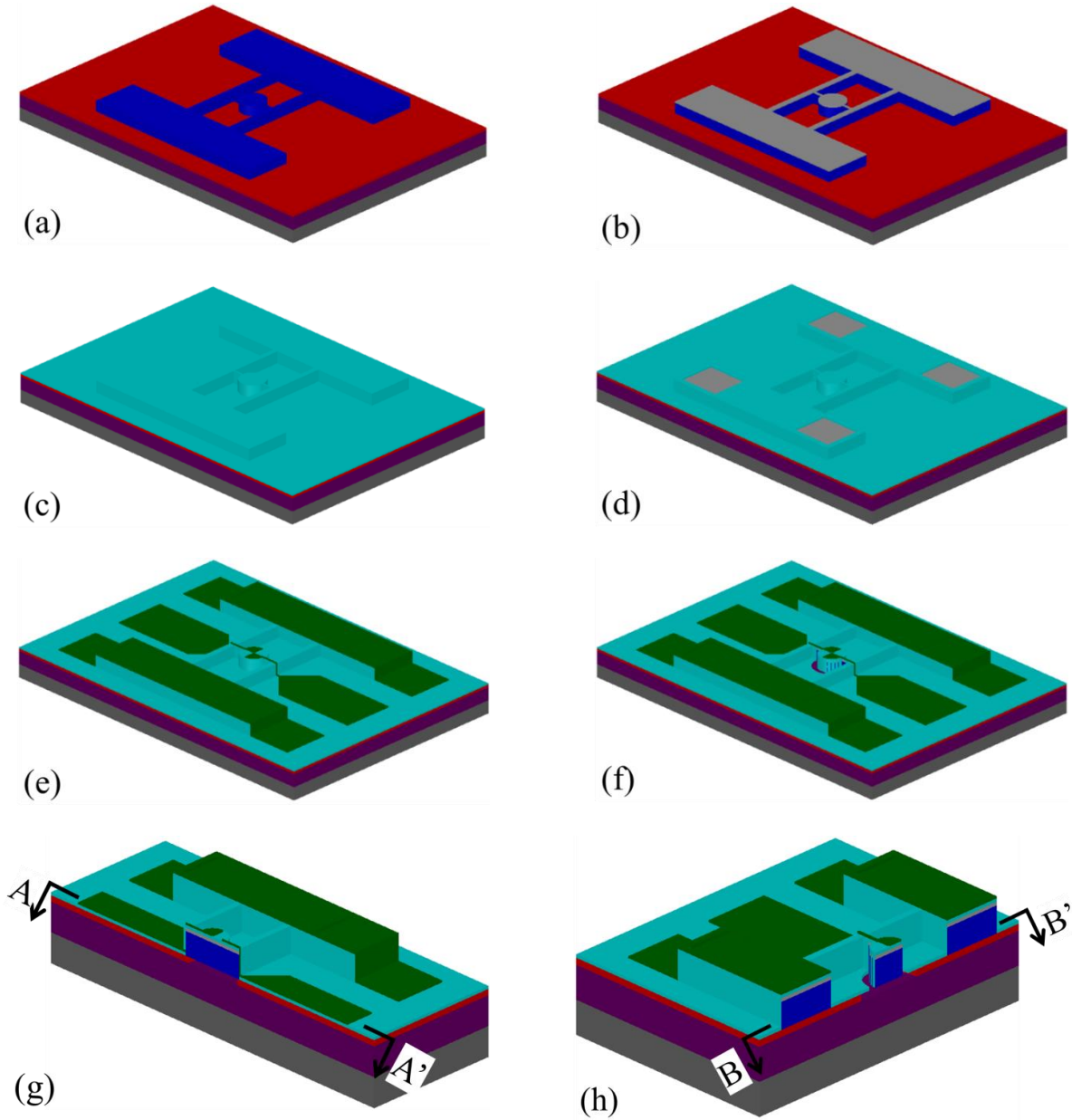
Figure 4.6 (a) ~ (f) Fabrication process flow of ZnO-on-nickel resonator and (g) A-A' and (h) B-B' cross-sectional schematic view of the final released resonator structure.

An alternative release process of backside release was also carried out by utilizing the

fifth photomask and aligning the backside of the silicon handle wafer followed by the DRIE

silicon etching. Figure 4.7 presents a fabricated wine-glass mode ZnO-on-nickel resonator with a ZnO thickness of 700 nm and a 4µm-thick electroplated nickel.
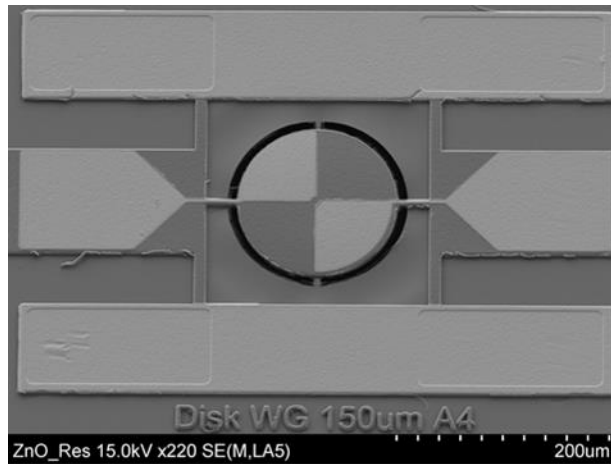
Figure 4.7 SEM image of a fabricated wine-glass mode ZnO-on-nickel resonator.

4.4 Localized Annealing

| (a) | (b) |
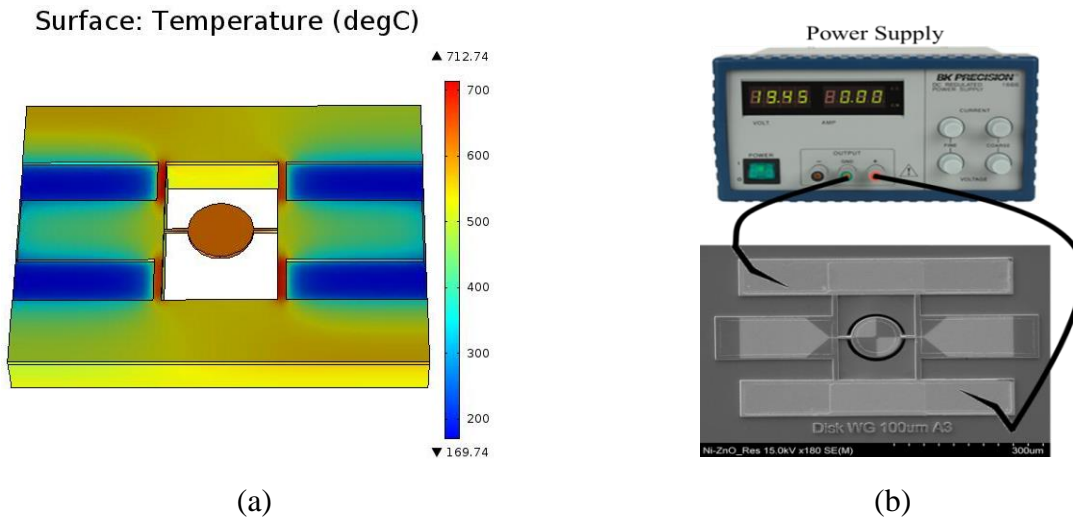
Figure 4.8 Illustration of the localized annealing by (a) Comsol simulation and (b) measurement set-up.

Besides the low deposition temperature and the ease of process, the employment of electroplated nickel as structural material has lower resistivity as compared to doped polysilicon which has a concern of additional resistive loss [52]. However, electroplated nickel applied in

MEMS devices has shown relatively low Q's [53]. Thus, a post-fabrication annealing procedure has been discovered [54] in order to improve the performance of nickel micromechanical resonators.

In situ localized annealing can be performed by applying an electrical current on the conductive micromechanical resonator structure to heat it up, which has been demonstrated to improve the Q's of a 75-kHz folded-beam resonator from 4,103 to 14,172 by applying 1.5v for 4 hours and reaching an elevated temperature of 886°C [54]. Comsol simulation has been conducted to simulate the relation between the applied voltage (1.5v) and the temperature of ZnO-on-nickel resonators as shown in Figure 4.8 (a). The suspended ZnO-on-nickel resonator body can be annealed to about 600°C to 700°C while the high resistivity silicon substrate retains a temperature of 200°C.
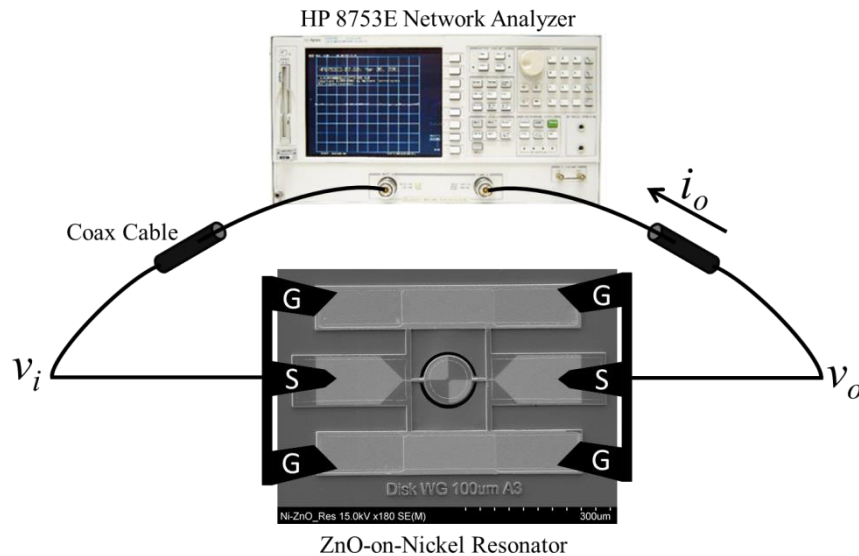
Figure 4.9 Schematic measurement set-up for ZnO-on-Nickel resonators.

4.5 Measurement Results

In order to measure the frequency response of piezoelectric resonators, an AC electric field is required which is provided by a vector network analyzer (VNA) as shown in Figure 4.9.

The AC signal applied on the input electrodes excite the piezoelectric film which drives the resonator structure to vibrate at its resonant frequency. The deformation by the vibrating resonator body will then induce the piezoelectrically-generated charges which are detected by the output electrodes. Compared to the capacitively-transduced resonators, piezoelectrically-actuated resonators require no DC-bias voltage by relying on the piezoelectric effect.

The measurement results from VNA reflect both the resonant frequency and quality factor of the device. However, the measured Q here is the loaded Q (Q_L) which includes the external circuit influences from both the parasitic resistance (R_L) in series together with the resonator motional resistance (R_m). The unloaded Q (Q_{UL}) reflects the intrinsic energy storage versus energy dissipation in the resonator system. The relationship among Q_L, Q_{UL} and insertion loss (IL) can be expressed by [55]

$$\frac{Q_{UL}}{Q_L} = \frac{10^{\frac{IL}{20}}}{10^{\frac{IL}{20}} - 1} \tag{4.4}$$

Thereafter, the motional resistance could be extrapolated by taking 50 Ω termination of VNA (a total of 100 Ω for two-port measurement) and expressed by [56]

$$Q_L = Q_{UL} \frac{R_m}{R_m + R_L} \tag{4.5}$$

4.5.1 Circular Disk ZnO-on-Nickel Resonators

Figure 4.10 shows the measured frequency response of a circular disk ZnO-on-nickel resonator operating in its wine-glass mode at 29.1 MHz which measured Q of 564.5. The frequency response reflects the design of the top input and output electrodes which align with the vibration mode shape shown in Figure 4.3 (a'). Also, the supporting beams are located at the quasi-nodal points to minimize the anchor loss.
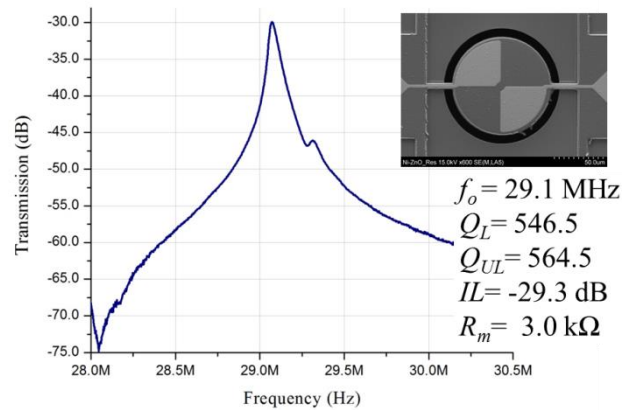
Figure 4.10 Frequency response of a 275µm-diameter wine-glass mode ZnO-on-nickel resonator.
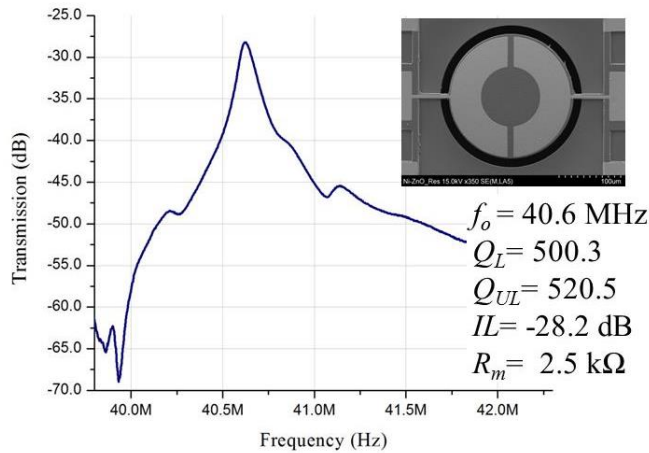
Figure 4.11 Frequency response of a 225µm-diameter radial-contour mode ZnO-on-nickel resonator.

Figure 4.11 presents the measured frequency response of a ZnO-on-nickel resonator operating in its radial-contour mode at 40.6 MHz and a Q of 520.5. The frequency response reflects the strategic design of the top input and output electrodes with the shape of two half circular rings which align with the vibration mode shape as shown in Figure 4.3 (b'). However, the supporting beams which are holding the vibrating structure are not directly located at the quasi-nodal point, which introduce anchor loss to the device leading a slightly lower Q as compared to wine-glass mode resonators.
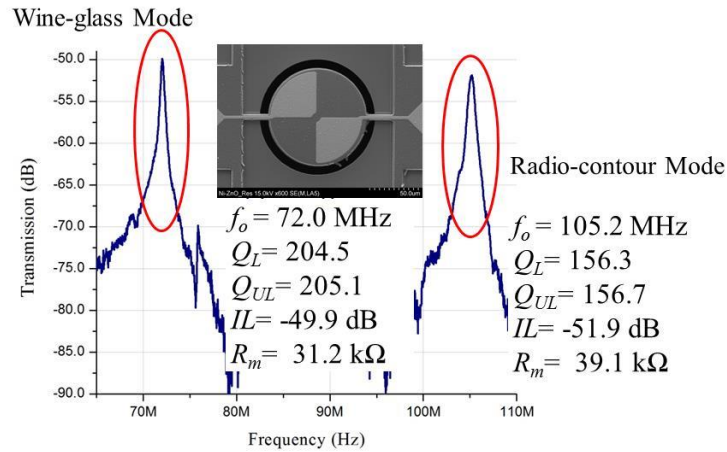
Figure 4.12 Frequency response of a 75µm-diameter ZnO-on-nickel resonator with quarter-circle top electrodes.
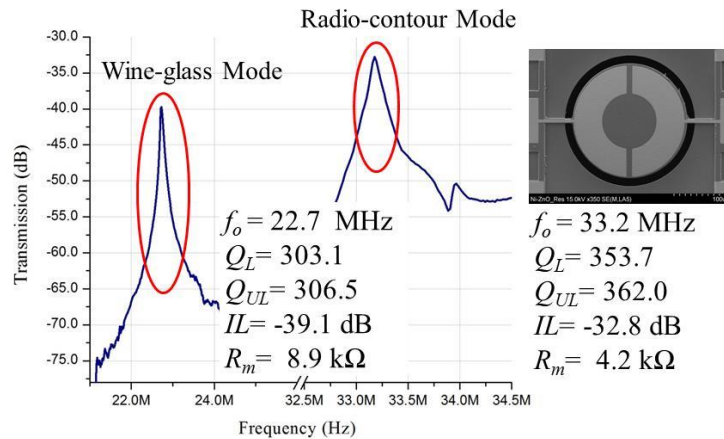
Figure 4.13 Frequency response of a 250µm-diameter ZnO-on-nickel resonator with half-circle ring top electrodes.

Figure 4.12 shows the measured frequency response of a circular disk ZnO-on-nickel resonator operating in its wine-glass mode at 72.0 MHz and radial-contour mode at 105.2 MHz. Both wine-glass mode and radial-contour mode can be actuated in a circular disk resonator. The top electrodes of this device were designed to match with the wine-glass mode shape. Therefore, the signal of the desired mode is much stronger than that of the radial-contour mode.

70

Figure 4.13 presents the measured frequency response of a circular disk ZnO-on-nickel resonator showing both wine-glass mode at 22.7 MHz and radial-contour mode at 33.2 MHz. Similarly, although both modes can be observed in this circular device, the top electrodes were designed to match with the radial-contour mode shape. Therefore, the signal of the desired radial-contour mode is much stronger than that of the wine-glass mode.

4.5.2 Square and Rectangular Plate ZnO-on-Nickel Resonators

(a)   (b)
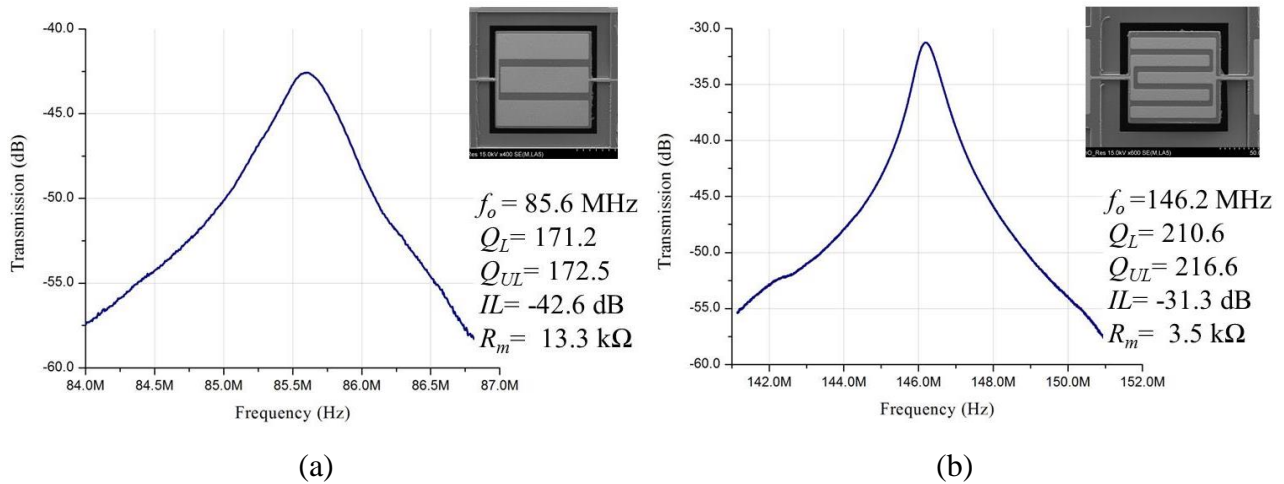
Figure 4.14 Frequency response of two 82μm-width square plate ZnO-on-nickel resonators with (a) n=3 and (b) n=5.

Figure 4.14 shows the frequency responses of two identically sized ZnO-on-nickel resonators with different top electrodes designs. As shown in Figure 4.14 (a), the resonator vibrates at 85.6 MHz which matches the modal frequency of n=3 as seen in Figure 4.3 (c). And the resonator in Figure 4.14 (b) vibrates at 146.2 MHz which matches the lateral-extensional frequency mode of n=5 and gives a higher Q because the deigned width of the top electrodes match the mode shape better than the one of n=3. In addition, for higher order mode device, the impedance is also reduced by a factor of N, where $N = n$ for the even n; and $N = (n^2 - 1)$ for the odd n [18].
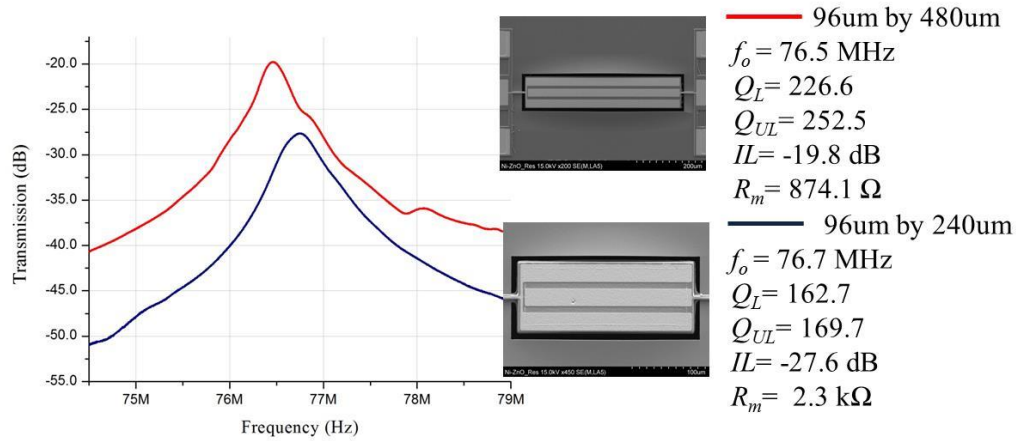
Figure 4.15 Frequency responses of two rectangular plate ZnO-on-nickel resonators with the same width of 96 μm but different length of 480 μm and 240 μm, respectively.
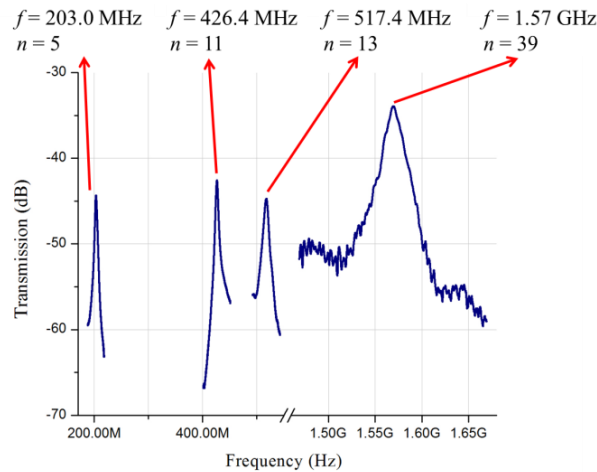
Figure 4.16 Frequency response of a 60μm-width square plate ZnO-on-nickel resonator in fundamental mode and high order frequency modes.

Figure 4.15 presents the measured frequency responses of two rectangular plate ZnO-on-nickel resonators designed to have the same width but different length. Both of the devices were actuated in width extensional mode, therefore, the vibration frequencies are roughly the same which are determined by the size of width only. Since one of the devices has twice of the length, the overall area of ZnO film on top of the nickel is much larger which results in higher

72

electromechanical coupling coefficient. Thus, the motional resistance has decreased by increasing the effective piezoelectric transducer area.

f_o = 77.1 MHz
Q_L= 116.3
Q_{UL}= 120.6
IL= -28.8 dB
R_m= 2.6 kΩ

(a)

f_o = 77.0 MHz
Q_L= 100.9
Q_{UL}= 107.9
IL= -23.7 dB
R_m= 1.4 kΩ

(b)

f_o = 77.1 MHz
Q_L= 171.5
Q_{UL}= 186.6
IL= -21.85 dB
R_m= 1.1 kΩ

(c)

f_o = 77.1 MHz
Q_L= 158.1
Q_{UL}= 183.5
IL= -17.2 dB
R_m= 623 Ω

(d)
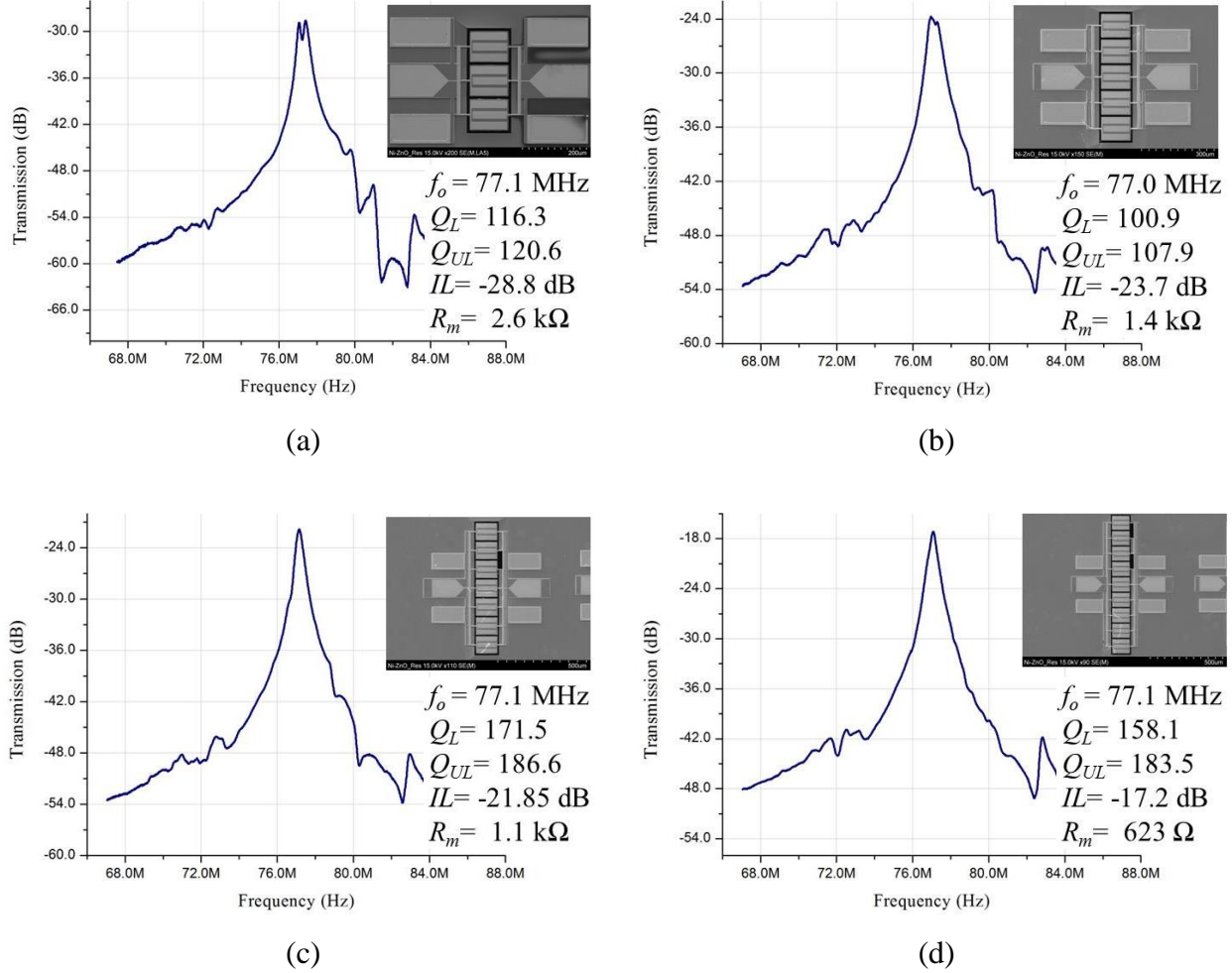
Figure 4.17 Frequency responses of ZnO-on-nickel resonator arrays: (a) 1×3 array; (b) 1×5 array; (c) 1×7 array; and (d) 1×9 array.

Besides the fundamental frequency mode, higher frequency modes can also be observed in a single ZnO-on-nickel resonator as shown in Figure 4.16. With the width size of 60 μm and five top electrodes fingers, this square resonator was actuated at 203.0 MHz in the fundamental width-extensional mode. Meanwhile, higher mode of n=11, 13 and 39 also appeared at resonance frequency of 426.4 MHz, 517.4 MHz and 1.57 GHz, respectively. It is observed that the design

of this ZnO-on-nickel resonator can achieve frequencies ranging from very high frequency to ultra high frequency.

4.5.3 Resonator Arrays

In order to achieve higher operation frequency, the size of MEMS resonator has been reduced significantly. As a trade-off of the reduced-size resonator, the electromechanical coupling coefficient is reduced as well resulting in a higher motional resistance. Mechanically coupling several identical resonators into an array provides promising solution to lower the motional resistance while perfectly matching the frequency as compared to the electrically coupled method [57]. In an idea case, by sharing the same input voltage, the output current will be boosted by a factor that is equal to the number (N) of resonators in an array. As a result, the motional resistance could be reduced by N times while each resonator vibrates at the same frequency individually.

The frequency responses of different resonator arrays as shown in Figure 4.17 indicate a significant reduction of motional resistance from 2.6 kΩ to 623 Ω when expanding the coupled resonators in parallel from three to nine with a consistent resonant frequency of about 77.1 MHz.

4.5.4 In Air vs. In Vacuum Operation

At this point, in order to improve the quality factor of resonators, it's worth to mention all the energy dissipation mechanisms have to be taken into account including the radiation of elastic energy by the supporting structures to the substrate (e.g. anchor losses), air damping, squeeze film damping, surface related dissipation due to surface defects, and thermoelastic damping. Therefore, the overall Q of a resonator can be expressed by [58]

$$\frac{1}{Q_{total}} = \frac{1}{Q_{anchor}} + \frac{1}{Q_{air}} + \frac{1}{Q_{surface}} + \frac{1}{Q_{thermoelastic}} \tag{4.6}$$

After wire bonding, the devices can also be tested inside a vacuum chamber. The frequency responses of ZnO-on-nickel resonator are shown in Figure 4.18, which compare the results measured in air and in vacuum. Figure 4.18 (a) presents the responses in flexural mode which is an out-of-plane mode at a lower frequency. After measuring in vacuum, the Q has been improved almost twice as a result of the reduced air damping in vacuum.

(a)   (b)
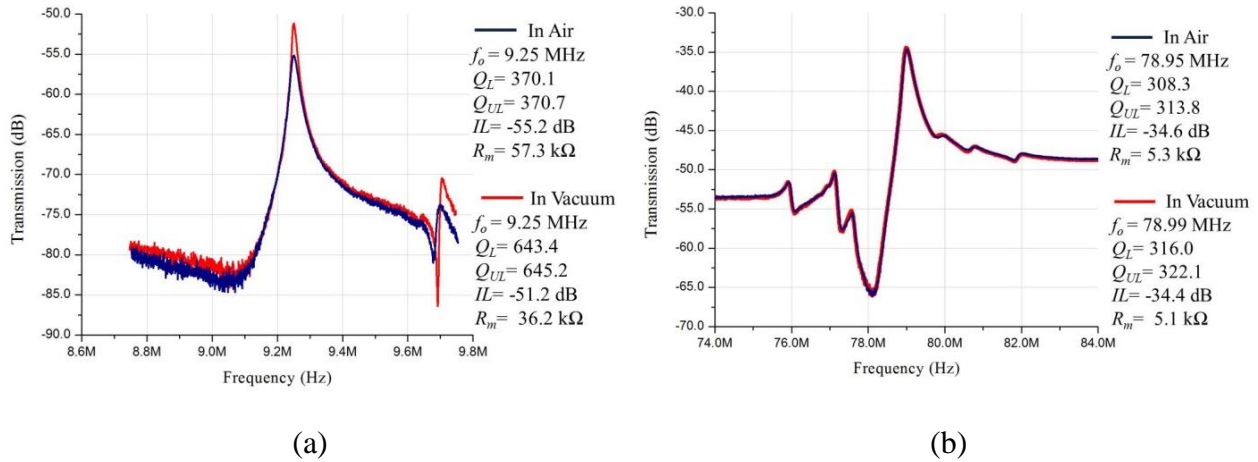
Figure 4.18 Frequency responses of ZnO-on-Nickel resonator measured in air and in vacuum.

The resonator vibrates in width extensional mode as shown in Figure 4.18 (b), also known as in-plane mode. Measured Q in vacuum has not been enhanced as compared to the in air measurement, which indicates that most of the energy dissipation may come from the material loss, anchor loss or thermoelastic loss instead of air damping in this range of frequency and mode shape.

4.5.5 Annealing

Figure 4.19 compares the frequency responses of a ZnO-on-nickel resonator measured before and after localized annealing. After applying a DC voltage of 1.5 v, the resonator was annealed in air for half an hour. As shown, the frequency has drifted by 0.3 MHz and the Q has

been increased by about 3 times from 87.5 to 246.6 as a result of the enhanced material properties after annealing or surface defect removal [54].
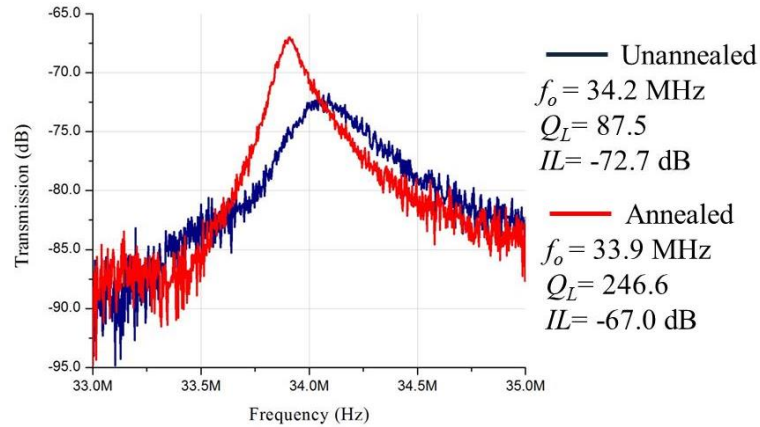
Figure 4.19 Frequency responses of ZnO-on-nickel resonator measured before and after localized annealing.

4.5.6 Temperature Stability
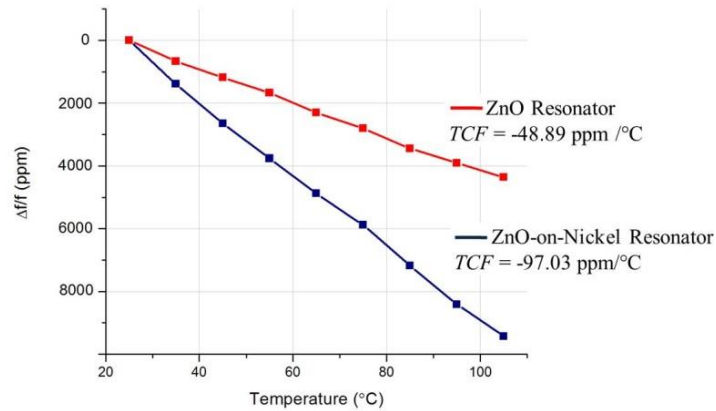
Figure 4.20 Measured fractional frequency change versus temperature for the same size ZnO resonator and ZnO-on-nickel resonator.

Figure 4.20 presents the measurement of fractional frequency change versus temperature for ZnO resonator and ZnO-on-nickel resonator with the same size. The extracted temperature coefficients of the two devices are -48.89 ppm/°C and -97.03 ppm°/C, respectively. Although the

uncompensated temperature coefficient of ZnO-on-nickel resonator is higher than that of ZnO resonator, the frequency versus temperature dependence is very linear which can be readily compensated as compared to the quartz crystal resonators which have nonlinear temperature dependency.

CHAPTER 5 CONCLUSION

According to Yole, a market research, technology evaluation and strategy consulting company, "MEMS will continue to see steady, sustainable double digit growth for the next six years including 13 per cent CAGR in revenues and 20 per cent CAGR in units. MEMS will grow to $21 billion market by 2017." New innovative MEMS technologies have been developed and deployed in the devices for sensing, computing, communications and so on.

The growing needs in wireless communications have driven RF MEMS technologies to meet the requirements such as low power consumption, high power handling, high selectivity and sensitivity. IC-compatible vibrating micromechanical resonator devices have been demonstrated as on-chip passives having great potential on various applications in wireless communications.

5.1 Achievements

Piezoelectrically-actuated vibrating micromechanical resonators with ZnO-on-nickel structures were demonstrated to have proper performance that is suitable for applications such as filter, oscillator, and mixer in wireless communications. First, the resonant frequency of the ZnO-on-nickel resonators and resonator arrays were determined by the lateral dimensions of the vibrating structure and actuated by piezoelectric ZnO film. Hence, multiple frequencies can be achieved on the same sample. Secondly, the fabricated ZnO-on-nickel resonators and resonator arrays have been measured to operate at HF, VHF and UHF ranges with low motional impedance and moderate quality factor. Thirdly, the very high yield and repeatable device fabrication process was demonstrated under 300°C which is totally compatible with post fabrication over the

IC electronics for further IC-MEMS integration. Last but not the least, electroplated nickel as MEMS structural material brings the benefit of both low deposition temperature and low cost which is easier to be realized in the industry.

Capacitively-transduced vibrating micromechanical resonators with electroplated nickel as structural material and different transducer gaps including air gap, solid gap and partially-filled air gap were developed for the applications such as filter, oscillator and mixer in wireless communications. Air-gap, solid-gap and partially-filled air-gap resonators were fabricated under 250°C process temperature by using the same five-mask set with slightly modified fabrication process and materials. By applying low temperature process of nickel electroplating and ALD deposition, capacitively-transduced MEMS resonators and arrays can be directly fabricated over IC electronics allowing monolithic IC-MEMS integration to reduce the parasitics, lower the cost and improve the efficiency in RF applications. Furthermore, the nonlinearity of air-gap, solid-gap partially-filled air gap resonators were simulated and designed for RF applications.

5.2 Future Works

As a trade-off of acquiring small form factor devices at high frequency, large motional impedance has been induced and become a big challenge for applications in wireless communications. As compared to air-gap resonators, partially-filled air-gap resonators can further reduce the gap spacing, lower the motional resistance close to 50 Ω, and significantly improve the quality factor higher than those of solid-gap capacitive transducers. Thus, nanolaminates by ALD could be a candidate of filling material since the combination of Al_2O_3 and TiO_2 brings the dielectric constant up to 1,000 and also improve the material quality. It is interesting to study the resonator behavior after employing nanolaminates.

In order to effectively decrease the crosstalk through silicon substrate, an on-chip Faraday cage isolation structure has been developed [59]. Faraday cage structure consists of serial high-aspect-ratio Cu-filled vias through silicon wafer to build an enclosure blocking out external static electric fields and shunt the middle of the transmitter-receiver gap to ground through the substrate vias as shown in Figure 5.1.

(a)   (b)
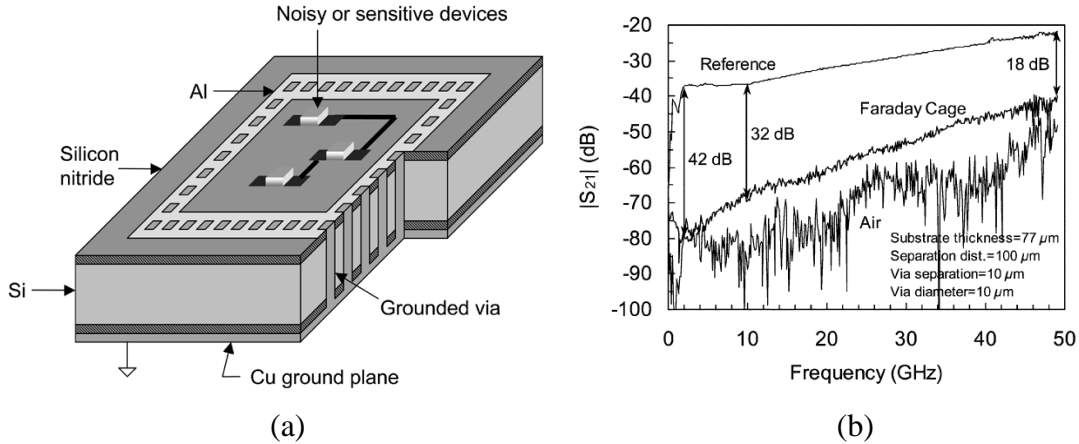
Figure 5.1 (a) Crosstalk isolation scheme by faraday cage; (b) measurement of a faraday cage and reference structure at a transmission distance of 100 um [59].

Table 5.1 Properties of Piezoelectric Material Used In MEMS

Material	Young's Modulus E(GPa)	Density ρ (kg/m³)	Acoustic Velocity (m/s)	Piezoelectric Coefficient (pm/V)	Deposition Temperature (°C)
ZnO	123	5676	4655	4.7	300
AlN [60]	330	3260	10547	2	300
PZT [61]	101	7600	3821	185	350

Among the piezoelectric materials, ZnO is the easiest one to be deposited and patterned during micro fabrication process. However, ZnO does not have the best piezoelectric

80

performance as compared to AlN or PZT which have either higher acoustic velocity or higher piezoelectric coefficient and can be deposited at relatively low temperature as well. By realizing AlN-on-nickel or PZT-on-nickel resonators, both resonant frequency and quality factor could be boosted by taking the advantages of their great piezoelectric properties.

REFERENCES

[1]   J. J. Fahie, *A History of Wireless Telegraphy* 1899.

[2]   R. P. Feynman, "There's Plenty of Room at the Bottom " *Engineering and Science,* 1960.

[3]   C. T. C. Nguyen, "Vibrating RF MEMS for next generation wireless applications," in *Custom Integrated Circuits Conference, 2004. Proceedings of the IEEE 2004*, 2004, pp. 257-264.

[4]   E. H. Armstrong, "A Method of Reducing Disturbances in Radio Signaling by a System of Frequency Modulation," *Radio Engineers, Proceedings of the Institute of,* vol. 24, pp. 689-740, 1936.

[5]   A. A. Abidi, "Direct-conversion radio transceivers for digital communications," *Solid-State Circuits, IEEE Journal of,* vol. 30, pp. 1399-1410, 1995.

[6]   P. Zhang, L. Der, D. Guo, I. Sever, T. Bourdi, C. Lam*, et al.*, "A single-chip dual-band direct-conversion IEEE 802.11a/b/g WLAN transceiver in 0.18-μm CMOS," *Solid-State Circuits, IEEE Journal of,* vol. 40, pp. 1932-1939, 2005.

[7]   A.-C. Wong and C. T. C. Nguyen, "Micromechanical mixer-filters ("mixlers")," *Microelectromechanical Systems, Journal of,* vol. 13, pp. 100-112, 2004.

[8]   N. Lobontiu, *Dynamics of Microelectromechanical Systems* vol. 17, 2007.

[9]   R. R. Mansour, "RF MEMS-CMOS Device Integration: An Overview of the Potential for RF Researchers," *Microwave Magazine, IEEE,* vol. 14, pp. 39-56, 2013.

[10]   M. Lapisa, G. Stemme, and F. Niklaus, "Wafer-Level Heterogeneous Integration for MOEMS, MEMS, and NEMS," *Selected Topics in Quantum Electronics, IEEE Journal of,* vol. 17, pp. 629-644, 2011.

[11]   F. Niklaus, M. Lapisa, S. J. Bleiker, V. Dubois, N. Roxhed, A. C. Fischer*, et al.*, "Wafer-level heterogeneous 3D integration for MEMS and NEMS," in *Low Temperature Bonding for 3D Integration (LTB-3D), 2012 3rd IEEE International Workshop on*, 2012, pp. 247-252.

[12]   A. Witvrouw, "CMOS-MEMS Integration: Why, How and What?," in *Computer-Aided Design, 2006. ICCAD '06. IEEE/ACM International Conference on*, 2006, pp. 826-827.

[13]   H. Wen-Lung, R. Zeying, and C. T. C. Nguyen, "Nickel Vibrating Micromechanical Disk Resonator with Solid Dielectric Capacitive-Transducer Gap," in *International Frequency Control Symposium and Exposition, 2006 IEEE*, 2006, pp. 839-847.

[14]   M. W. Putty and K. Najafi, "A micromachined vibrating ring gyroscope," in *Solid-State Sensor Actuator Workshop*, Hilton Head Island, SC, 1994, pp. 213–220.

[15]   Y. Satoh, T. Nishihara, T. Yokoyama, M. Ueda, and T. Miyashita, "Development of Piezoelectric Thin Film Resonator and Its Impact on Future Wireless Communication Systems," *Japanese Journal of Applied Physics,* vol. 44, pp. 2883-2894, 2005.

[16]   P. S. Cross, "Reflective Arrays for SAW Resonators," in *1975 Ultrasonics Symposium*, 1975, pp. 241-244.

[17]   G. Piazza, P. J. Stephanou, and A. P. Pisano, "Piezoelectric Aluminum Nitride Vibrating Contour-Mode MEMS Resonators," *Journal of Microelectromechanical Systems,* vol. 15, pp. 1406-1418, 2006.

[18]   R. Abdolvand, H. M. Lavasani, G. K. Ho, and F. Ayazi, "Thin-film piezoelectric-on-silicon resonators for high-frequency reference oscillator applications," *Ultrasonics, Ferroelectrics, and Frequency Control, IEEE Transactions on,* vol. 55, pp. 2596-2606, 2008.

[19]   J. Wang, Z. Ren, and C. T. C. Nguyen, "1.156-GHz self-aligned vibrating micromechanical disk resonator," *Ultrasonics, Ferroelectrics and Frequency Control, IEEE Transactions on,* vol. 51, pp. 1607-1628, 2004.

[20]   W.-T. Hsu and C. T. C. Nguyen, "Stiffness-compensated temperature-insensitive micromechanical resonators," in *Micro Electro Mechanical Systems, 2002. The Fifteenth IEEE International Conference on*, 2002, pp. 731-734.

[21]   M. A. Hopcroft, H. K. Lee, B. Kim, R. Melamud, S. Chandorkar, M. Agarwal*, et al.*, "A High-Stability MEMS Frequency Reference," in *Solid-State Sensors, Actuators and Microsystems Conference, 2007. TRANSDUCERS 2007. International*, 2007, pp. 1307-1309.

[22]   C. Kuan-Lin, W. Shasha, J. Salvia, R. T. Howe, and T. W. Kenny, "Encapsulated out-of-plane differential square-plate resonator with integrated actuation electrodes," in *Solid-State Sensors, Actuators and Microsystems Conference, 2009. TRANSDUCERS 2009. International*, 2009, pp. 1421-1424.

[23] L. Sheng-Shian, L. Yu-Wei, R. Zeying, and C. T. C. Nguyen, "Self-switching vibrating micromechanical filter bank," in *Frequency Control Symposium and Exposition, 2005. Proceedings of the 2005 IEEE International*, 2005, p. 7 pp.

[24] J. Wang, Z. Ren, and C. T. C. Nguyen, "1.14-GHz self-aligned vibrating micromechanical disk resonator," in *Radio Frequency Integrated Circuits (RFIC) Symposium, 2003 IEEE*, 2003, pp. 335-338.

[25] H. Li-Wen, C. T. C. Nguyen, X. Yuan, L. Yu-Wei, L. Sheng-Shian, and R. Zeying, "UHF Micromechanical Compound-(2,4) Mode Ring Resonators With Solid-Gap Transducers," in *Frequency Control Symposium, 2007 Joint with the 21st European Frequency and Time Forum. IEEE International*, 2007, pp. 1370-1375.

[26] M. Akgul, B. Kim, Z. Ren, and C. T.-C. Nguyen, "Capacitively transduced micromechanical resonators with simultaneous low motional resistance and Q >70,000," in *Tech. Digest, 2008 Solid-State Sensor, Actuator, and Microsystems Workshop*, Hilton Head, South Carolina, 2010, pp. 467-470.

[27] L.-W. Hung, Z. A. Jacobson, Z. Ren, A. Javey, and C. T.-c. Nguyen, "Capacitive transducer strengthening via ALD-enabled partial gap filling," in *Tech. Digest, 2008 Solid-State Sensor, Actuator, and Microsystems Workshop* Hilton Head, SC, 2008, pp. 208-211.

[28] D. Weinstein and S. A. Bhave, "Acoustic resonance in an independent-gate FinFET," in *Hilton Head*, 2010, pp. 459--462.

[29] J. Wang, J. E. Butler, T. Feygelson, and C. T. C. Nguyen, "1.51-GHz nanocrystalline diamond micromechanical disk resonator with material-mismatched isolating support," in *Micro Electro Mechanical Systems, 2004. 17th IEEE International Conference on. (MEMS)*, 2004, pp. 641-644.

[30] L. Yu-Wei, H. Li-Wen, L. Sheng-Shian, R. Zeying, and C. T. C. Nguyen, "Quality Factor Boosting via Mechanically-Coupled Arraying," in *Solid-State Sensors, Actuators and Microsystems Conference, 2007. TRANSDUCERS 2007. International*, 2007, pp. 2453-2456.

[31] M. Onoe, "Contour Vibrations of Isotropic Circular Plates," *Journal of The Acoustical Society of America,* vol. 28, pp. 1158-1162, 1956.

[32] R. Navid, J. R. Clark, M. Demirci, and C. T. C. Nguyen, "Third-order intermodulation distortion in capacitively-driven CC-beam micromechanical resonators," in *Micro Electro Mechanical Systems, 2001. MEMS 2001. The 14th IEEE International Conference on*, 2001, pp. 228-231.

[33]   Y.-W. Lin, S.-S. Li, Y. Xie, Z. Ren, and C. T. C. Nguyen, "Vibrating micromechanical resonators with solid dielectric capacitive transducer gaps," in *IEEE International Frequency Control Symposium and Exposition*, 2005, pp. 128-134.

[34]   S. M. George, "Atomic Layer Deposition: An Overview," *Chemical Reviews,* vol. 110, pp. 111-131, 2010.

[35]   Y.-W. Lin, S.-S. Li, Y. Xie, Z. Ren, and N. C. T. C., "Vibrating micromechanical resonators with solid dielectric capacitive transducer gaps," in *IEEE International Frequency Control Symposium and Exposition*, 2005, pp. 128-134.

[36]   R. Abdolvand and F. Ayazi, "Single-mask reduced-gap capacitive micromachined devices," in *Micro Electro Mechanical Systems, 2005. MEMS 2005. 18th IEEE International Conference on*, 2005, pp. 151-154.

[37]   T. J. Cheng and S. A. Bhave, "High-Q, low impedance polysilicon resonators with 10 nm air gaps," in *Micro Electro Mechanical Systems (MEMS), 2010 IEEE 23rd International Conference on*, 2010, pp. 695-698.

[38]   Y.-I. Lee, K. Park, x, Ho, L. Jonghyun, C. S. Lee*, et al.*, "Dry release for surface micromachining with HF vapor-phase etching," *Microelectromechanical Systems, Journal of,* vol. 6, pp. 226-233, 1997.

[39]   U. C. NanoTech. (2011). *Atomic Layer Deposition Overview*. Available: http://www.cambridgenanotechald.com/atomic-layer-deposition-tutorial.shtml#

[40]   W. Li, O. Auciello, R. N. Premnath, and B. Kabius, "Giant dielectric constant dominated by Maxwell–Wagner relaxation in Al2O3/TiO2 nanolaminates synthesized by atomic layer deposition," *Applied Physics Letters,* vol. 96, pp. -, 2010.

[41]   K. B. Jinesh, Y. Lamy, J. H. Klootwijk, and W. F. A. Besling, "Maxwell-Wagner instability in bilayer dielectric stacks," *Applied Physics Letters,* vol. 95, pp. 122903-122903-3, 2009.

[42]   O. P. Watts, *Transactions of the American Electrochemical Society* vol. 29, 1916.

[43]   C. T. C. Nguyen, "High-Q micromechanical oscillators and filters for communications," in *Circuits and Systems, 1997. ISCAS '97., Proceedings of 1997 IEEE International Symposium on*, 1997, pp. 2825-2828 vol.4.

[44]   A. T. Alastalo and V. Kaajakari, "Intermodulation in capacitively coupled microelectromechanical filters," *Electron Device Letters, IEEE,* vol. 26, pp. 289-291, 2005.

[45]   Y.-W. Lin, S.-S. Li, Z. Ren, and C. T. C. Nguyen, "Third-order intermodulation distortion in capacitively-driven VHF micromechanical resonators," in *Ultrasonics Symposium, 2005 IEEE*, 2005, pp. 1592-1595.

[46]   B. Razavi, *RF Microelectronics*: Prentice Hall PTR, 2011.

[47]   C. T.-C. Nguyen, "Micromechanical Signal Processors," Ph.D. Dissertation, Department of Electrical Engineering and Computer Sciences, University of California at Berkeley, 1994.

[48]   L. Piezoelectric Ceramics from APC International, *Piezoelectric Ceramics: Principles and Applications*, 2011.

[49]   "IEEE Standard on Piezoelectricity," *ANSI/IEEE Std 176-1987,* p. 0_1, 1988.

[50]   T. Fritz, M. Griepentrog, W. Mokwa, and U. Schnakenberg, "Determination of Young's modulus of electroplated nickel," *Electrochimica Acta,* vol. 48, pp. 3029-3035, 9/30/ 2003.

[51]   U. o. Cambridge. *Derivation of the rule of mixtures and inverse rule of mixtures*. Available: http://www.doitpoms.ac.uk/tlplib/bones/derivation_mixture_rules.php

[52]   C. T. Nguyen, "Micromachining technologies for miniaturized communication devices," 1998, pp. 23-37.

[53]   M. W. Putty and K. Najafi, "A micromachined vibrating ring gyroscope," in *Sensor and Actuator Workshop*, Hilton Head Island, SC, 1994, pp. 213-220.

[54]   W.-T. Hsu, S. Lee, and C. T.-C. Nguyen, "In Situ Localized Annealing for Contamination Resistance and Enhanced Stability in Nickel Micromechanical Resonators," in *10th International Conference on Solid-State Sensors and Actuators*, Sendai, Japan, 1999, pp. 932-935.

[55]   J. Audet. (2012). *Q Factor Measurements on L-C Circuits*. Available: http://hb9abx.no-ip.biz/VE2AZX-Q-factor.pdf

[56]   S. Pourkamali, G. K. Ho, and F. Ayazi, "Low-Impedance VHF and UHF Capacitive Silicon Bulk Acoustic-Wave Resonators Part II: Measurement and Characterization," *Electron Devices, IEEE Transactions on,* vol. 54, pp. 2024-2030, 2007.

[57]   M. U. Demirci and C. T. C. Nguyen, "Mechanically Corner-Coupled Square Microresonator Array for Reduced Series Motional Resistance," *Microelectromechanical Systems, Journal of,* vol. 15, pp. 1419-1436, 2006.

[58]   J. Wang, "SELF-ALIGNED RADIAL CONTOUR MODE MICROMECHANICAL DISK RESONATORS FOR WIRELESS COMMUNICATIONS," Doctor of Philosophy, University of Michigan, 2006.

[59]   J. H. Wu, J. Scholvin, and J. A. del Alamo, "A through-wafer interconnect in silicon for RFICs," *Electron Devices, IEEE Transactions on,* vol. 51, pp. 1765-1771, 2004.

[60]   A. Mahmoud Al and R. Plana, "Piezoelectric Coefficients of Thin Film Aluminum Nitride Characterizations Using Capacitance Measurements," *Microwave and Wireless Components Letters, IEEE,* vol. 19, pp. 140-142, 2009.

[61]   J.-h. Yang, J. Kim, Y. Kang, Y. Park, C. Yang, P. Kang*, et al.*, "Effects of Piezoelectric Constants and Thicknesses of Lead-zirconate-titanate Ceramics on the Performances of Inkjet Printheads," *Journal of the Korean Physical Society,* vol. 59, pp. 3008-3013, 2011.

APPENDICES

Appendix A Process Traveler

A.1 IC-Compatible Electroplated-Nickel Air-Gap Resonator Process Traveler

1. Starting Wafers: High Resistivity Silicon, 6000Ω-cm, p-type, <100>, 450um

   Label wafers as process and control samples.

2. Pattern Resonator Bottom Electrodes

   a. Solvent Clean

   b. Dehydration Bake on Hotplate: 5 min @ 150°C

   c. Spin Photoresist by Laura Spinner

      HMDS: 30 sec @ 3000 RPM

      LOR 3B: 30 sec @ 3000 RPM

      Softbake: 30sec @ 100°C

      1827: 40 sec @ 4000 RPM

      Softbake: 2 min @ 100°C

   d. Expose in EVG Mask Aligner

      Hard Contact

      4 sec @ 25 mW/cm^2

   e. Develop

      Chemical: AZ 726

      Time: 1 min

   f. Descum

      Equipment: Plasma Therm

      O_2: 50 sccm

      Pressure: 300 mTorr

      Power: 75 watts

      Time: 2 min

   g. Deposit Metal

      Equipment: E-beam Evaporation

      Cr: 100nm

      Au: 300nm

   h. Lift-Off

Chemical: 1165 Photoresist Stripper

Time: 1hr

    i. Descum

Equipment: Plasma Therm

O_2: 50 sccm

Pressure: 300 mTorr

Power: 75 watts

Time: 2 min

3. Deposit Sacrificial Layer

Equipment: Plasma Therm

PECVD SiO_2: 1um

4. Pattern Via Anchors

    a. Solvent Clean

    b. Dehydration Bake on Hotplate: 5 min @ 150°C

    c. Spin Photoresist by Laura Spinner

HMDS: 30 sec @ 3000 RPM

1827: 40 sec @ 4000 RPM

Softbake: 2 min @ 100°C

    d. Expose in EVG Mask Aligner

Hard Contact

4 sec @ 25 mW/cm^2

    e. Develop

Chemical: AZ 726

Time: 1 min

    f. Descum

Equipment: Plasma Therm

O_2: 50 sccm

Pressure: 300 mTorr

Power: 75 watts

Time: 2 min

    g. Etch Sacrificial Layer

Equipment: Alcatel AMS 100

Temperature: -20°C

C_4F_8: 17 sccm

He: 150 sccm

CH_4: 13 sccm

Power: 2800 watts

Time: 2.5 min

h. Strip Photoresist

Chemical: 1165 Photoresist Stripper

Time: 40 min

5. Nickel Electroplating for Resonator

a. Deposit Seed Layer

Equipment: E-beam Evaporation

Cr: 20nm

Au: 30nm

b. Solvent Clean

c. Dehydration Bake on Hotplate: 5 min @ 150°C

d. Spin Photoresist by Laura Spinner

HMDS: 30 sec @ 3000 RPM

AZ P4620: 40 sec @ 2000 RPM

Softbake: 5 min @ 100°C

e. Expose in EVG Mask Aligner

Vacuum Contact

10 sec @ 25 mW/cm^2

f. Develop

Chemical: AZ 400K

Time: 3 min

g. Descum

Equipment: Plasma Therm

O_2: 50 sccm

Pressure: 300 mTorr

Power: 75 watts

Time: 2 min

h. Nickel Electroplating

Chemical: Nickel Sulfamate

Agitation Rate: 200 rpm

Temperature: 50°C

pH: 3.5-4.5

Current density: 10-20 mA/cm²

Time: 13mins

Thickness: 5um

i. Strip Photoresist

Chemical: AZ 400T Photoresist Stripper

Time: 20 min

j. Strip Seed Layer

Chemical: Au Etchant, Cr Etchant

Time: 1min

6. Define Resonator to Electrode Gap

a. Deposit Al_2O_3 by Atomic Layer Deposition

Equipment: Savannah 100 by Cambridge NanoTech Inc.

Temperature: I=O=250 °C, T=V=B=150 °C

Flow rate: 20 sccm

Recipe: pulse H_2O, 0.015 sec

wait 20 sec

pulse TMA, 0.1 sec

wait 20 sec

cycle 867

Deposition rate: 0.9 Å/cycle

b. Solvent Clean

c. Dehydration Bake on Hotplate: 5 min @ 150°C

d. Spin Photoresist by Laura Spinner

HMDS: 30 sec @ 3000 RPM

AZ P4620: 40 sec @ 2000 RPM

Softbake: 10 min @ 100°C

    e. Expose in EVG Mask Aligner

Vacuum Contact

10 sec @ 25 mW/cm^2

    f. Develop

Chemical: AZ 400K

Time: 3 min

    g. Descum

Equipment: Plasma Therm

O_2: 50 sccm

Pressure: 300 mTorr

Power: 75 watts

Time: 2 min

    h. Etch ALD

Equipment: Alcatel AMS 100

Temperature: -20°C

C_4F_8: 17 sccm

He: 150 sccm

CH_4: 13 sccm

Power: 2800 watts

Time: 40 sec

    i. Strip Photoresist

Chemical: AZ 400T Photoresist Stripper

Time: 20 min

7. Nickel Electroplating for Electrodes

    a. Deposit Seed Layer

Equipment: E-beam Evaporation

Cr: 20nm

Cu: 30nm

    b. Solvent Clean

c. Dehydration Bake on Hotplate: 5 min @ 150°C

d. Spin Photoresist by Laura Spinner

HMDS: 30 sec @ 3000 RPM

AZ P4620: 40 sec @ 2000 RPM

Softbake: 10 min @ 100°C

AZ P4620: 40 sec @ 2000 RPM

Softbake: 10 min @ 100°C

e. Etch Back Process

Equipment: Alcatel AMS 100

Temperature: 20°C

O_2: 50 sccm

Power: 2000 watts

Time: 12 min

f. Etch Top Seed Layer

Chemical: Cu Etchant, Cr Etchant

Time: 1min

g. Strip Photoresist

Chemical: AZ 400T Photoresist Stripper

Time: 20 min

h. Solvent Clean

i. Dehydration Bake on Hotplate: 5 min @ 150°C

Spin Photoresist by Laura Spinner

HMDS: 30 sec @ 3000 RPM

AZ P4620: 40 sec @ 2000 RPM

Softbake: 5 min @ 100°C

j. Expose in EVG Mask Aligner

Vacuum Contact

10 sec @ 25 mW/cm^2

k. Develop

Chemical: AZ 400K

Time: 3 min

    l. Descum

        Equipment: Plasma Therm

        O_2: 50 sccm

        Pressure: 300 mTorr

        Power: 75 watts

        Time: 2 min

    m. Nickel Electroplating

        Chemical: Nickel Sulfamate

        Agitation Rate: 200 rpm

        Temperature: 50°C

        pH: 3.5-4.5

        Current density: 10-20 mA/cm²

        Time: 13mins

        Thickness: 5um

    n. Strip Photoresist

        Chemical: AZ 400T Photoresist Stripper

        Time: 20 min

    o. Strip Seed Layer

        Chemical: Cu Etchant, Cr Etchant

        Time: 1min

8. Structure Release

    a. Etch Sacrificial Layer

        Chemical: Diluted HF with Triton-X

        Time: 20-30 min

        Rinse: 10 min

    b. Methanol Soak

        Time: 10 min

        Air Dry

9. Partially Fill Air Gap

    a. Deposit Al2O3 by Atomic Layer Deposition

        Equipment: Savannah 100 by Cambridge NanoTech Inc.

Temperature: I=O=250 °C, T=V=B=150 °C

Flow rate: 20 sccm

Recipe: pulse H2O, 0.015 sec

　wait 20 sec

　　　pulse TMA, 0.1 sec

　　　wait 20 sec

　　　cycle 867

Deposition rate: 0.9 Å/cycle

A.2 IC-Compatible Electroplated-Nickel Solid-Gap Resonator Process Traveler

1. Starting Wafers: Standard Silicon, 1-100 Ω-cm, p-type, <100>, 450um

   Label wafers as process and control samples.

2. Pattern Resonator Bottom Electrodes

   a. Solvent Clean

   b. Dehydration Bake on Hotplate: 5 min @ 150°C

   c. Spin Photoresist by Laura Spinner

      HMDS: 30 sec @ 3000 RPM

      LOR 3B: 30 sec @ 3000 RPM

      Softbake: 30sec @ 100°C

      1827: 40 sec @ 4000 RPM

      Softbake: 2 min @ 100°C

   d. Expose in EVG Mask Aligner

      Hard Contact

      4 sec @ 25 mW/cm^2

   e. Develop

      Chemical: AZ 726

      Time: 1 min

   f. Descum

      Equipment: Plasma Therm

      O_2: 50 sccm

      Pressure: 300 mTorr

Power: 75 watts

Time: 2 min

g. Deposit Metal

Equipment: E-beam Evaporation

Cr: 100nm

Au: 300nm

Pt: 100nm

h. Lift-Off

Chemical: 1165 Photoresist Stripper

Time: 1hr

i. Descum

Equipment: Plasma Therm

O_2: 50 sccm

Pressure: 300 mTorr

Power: 75 watts

Time: 2 min

3. Deposit Sacrificial Layer

Equipment: Plasma Therm

PECVD amorphous-Si: 1um

4. Pattern Via Anchors

a. Solvent Clean

b. Dehydration Bake on Hotplate: 5 min @ 150°C

c. Spin Photoresist by Laura Spinner

HMDS: 30 sec @ 3000 RPM

1827: 40 sec @ 4000 RPM

Softbake: 2 min @ 100°C

d. Expose in EVG Mask Aligner

Hard Contact

4 sec @ 25 mW/cm^2

e. Develop

Chemical: AZ 726

Time: 1 min

    f. Descum

        Equipment: Plasma Therm

        O_2: 50 sccm

        Pressure: 300 mTorr

        Power: 75 watts

        Time: 2 min

    g. Etch Sacrificial Layer

        Equipment: Alcatel AMS 100

        Temperature: -15°C

        SF6: 300 sccm, 3 sec

        C4F8: 200 sccm, 1.4 sec

        O2: 20 sccm, 1.4 sec

        Power: 2400 watts

        Pulsed power: 25 ms @ 100 watts; 75 ms @ 0 watts

        Time: 1 min 10 sec

        Etch rate: ~0.8 um/min

    h. Strip Photoresist

        Chemical: 1165 Photoresist Stripper

        Time: 40 min

5. Nickel Electroplating for Resonator

    a. Deposit Seed Layer

        Equipment: E-beam Evaporation

        Cr: 20nm

        Au: 30nm

    b. Solvent Clean

    c. Dehydration Bake on Hotplate: 5 min @ 150°C

    d. Spin Photoresist by Laura Spinner

        HMDS: 30 sec @ 3000 RPM

        AZ P4620: 40 sec @ 2000 RPM

        Softbake: 5 min @ 100°C

e. Expose in EVG Mask Aligner

Vacuum Contact

10 sec @ 25 mW/cm^2

f. Develop

Chemical: AZ 400K

Time: 3 min

g. Descum

Equipment: Plasma Therm

O_2: 50 sccm

Pressure: 300 mTorr

Power: 75 watts

Time: 2 min

h. Nickel Electroplating

Chemical: Nickel Sulfamate

Agitation Rate: 200 rpm

Temperature: 50°C

pH: 3.5-4.5

Current density: 10-20 mA/cm²

Time: 13mins

Thickness: 5um

i. Strip Photoresist

Chemical: AZ 400T Photoresist Stripper

Time: 20 min

j. Strip Seed Layer

Chemical: Au Etchant, Cr Etchant

Time: 1min

6. Define Resonator to Electrode Gap

a. Deposit Ti_2O_3 by Atomic Layer Deposition

Equipment: Savannah 100 by Cambridge NanoTech Inc.

Temperature: I=O=250 °C, T=V=B=150 °C

Flow rate: 20 sccm

Recipe: pulse H_2O, 0.015 sec

       wait 20 sec

       pulse $Ti(NMe_2)_4$, 0.1 sec

       wait 20 sec

       cycle 769

Deposition rate: 0.39 Å/cycle

b. Solvent Clean

c. Dehydration Bake on Hotplate: 5 min @ 150°C

d. Spin Photoresist by Laura Spinner

HMDS: 30 sec @ 3000 RPM

AZ P4620: 40 sec @ 2000 RPM

Softbake: 10 min @ 100°C

e. Expose in EVG Mask Aligner

Vacuum Contact

10 sec @ 25 mW/cm^2

f. Develop

Chemical: AZ 400K

Time: 3 min

g. Descum

Equipment: Plasma Therm

O_2: 50 sccm

Pressure: 300 mTorr

Power: 75 watts

Time: 2 min

h. Etch ALD

Equipment: Alcatel AMS 100

Temperature: -20°C

C_4F_8: 17 sccm

He: 150 sccm

CH_4: 13 sccm

Power: 2800 watts

Time: 30 sec

    i.   Strip Photoresist

        Chemical: AZ 400T Photoresist Stripper

        Time: 20 min

7. Nickel Electroplating for Electrodes

    a. Deposit Seed Layer

        Equipment: E-beam Evaporation

        Cr: 20nm

        Cu: 30nm

    b. Solvent Clean

    c. Dehydration Bake on Hotplate: 5 min @ 150°C

    d. Spin Photoresist by Laura Spinner

        HMDS: 30 sec @ 3000 RPM

        AZ P4620: 40 sec @ 2000 RPM

        Softbake: 10 min @ 100°C

        AZ P4620: 40 sec @ 2000 RPM

        Softbake: 10 min @ 100°C

    e. Etch Back Process

        Equipment: Alcatel AMS 100

        Temperature: 20°C

        O_2: 50 sccm

        Power: 2000 watts

        Time: 12 min

    f. Etch Top Seed Layer

        Chemical: Cu Etchant, Cr Etchant

        Time: 1min

    g. Strip Photoresist

        Chemical: AZ 400T Photoresist Stripper

        Time: 20 min

    h. Solvent Clean

    i. Dehydration Bake on Hotplate: 5 min @ 150°C

Spin Photoresist by Laura Spinner

HMDS: 30 sec @ 3000 RPM

AZ P4620: 40 sec @ 2000 RPM

Softbake: 5 min @ 100°C

j. Expose in EVG Mask Aligner

Vacuum Contact

10 sec @ 25 mW/cm^2

k. Develop

Chemical: AZ 400K

Time: 3 min

l. Descum

Equipment: Plasma Therm

O_2: 50 sccm

Pressure: 300 mTorr

Power: 75 watts

Time: 2 min

m. Nickel Electroplating

Chemical: Nickel Sulfamate

Agitation Rate: 200 rpm

Temperature: 50°C

pH: 3.5-4.5

Current density: 10-20 mA/cm²

Time: 13mins

Thickness: 5um

n. Strip Photoresist

Chemical: AZ 400T Photoresist Stripper

Time: 20 min

o. Strip Seed Layer

Chemical: Cu Etchant, Cr Etchant

Time: 1min

8. Structure Release

a. Etch Sacrificial Layer

Equipment: Alcatel AMS 100

Temperature: -15°C

SF6: 300 sccm, 3 sec

O2: 20 sccm, 1.4 sec

Power: 2400 watts

Time: 20min

Appendix B Copyright Permissions

The permission below is for the use of Figure 1.6.

The permission below is for the use of Figure 1.7 and 1.8.

To: President of the Japan Society of Applied Physics

23 / May / 2014
Day   Month   Year

Submit to:
Publication Center for Pure and Applied Physics, The Japan Society of Applied Physics
2-31-22-5F, Yushima, Bunkyo-ku, Tokyo 113-0034, Japan
TEL: +81-3-5844-3291 FAX: +81-3-5844-3290 E-mail address: permission@jsap.or.jp

Application for Permission to Reproduce Material

I request permission to reproduce the following material, copyrighted by the Japan Society of Applied Physics.

Publication where material is reproduced (the Publication)

Name of the Publication (e.g., journal title, book title): Development of Electroplated-Ni Structured Capacitively-Transduced Micromechanical Resonators for RF Application
Publisher (e.g., publishing company): University of South Florida / Dissertation
Planned date of publication: July, 2014
Number of copies: 1

Content of reproduction (the Content)

Journal title: Japanese Journal of Applied Physics
Volume/Year/ID(starting page): 44 / 2005 /2883
Article title: Development of Piezoelectric Thin Film Resonator and Its Impact on Future Wireless Communication Systems
Author(s): Yoshio Satoh, Tokihiro Nishihara, Tsuyoshi Yokoyama, Masanori Ueda and Tsutomu Miyashita
Content to be reproduced (please specify): Figure 1 and Figure 2

Applicant (only to be completed by the author of the Publication)

Name: Mian Wei
Affiliation (e.g., university, company, organization): University of South Florida

E-mail address: mwei@mail.usf.edu

I will abide by the following conditions of reproduction.
1. A credit line "Copyright publication year The Japan Society of Applied Physics" must be added to the Content (in the figure caption(s)). The material containing the Content, copyrighted by the Japan Society of Applied Physics, must be cited in the references of the Publication.
2. The Content will not be modified.
3. The Content will not be reproduced in other materials.

Signature of applicant:

* The purpose of reproduction will be considered before permission is granted.

ENDORSEMENT

Dr.   Mian Wei,

I permit the reproduction of the Content in the Publication.

26 / May / 2014
Day   Month   Year

President, The Japan Society of Applied Physics

The permission below is for the use of Figure 1.9.

The permission below is for the use of Figure 1.10.

The permission below is for the use of Figure 1.11.

The permission below is for the use of Figure 1.12.

Copyright Clearance Center

RightsLink®

Home | Account Info | Help

Title: UHF Micromechanical Compound-(2,4) Mode Ring Resonators With Solid-Gap Transducers

Conference Proceedings: Frequency Control Symposium, 2007 Joint with the 21st European Frequency and Time Forum. IEEE International

Author: Li-Wen Hung; Nguyen, C.T.-C.; Yuan Xie; Yu-Wei Lin; Sheng-Shian Li; Zeying Ren

Publisher: IEEE

Date: May 29 2007-June 1 2007

Copyright © 2007, IEEE

Logged in as:
Mian Wei
University of South Florida
Account #:
3000793747

LOGOUT

The permission below is for the use of Figure 1.14.

ABOUT THE AUTHOR

Mian Wei received her B.S. degree from Tianjin University of Science and Technology, Tianjin, China, in 2007; her M.S. degree in Electrical Engineering from the University of South Florida, Tampa, in 2010, and is currently working towards her Ph.D. degree in Electrical Engineering at the University of South Florida. She is currently working with Dr. Jing Wang in the RF MEMS Transducers Group (a division of the WAMI Center), Electrical Engineering Department, University of South Florida. Her areas of research are RF and MEMS devices. Her current research involves the design, simulation, fabrication and measurement of MEMS resonators for wireless communications.